Determination of the attitude state of space debris objects based on Satellite Laser Ranging

Using Envisat as a test-case

B.F. Lagaune

MSc Thesis Aerospace Engineering

© Denman Productions 2000

Credits to cover image: European Space Agency (ESA)

Determination of the attitude state of space debris objects based on Satellite Laser Ranging

Using Envisat as a test-case

by

B.F. Lagaune

to obtain the degree of Master of Science
at the Delft University of Technology,
to be defended publicly on Wednesday December 21, 2016 at 09:30 AM.

Student number:	4065174	
Project duration:	February 1, 2016 – December 21, 2016	
Thesis supervisor:	Dr. Ir. E.N. Doornbos,	TU Delft
Thesis committee:	Prof. Dr. P.N.A.M. Visser,	TU Delft
	Dr. Ir. J.M. Kuiper,	TU Delft

Summary

The past few years, attitude states of space debris objects have become of larger interest for various reasons. The first includes a valuable source of information for active-debris removal missions. Secondly attitude information could provide better short and long-term orbit predictions. Where the short term predictions might only rely on a correct interpretation of the offset between the Center of mass (COM) and the Laser Retro Reflector (LRR), long term predictions involve accurate force model estimations which need attitude information. Multiple techniques exist to evaluate the attitude state of passive objects like radar mapping, evaluating light curves, or if the object contains a LRR, Satellite Laser Ranging (SLR). The latter is used in this thesis to evaluate the performance and use with respect to the attitude determination of Envisat in the period of 2013-2016. From the range residuals(between the ground station and the satellite), a clear oscillating signal can be seen. This indicates the rotating LRR around the COM during a measurement. The attitude determination technique used here involves matching simulated range residuals with their true solution in order to derive the specific attitude state at that particular moment of time.

The true residuals are created using a simple cannonball model approximation during the orbit determination process using GEODYN (orbit determination software from NASA). Large empirical accelerations in the orbit determination process ensured the sparse data set of laser data to produce residuals which were centred around zero and showed almost no linear trend. Due to the low and highly distributed amount of data available for Envisat, fluctuations in the different orbits occur but show not to have large differences on the residuals.

In order to validate the attitude estimation process, simulated range residuals where created with known input parameters which where then estimated. Envisat is regarded as a torque-free rigid body as only short arcs are considered. A total of seven parameters govern the full rotational motion: Three rotational parameters (speed and direction of the spin axis) and four quaternions describing the (initial) attitude. An attitude simulator was created using a fourth order Runge-Kutta family (RK4) integration scheme. Several different scenarios where chosen to asses the performance of the attitude determination technique. Both single pass as well as using multiple passes simultaneously were evaluated. A Sequential Least Squares Programming (SLSQP) optimization algorithm was used to match the attitude parameters which resulted in the smallest difference between the true and estimated residuals. When considering one single pass, a minimum of two revolutions are necessary in order to end up with the true solution. Multiple local minima do however exist which make it hard to converge to the true solution if the initial guess is set too far apart from the true solution. This problem can be partially solved using a slightly different approach, but only when the spin axis is assumed to lie in the direction of a principal axis of the body. It consists of two phases where the first rotates the body around its principal axis with an euler angle (reducing the number of parameters to be estimated). Secondly, the found best fit conditions of the first phase are used as the initial conditions in the full quaternion estimation scheme which lie close enough to the solution to converge. This method shows to work even if precession in the spin axis is added. The key advantage lies in the fact that the initial conditions do not need to lie that close to the true solution in order to find the true solution.

Next, multiple stations where evaluated simultaneously. A difference was made between simultaneous tracking and separated tracking. When multiple stations track Envisat from the same direction as seen from the local orbit frame the solution does not converge any faster than considering one single pass. If Envisat might be tracked from multiple directions, no increase in converge speed has been found when compared to a local pass. When two or more passes are evaluated at the same time but separated from each other the solution converges in less function evaluations. This however does require longer computational time as the attitude state needs to be propagated till the next pass.

Investigating real Envisat data has only been done using local passes. Due to the sparse distribution of long passes, a multi-pass method was not used. The spin axis orientation shows not to remain stable over the years but shows large deviations of about 220–320° in azimuth and 10–60° in elevation angle respectively in the local orbit frame. The estimated rotational period shows a non linear increase over time indicating its rotational loss over time.

Furthermore, the implementation of the found attitude of Envisat in the orbit determination process needs to be evaluated.

Abstract

The attitude state of the passive Envisat satellite (ESA) has been estimated before using various techniques like Satellite Laser Ranging, radar and using light-curves. This research focusses on the use of Satellite Laser Ranging. Due to the relatively large (meter scale) offset between the center-of-mass of the satellite and the reflector where the laser signal is reflected back to the transmitting and receiving ground station, large oscillations in the range residuals are visible. These oscillations show the rotating behaviour of Envisat, and can be translated to its rotational state by re-producing this signal using a corresponding attitude model and the offset between the reflector and the center-of-mass. First a purely theoretical case was considered where a known simulated orbit and attitude where estimated for various cases in order to validate the use of the estimation scheme. Afterwords, the real Satellite Laser Ranging data of Envisat was used for the time period 2013-2015.

Preface

I would like to state my professor and former Dutch ESA-astronaut Wubbo Ockels: "We are all astronauts, and the Earth is our spaceship". With these inspiring words, Wubbo showed me and others, the vulnerability of our Earth in the entire galactic. We should all take care of our Earth. If only more people could open their eyes and see how vulnerable the Earth actual is, maybe a large step towards a greener and brighter future could be set.

During my 4-month internship at the German Space Operations Center (GSOC) of the Deutsches Zentrum für Luft- und Raumfahrt (DLR) in Munich, I had the opportunity to analyse SLR data of the passive Envisat. Here I mainly focussed on the orbital evolution past its end-of-life and addressed briefly the rotational state of Envisat. My supervisors, Martin Weigel and Hauke Fiedler gave me the opportunity to continue my internship work in an MSc thesis, where the focus would be on determining the attitude of Envisat. Unfortunately, I wanted to head back to Delft (friends, family and girlfriend) to sit my last year in Delft. The subject really interested me, so I searched for an appropriate supervisor in Delft. Here I found Eelco Doornbos, which was familiar with orbit determination of Envisat during its active lifetime. Together we proposed a mail-contact relation between DLR and the TU Delft. I was ready to start.

During my literature study it became clear that a similar big project which involved attitude determination of space debris objects has been set up with funding from ESA. This made that I had to shift the focus of my thesis slightly to simulating SLR data, and validating the performance of the attitude determination using SLR data. In May, I visited the Clean Space Industrial Days of ESA at ESTEC, where the topic of Envisat's removal brought forward that its attitude remained one of the big challenges. My motivation of continuing my research had grown even more.

During my eight-month time at the Astrodynamics and Space Missions department of the faculty of Aerospace Engineering I had the opportunity to ask all my questions at all staff and student members. I would like to thank everybody who helped me set up GEODYN (which was quite a expedition). Thanks to Eelco Doornbos and Jose van den Ijssel for guiding me through the numerous options of GEODYN and thanks to Bart Root and Ernst Schrama who provided me with useful converters of SLR data. During my thesis I had the opportunity to sit in the MSc student room(if you came in time that is) and share thoughts and interests among my colleagues. This was extremely useful as you could discuss not only directly with your fellow students but also with all other staff members of the department. Next, I would like to thank Martin Weigel from DLR, with whom I could discuss and compare my results with through e-mail.

Last but not least I would to thank especially my parents for making it possible to follow my dreams. My girlfriend for supporting me during hard times, and my sports association S.B.V. Slopend for creating a perfect way for getting out and clearing your minds. You have all been an inspiring source of motivation.

B.F Lagaune
Delft, December 2016

Contents

List of Figures

List of Tables

Acronyms

ASAR Advanced Synthetic Aperture Radar. 12
AT Along-track. 28
Az Azimuth. 23

b-frame body fixed frame. 8
BFGS Broyden–Fletcher–Goldfarb–Shanno algorithm. 69, 70
BoL Beginning of life. 14

CCR Corner Cube Reflector. 14
CCW Counter-Clockwise. 98
CDDIS Crustal Dynamics Data Information System. 34
CNES Centre National d'Etudes Spatiales. 18
COM Center of mass. 15, 34
CRD Consolidated Laser Ranging Data Format. 7, 33

DCM Direction Cosine Matrix. 23, 107

ECEF Earth Centered Earth Fixed. 10
ECI Earth Centered Inertial. 10
EDC EUROLAS Data Centre. 34
EGM96 Earth Gravitational Model 1996. 37
El Elevation. 23
EOP Earth Orientation Parameters. 57
EQ Euler Quaternion. 72, 74, 81, 82, 89, 90, 96, 99, 104
ERS European Remote Sensing. 11
ESA European Space Agency. 11, 14

f-frame Envisat spacecraft fixed frame. 8

GBF Geodyn binary Format. 34
GCRF Geocentric Celestial Reference Frame. 57
GIIE Geodyn II Execute. 32
GIIS GEODYN II Setup. 32, 36
GOCE Gravity Field and Steady-Stae Ocean Circulation Explorer. 36

i-frame inertial orbit frame. 8
IAU International Astronomical Union. 43
IDS International Doris Service. 16
IERS International Earth Rotation Service. 10, 37, 43
ILRS International Laser Ranging Service. 7, 15, 33
iota In-Orbit Tumbling Analysis. 100
ISAR Inverse Synthetic Aperture Radar. 13, 61
ITRF International Terrestrial Reference Frame. 10, 47, 57

L-BFGS-B Limited-memory Broyden-Fletcher-Goldfarb-Shanno with Bound constraints. 69, 79, 80
l-frame local orbit frame. 8
Lat Latitude. 28
LEO Low Earth Orbit. 4
LOD Length of Day. 43
Lon Longitude. 28
LRR Laser Retro Reflector. 5, 14, 15, 34, 65, 103–105

N Normal. 28
n Nadir. 28
NGDC National Geophysical Data Center. 38
NOVAS United States Naval Observatory NOVAS astronomy library. 57

OD Orbit Determination. 36

PCE NASA archaic data format. 34

R Radial. 28
RCS Radial Coordinate System. 28
RK4 fourth order Runge-Kutta family. 21
RMS Root Mean Square. 37

SBF Satellite Body Frame. 44
SLR Satellite Laser Ranging. 4, 6, 15, 32
SLSQP Sequential Least Squares Programming. 69, 103
STK Systems Tool Kit. 66

TAI International Atomic Time. 43
TDF Tracking Data Formatter. 32
TDT Terrestrial Dynamical Time. 43
TLE Two-Line-Element. 8, 36
TOD True of Date. 10
TT Terrestrial Time. 43

UTC Universal Time Coordinate. 43

XML eXtensible Markup Language. 33

Nomenclature

α	Cone half angle	rad
$\ddot{r}_{emp}$	Empirical acceleration	m/s^2
$\Delta\nu$	Difference between simulated and estimated residuals	-
$\dot{\omega}$	Angular acceleration	rad/s^2
ϵ	Measurement noise	-
ϵ_{min}	Minimum elevation angle	rad
η_{max}	Maximum nadir angle	rad
$\hat{e}$	Euler axis unit vector	-
$\hat{r_{e'}}$	Unit vector in the e'- frame	-
$\hat{r}_e$	Unit vector in the e- frame	-
$\lambda_{max,min}$	Maximum/Minimum Earth Central Angle	rad
λ_{min}	Minimum Earth central angle	rad
λ_{op}	Longitude of orbit pole	rad
$\nu_{estimated}$	Estimated residuals	m
$\nu_{simulated}$	Simulated residuals	m
Ω	Skew symmetric matrix	-
ω	Angular velocity	rad/s
Φ	Phase angle empirical acceleration	rad
ϕ	Euler angle around euler axis	deg
ϕ	Roll angle (rotation around X axis)	rad
ϕ_{op}	Latitude of orbit pole	rad
ψ	Yaw angle (rotation around Z axis)	rad
ρ	Angular radius of the Earth as seen from the satellite	rad
ρ_{avg}	Average range satellite-station	m
ρ_{SLR}	Two way range of SLR	m
σ	A priori standard deviation associated with the observation	-
θ	Pitch angle (rotation around Y axis)	rad
$\vec{b}$	Observation vector	-
$\vec{q}$	Quaternion vector of rotation	-
$r_{obs,\vec{com},i}$	Observation position vector between the station and the COM in an inertial frame	-

$\vec{r_{satellite,i}}$	Satellite COM vector in an inertial frame	-
$\vec{r_{station,i}}$	Station position vector in an inertial frame	-
$\vec{x}$	State parameter vector	-
$\vec{X}_{sim}$	Simulator state vector	-
C_i	Empirical acceleration cosine coefficient	-
C_x, C_y, C_z	Rotation amplitudes of Envisat	deg
df_{AL}	Apparent longitude frequency shift	Hz
df_{AP}	Apparent phase shift frequency	Hz
E_M	Input edit multiplier	-
E_R	Weighted RMS of the previous global iteration	-
i	Orbital inclination	rad
k_i	Time derivative at the nth point in the RK4 integrator	-
L_{node}	Longitude of ascending node	rad
$LON_{laser,sbc}$	Longitude change of the laser vector in the satellite orbit frame	rad
$LON_{laser,scs}$	Longitude change of the laser vector in the spin coordinate system frame	rad
q_v	Vector part of quaternions	-
$R_{\text{♁}}$	Earth's radius	m
S_i	Empirical acceleration sine coefficient	-
t_r	Receive time of a SLR signal	-
t_t	Transmit time of a SLR signal	-
$T_{apparent}$	Apparent spin period	s
$T_{inertial}$	Inertial spin period	s
T_{tot}	Total external torque	Nm
U_N	Unit vector in the normal direction	
U_R	Unit vector in the radial direction	-
U_T	Unit vector in the tangential direction	-
U_{lat}	Argument of latitude	rad
X_{if}, Y_{if}, Z_{if}	Coordinates in the ECEF if-frame	m
X_i, Y_i, Z_i	Coordinates in the inertial ECI i-frame	m
X_l, Y_l, Z_l	Coordinates in the local orbit l-frame	m
X_s, Y_s, Z_s	Coordinates in the ESA s-frame	m
$\mathbf{I}$	Mass moment of inertia matrix	kgm^2
$\mathbf{L}$	Angular momentum vector	Nms
$\mathbf{x}$	State vector	-

$\mathbf{y}$	Observation vector	-
$\mathbf{z}$	Observation model vector	-
A	Amplitude empirical acceleration	m/s^2
Az	Azimuth angle	deg
C	Computed observation	-
c	Speed of light	m/s
El	Elevation	deg
h	Step size	s
O	Observation	-
P	Orbital period of satellite	rad

1

Introduction

According to the World Commission on Environment and Development (WCED) (1987), the definition of sustainability may be defined as *"Development that meets the needs of the present without compromising the ability of future generations to meet their own needs"*. The space debris problem meets this definition. Space debris is defined as all man made objects including fragments and elements thereof, in Earth orbit or re-entering the atmosphere, that are non functional (Inter-Agency Space Debris Coordination Committee, 2007). The threat of possible collisions make it one of the largest space challenges of the upcoming decades.

1.1. Space debris and its attitude

With the increasing number of space objects every year, the problem of space debris is becoming a major threat in space. Especially the Low Earth Orbit (LEO) regime is the most affected region which holds about 79% of the total amount of traceable space objects from which about 78% is debris, 15% payload and 7% are left over rocket bodies (Peters et al., 2013). Collisions have already occurred in the past, like the 2009 Iridium 33- Kosmos-2251 collision in 2009 creating an enormous cloud of debris. Kessler and Cour-Palais (D. J. Kessler, 1978) already addressed in 1978 the cascading effect of a possible non-reversible collisional phenomena called the Kessler syndrome. The syndrome shows that a domino effect of collisions could occur. One of the major solutions, next to mitigation rules, lies in the active debris removal of uncontrolled space objects. Concepts like robotic-arm or net capturing techniques are currently being developed and assessed on their feasibility. One of the selection criteria is the rotational speed and state of the tumbling target object (Bonnal et al., 2013; Nishida and Yoshikawa, 2003).

To fill the time gap between the present and the actual active removal of a passive space object, accurate tracking of such objects remains of high importance when preventing collisions. Propagation accuracy of a passive object's orbit could possibly be increased when the rotational state is known and implemented in the orbit determination. On the other hand, passive objects can be treated as scientific cases in terms of assessing the effect of internal and external perturbations acting on the spacecraft. Lastly, the rotational evolution could explain possible end-of-life scenarios like debris impact.

This is only possible if the object is traceable to a certain accuracy. Luckily, some space debris satellites are equipped with passive tracking systems like the Satellite Laser Ranging (SLR) system, which uses the round-trip time of a laser pulse in order to accurately estimate the distance between the station and the object. The ESA satellite Envisat lost contact with Earth in April 2012 for a still unknown reason. Luckily it is equipped with a SLR system allowing it to be passively tracked. The chosen orbit was an initial sun-synchronous polar orbit at about 780 km altitude. Estimations revealed an expected orbital lifetime of about 150 years (Kirchner et al., 2013). Earth observation satellites are often put in these orbits creating a relativity high collision threat with Envisat in its expected lifetime. Luckily Envisat is regularly being tracked by several laser ground stations around the world. This data allows determination of Envisat's orbit. Laser ranging analysis has already shown that Envisat is rotating and slowly losing its rotational speed (Kucharski et al., 2014).

1.2. Research framework and objective

The use of SLR in attitude determination has shown its results in the past. The most prominent researchers include D. Kucharski, T. Schildknecht and G. Kirchner. These researchers have tried to estimate attitude states of space debris objects during the past years using various techniques. To which extent the outcome of their analysis corresponds to reality remains however unknown. The analysis performed so far was mainly focussed on assessing the rotational period and axis based on the data available. Whether or not the number of SLR passes of Envisat is sufficient for accurate attitude determination is a question which is still not answered. Also, whether or not SLR can be used as a stand-alone tool to asses attitudes states remains unknown. Furthermore, the evaluation of a COM-LRR correction for tumbling space debris remains not implemented in the orbit determination process, nor are its effect investigated properly. The research question of this MSc thesis has therefore been formulated as:

To which extent is it possible to use SLR for attitude determination of tumbling space objects equipped with a laser retro reflector?

The research objective of the thesis work is to gain more insight in the use of SLR data for gathering information regarding attitude states of passive space objects. The passive Envisat equipped serves as a perfect example for multiple reasons: First it posses a Laser Retro Reflector (LRR) and is tracked on a regular basis, such that a SLR data set is available. Next, Envisat is selected as a possible active debris removal target by the eDeorbit mission of ESA (European Space Agency, 2015) and it has already been found that Envisat is tumbling by Kucharski et al. (2014) which makes it possible to compare results.

The attitude of Envisat will be estimated using simulated laser ranging data which will be compared to real and simulated SLR data of the tumbling Envisat. The research will furthermore gain insights in the estimation process of the attitude state parameters and provide conclusions regarding the feasibility of the use of SLR for attitude determination.

1.3. Thesis outline

The thesis is structured in the following way: First an introduction about SLR and the Envisat spacecraft and its properties will be given in chapter 2. This chapter also describes the reference frames necessary for chapter 3. Here the set-up of the rotational model used for the attitude state of the spacecraft will be covered as will the chosen propagator briefly be explained and tested. Next the orbit determination procedures used in this thesis will be explained in chapter 4. From this chapter the main working product is developed, the range residuals. From these the apparent spin period is derived. Together with an elaborate station analysis, and the validation of the previously produced attitude model in GEODYN, the chapter is completed. Chapters 2,3 and 4 lead up to the the simulated attitude determination chapter 5. Here, the results are gathered, methods are evaluated and conclusions are drawn with the use of simulated data. Finally in chapter 6 real SLR data will be used in order to determine its attitude. The thesis will end with chapter 7 concluding all the work done and provide recommendations for further research in this field.

2

SLR and Envisat

"Sometimes you have to go up really high to understand how small you really are."
— *Felix Baumgartner,* Austrian extreme skydiver

SLR is the main measurement technique used in this thesis. This chapter will provide a brief overview about the measurement technique and its application on Envisat in section 2.1. All relevant reference frames will be addressed and labelled for this particular thesis in section 2.2. Furthermore, it will provide all relevant technical satellite information of Envisat with respect to the satellite laser ranging technique and its attitude modelling in section 2.3, after which the chapter will end with some preliminary conclusions in section 2.4.

2.1. Measurement technique- SLR

Next to radar, DORIS and GPS, laser ranging can be used as well in order to track a satellite's position. It follows the principle of measuring the two-way time of flight from a SLR ground stations to the retro reflector of a satellite in order to calculate the distance between both. The system thus relies on both a uplink as a downlink path. The retro reflector is designed in such a way that it reflects the laser pulse in almost the exact direction from which it comes. Envisat has one retro reflector as will be described in section 2.3.5. The round trip distance between the laser station and the satellite thus follows:

$$\rho_{SLR} = c(t_r - t_t) \tag{2.1}$$

Where c is the speed of light and t_r and t_t resemble the receive and transmit time respectively(measured by the same accurate clock (Tapley et al., 2004)). The range observations are a non-linear function of the actual state vector (position), with associated (systematic and random) errors. Using a two-way range system where the same clock is used cancels the clock offset which reduces the clock error significantly and only a linear clock drift and other small non-linear terms and stochastic components need to be included in the clock error component.

Equation 2.1 does not take into account the atmospheric refraction which slightly delays the signal. Using an appropriate atmospheric model and adding this correction to equation 2.1, the accuracy of the measurement can be increased. Typical accuracy is in the range of 1 cm for high precision laser up to about 20 cm for those with higher errors (de la Fuente, 2007). The use of an SLR system is thus dependant on the local weather conditions due to its use of the optical wavelength. SLR stations nowadays use a Nd:YAH (neodymium yttrium aluminium garnet) which operates at a (green) wavelength of about 0.532 micrometer (Tapley et al., 2004). Different type of laser repetition rates are used ranging from 10 Hz to 2 kHz and using short(10 ps to 100 ps) laser pulses (Kirchner et al., 2011). To be able to establish a link between the station and the satellite during a pass, accurate orbit (prediction) data must be available. The position must be known within a few-hundred meter diameter(at satellite altitude), in order to have a successful echo back to the ground station's receiver telescope (Tapley et al., 2004).

In order to find the true range between the satellite and the station, an iterative process is used by the orbit determination program. It compares the measured two-way-range to a computed value which results from a known satellite ephemeris, ground station coordinates and modelled errors. It is an iterative process due to lack of information of the time when the signal arrives at the satellite, which is a necessary piece of information in this calculation. According to Tapley et al. (2004) the average range(equation 2.2) can also be used which simplifies the process significantly.

$$\rho_{avg} = \rho_{SLR}/2 \tag{2.2}$$

The International Laser Ranging Service (ILRS) gathers and coordinates all the global satellite and lunar laser ranging data. This institute ensures all the SLR data is standardized and of sufficient quality. Next to providing ranging data for satellite orbits, the laser data is used for numerous scientific purposes like precise geocentric positions, components of Earth's gravity field and their temporal variations and Earth orientation parameters. The Consolidated Laser Ranging Data Format (CRD) format has been developed in order to achieve standardization of the laser data formats, which enables several institutions to work and implement data from all stations more easily (Pearlman et al., 2002). The CRD format will be addressed in section 4.1.1. Figure 2.1 shows all 51 SLR stations around the world which support the ILRS. It clearly shows the relatively high concentration of stations in Europe compared to the rest of the world. The sparse distribution is partially due to the high cost of operating and servicing a present complex SLR system (Degnan, 1994).

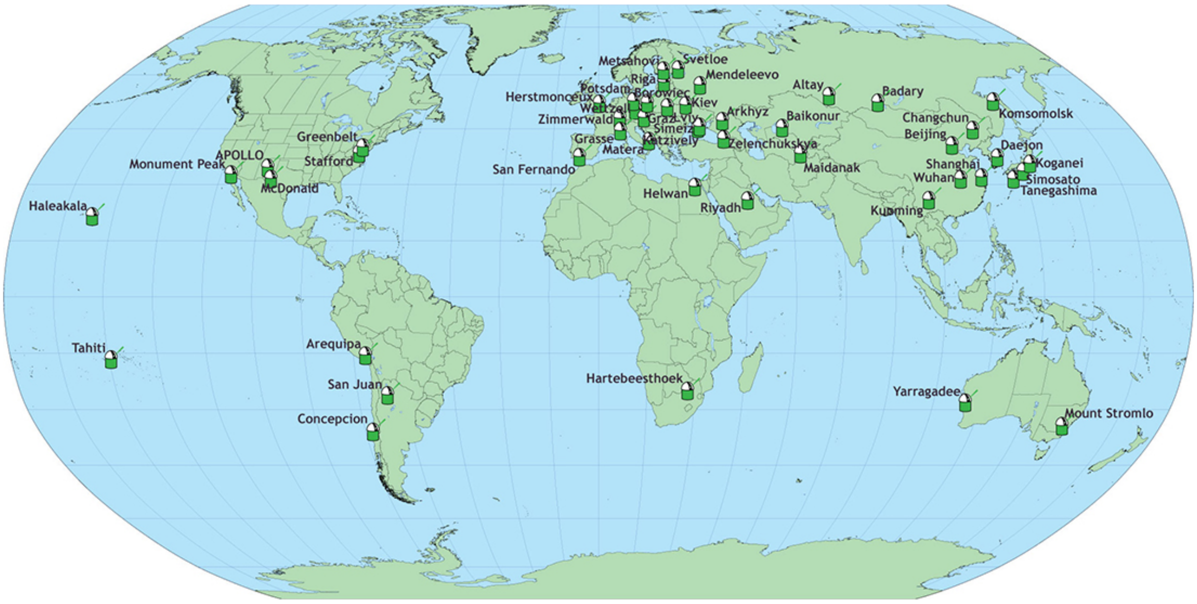

Figure 2.1: Global map showing all the participating SLR stations (Pearlman et al., 2002)

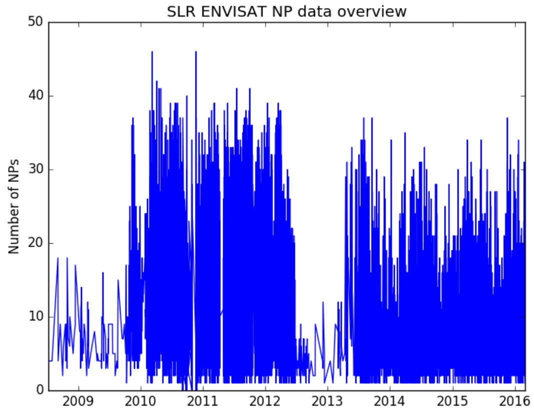

Figure 2.2: Envisat past SLR tracking

Envisat could be actively tracked using its DORIS system before 2012 during its active mission lifetime. The 50 ground beacons around the globe could cover about 75% of Envisat's orbit and resulted in an orbit accuracy of about 1 cm (ESA, 2002). The SLR measurements were performed as well in this active time span to further help increase and validate the orbit accuracy. According to the ILRS, Envisat was tracked up until June 2012 by 19 stations, after which Envisat was only tracked sporadically. In 2012 during the International Technical Laser Ranging Workshop it was suggested that SLR stations should remain trying to track the inactive Envisat (Kucharski et al., 2014). Apparently this was not enough to convince the entire global community as only a few stations directly followed this call. After DLR has taken initiative in May 2013 to keep on tracking Envisat, the ILRS asked the global network to resume tracking of Envisat past its end-of life after the 30st of May 2013 (Weigel et al., 2013).

This can be clearly seen in figure 2.2 where all the measured normal points for all stations are plotted in the period from 2009-2016. The loss of contact in April 2014 shows an abrupt stop of nearly all SLR tracking. DLR emphasizes that in order to predict Envisat's orbit (and attitude) to a higher extend than the Two-Line-Element (TLE) system and thus warn other satellites to a higher degree of accuracy, satellite laser ranging must be performed.
A drop in the priority list can be observed over the years from the ILRS priority list (Pearlman et al., 2002). Where Envisat was placed on the 21st position(of 40) on the priority list in May 2013, it has dropped to the 56th(of 61) in April 2016.

2.2. Reference frames

The most common used reference frames which are to be used throughout the report are defined below as the Envisat spacecraft fixed frame (f-frame), body fixed frame (b-frame), local orbit frame (l-frame) and an inertial orbit frame (i-frame). These conventions will be used throughout the report following the orientations as given in this section.

ESA Envisat spacecraft fixed frame (f-frame) This reference system is fixed to the body and defined by engineering drawings which are set during the design phase. For Envisat its origin lies in the center of the furthest point of the service module at the center of the launcher interface as shown in figure 2.3. The $+X_f$ direction lies along the satellite's longest direction(towards the solar array), $+Z_f$ points perpendicular to this direction in the direction outwards from the top side of the satellite and $+Y_f$ completes the right hand rule convention pointing along the direction of the ASAR.

Spacecraft COM body frame (b-frame) This frame is fixed to the satellite as well just like the f-frame but its origin lies in the center-of-mass position as will be given in section 2.3.6. The COM position is given with respect to Envisat's f-frame. The orientation of theses axes follow the same definition as was given for the f-frame. The body-fixed reference frame is illustrated in figure 2.4. All three principal axis are chosen to be perpendicular to the faces of the spacecraft bus.

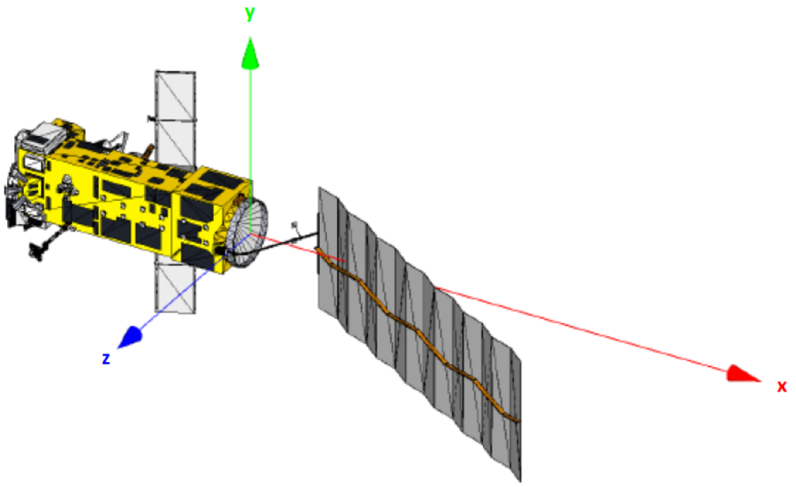

Figure 2.3: Envisat spacecraft fixed frame(f-frame) (B. Bastida Virgili, 2014)

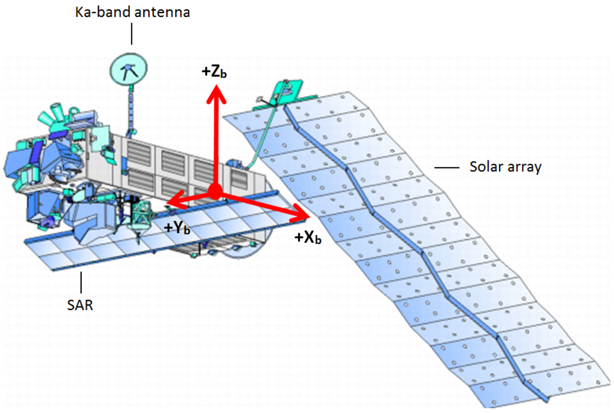

- $+X_b$: Longitudinal direction of the spacecraft bus towards the solar array
- $+Y_b$: Parallel to SAR antenna (long side) towards the left side with respect to the positive X_b direction
- $+Z_b$: Parallel to Ka-band antenna following a right-hand system

Figure 2.4: Envisat COM body frame(b-frame) (ESA, 2016c)

Local orbit coordinate frame (l-frame) and ESA frame (s-frame) This frame has its origin as well in the center of mass of the orbiting body, but is relative to the inertial coordinate system(i-frame). Its $+Z_l$ axis points in the radial direction, directly away from the center of the Earth towards the satellite's center of mass. The $+X_l$ axis points along the transversal direction in the osculating position/velocity plane such that it points perpendicular to Z_l-axis and positive towards the velocity vector. The Y_l axis follows the right-hand rule and lies in the cross-track or out of plane direction. For an eccentric orbit, the along-track and radial direction are not perfectly perpendicular(except at apogee and perigee). It is therefore necessary to chose two of these axis as the principal ones, where the other follows from the vector cross product of these chosen axes in order to result in a orthogonal system (Doornbos et al., 2013). The Z_l direction is chosen to be truly radial, from which the cross-track/normal Y_l follows. The X_l along-track direction is therefore chosen to be pseudo-along-track. The local reference frame(l-frame) is shown in figure 2.5. On the right side, figure 2.6 is shown, which is the standard satellite reference frame of Envisat as defined by the mission conventions of ESA (Alvarez, 1997). It shows strong resemblance with the previously defined l-frame. Both are centred in the satellite's center of mass, both have their Z-axis pointing in the radial direction, positive from the center of the Earth towards the satellite, and both are based on the specific osculating orbital plane. However, the l-frame has its along-track axis pointed in the positive velocity direction, whereas the ESA frame has its along track direction in the negative velocity direction. Furthermore, the X and Y conventions for both frames are switched such that X_s corresponds to Y_l and X_l to $-Y_s$. Table 2.1 summarizes both frames and their conventions.

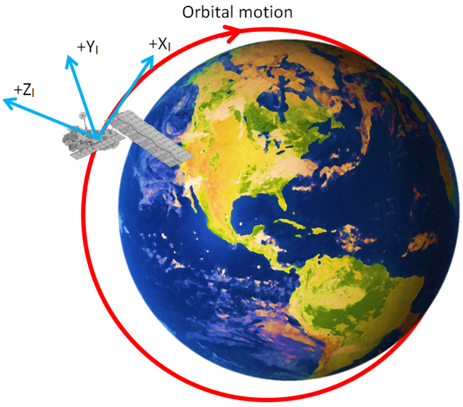

Figure 2.5: Local orbit frame(l-frame)

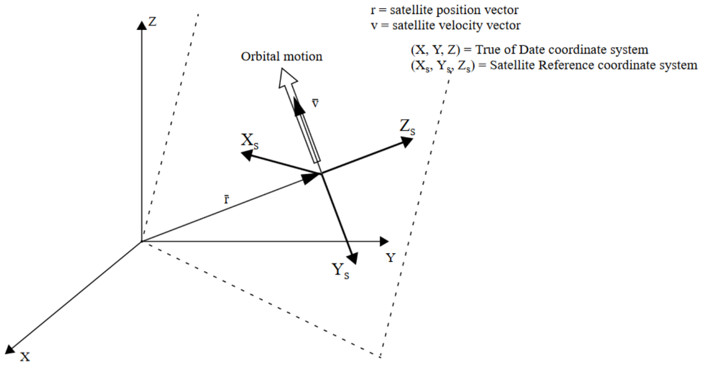

Figure 2.6: ESA Envisat's reference coordinate frame(s-frame) (Alvarez, 1997)

Table 2.1: Difference between l-frame and s-frame

Direction	l-frame	s-frame
Along-track(pseudo)	$+X_l$	$-Y_s$
Cross-track(true)	$+Y_l$	$+X_s$
Radial(true)	$+Z_l$	$+Z_s$

Satellite relative reference frame (s'-frame) The satellite relative reference frame is obtained by rotating the s-frame by three consecutive rotations over a roll angle around the Y_e axis, over a pitch angle around the X_e axis and over a yaw angle around the Z_e axis. The order in which this should occur depends on the attitude law as will be discussed in section 2.3.7. If the axes of the body fixed b-frame are initially aligned with the ESA orbit s-frame, then the e'-frame corresponds to the b-frame.

Reference inertial coordinate frame (i-frame) As an inertial reference frame, the Earth Centered Inertial (ECI) frame is chosen and will be further referenced as the i-frame throughout this thesis. A non-rotating frame is a common used frame when considering orbital space objects (Wertz, 2009). Due to precession(conical motion of the spin axis), nutation(perturbations in the conical motion) and the acceleration of the Earth around the sun, this system is however a pseudo or quasi inertial reference frame. Its origin is located in the center of mass of the Earth as shown in figure 2.7. The X_i axis points in the direction of the mean equinox(at J2000.0 epoch). This fixed specific epoch at the equinox and equator is necessary due to precession and nutation which exert a variation in the location of the vernal equinox. The J2000 system is defined as the reference mean equator and equinox on the 1st of January, 2000, 12 hrs (Tapley et al., 2004). The Z_i axis is orthogonal to the plane as defined by the mean equator at J2000.0 epoch and coincides with the rotational axis of the Earth. The Y_i axis follows the right-hand orientation convention which completes the orthogonal reference frame. This frame will be used throughout the thesis as the iJ2000-frame. Another representation often used in orbit determinaton, is the True of Date (TOD) format, where the true equator and equinox at a specific date is used. Whereas the J2000 system is fixed in space, the TOD equinox changes slightly over time due to the precession of the ecliptic pole with a period of 26,000 years which shifts the vernal equinox (Wertz, 2009). This frame will be referenced as the iTOD-frame throughout the thesis.
An Earth Centered Earth Fixed (ECEF) frame (if-frame) will be used as well in this thesis. Opposed to the ECI frames, the ECEF frame co-rotates with the Earth around the Z_{if} axis with a constant angular velocity. The X_{if} axis is located at the intersection of the orthogonal plane to the Z_{if} and the Greenwich mean meridian as shown in figure 2.8. The Y_{if} axis follows as it is orthogonal to both Z_{if} and X_{if}. This frame is commonly used when considering positions with respect to the Earth's surface like longitudes and latitudes of for instance station positions. The International Terrestrial Reference Frame (ITRF) is a common used ECEF frame maintained by the International Earth Rotation Service (IERS). Coordinates are fixed on a reference surface which undergo only small variations like tectonic or tidal deformations.

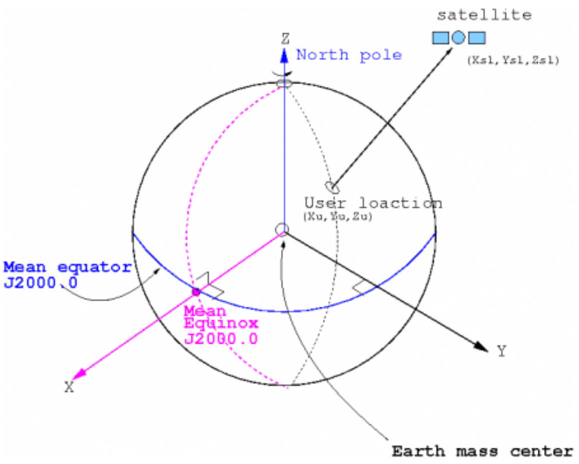

Figure 2.7: ECI i-frame (ESA, 2016b)

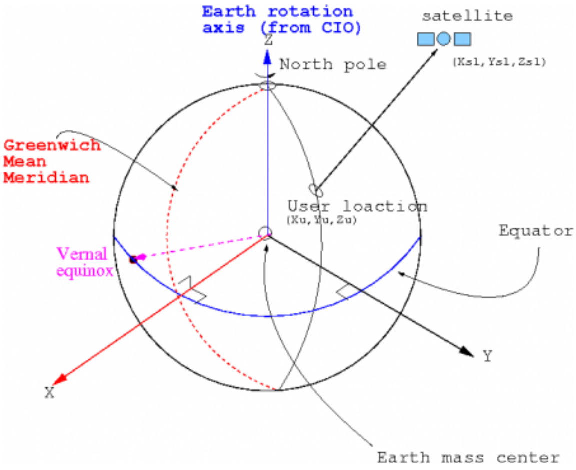

Figure 2.8: ECEF if-frame (ESA, 2016b)

2.3. Envisat

Designed as the successor of the European Remote Sensing (ERS) satellites, Envisat was the largest civilian Earth observation mission of the European Space Agency (ESA). It served the scientific community greatly by collecting an astonishing amount of data in its 10 year operational lifetime (2002 – 2012). With its eight-tonne mass it nowadays orbits the Earth uncontrolled as a piece of space debris after contact was suddenly lost in April 2012. All possible means to re-establish contact have failed and the object can be regarded as one of the largest pieces of space debris.

The following section covers all relevant information of Envisat for this thesis. First, the orbit of Envisat, its dimensions and a brief overview of its solar panel and possible left over fuel will be given. Next the retro reflector will be covered after which the section will end with Envisat's current mass distribution, its active attitude modes and a simplified panel model which will be used in chapter 4 during the orbit determination.

2.3.1. Orbit

Envisat was launched on the first of March 2002 in its original sun-synchronous frozen orbit at an altitude of about 800 km and a repeat cycle of 35 days. Such orbits have the key advantage that the orientation of the orbit plane with respect to the Sun remains approximately constant. This is achieved by Earth's oblateness which causes the orbit to rotate in inertial space with about the same period it takes the Earth to complete a full cycle around the Sun. This orbit is especially popular for Earth observation missions as a nearly constant Sun angle is maintained which allows easier interpretation of pictures over time. The corresponding orbital elements are given in table 2.2. Due to perturbations acting on the spacecraft, inclination changes were necessary to keep its orbit stable. These were abandoned in 2010 in the second mission stage where the orbital altitude was decreased with 17km in order to save fuel which resulted in a 30-day repeat cycle (ESA, 2016a). This phase can be seen in figure 2.9 where it is given by Phase E3. Due to aerodynamic drag, Envisat's orbital height is slowly decreasing, as well are its inclination and eccentricity slightly drifting as is given in table 2.2.

Table 2.2: Envisat orbital elements pre and post 2012

Orbital element	Nominal (<2012) (DLR-IMF, 2016)	Current (2016) (Peat, 2016)
Semi-major axis [km]	7159	7144
Inclination [deg]	98.55	98.28
Eccentricity [-]	0.001165	0.001357
Argument of perigee [deg]	90.0	83.21
Orbital period [min]	100.6	100.14

The drifting of Envisat's orbit due to several perturbations like the zonal harmonics, aerodynamic drag and solar radiation pressure result in the drifting of Envisat's orbit which violates its original sun-synchronous orbit condition. Furthermore a small decrease in orbital altitude can be witnessed, however this remains still small for the past few years.

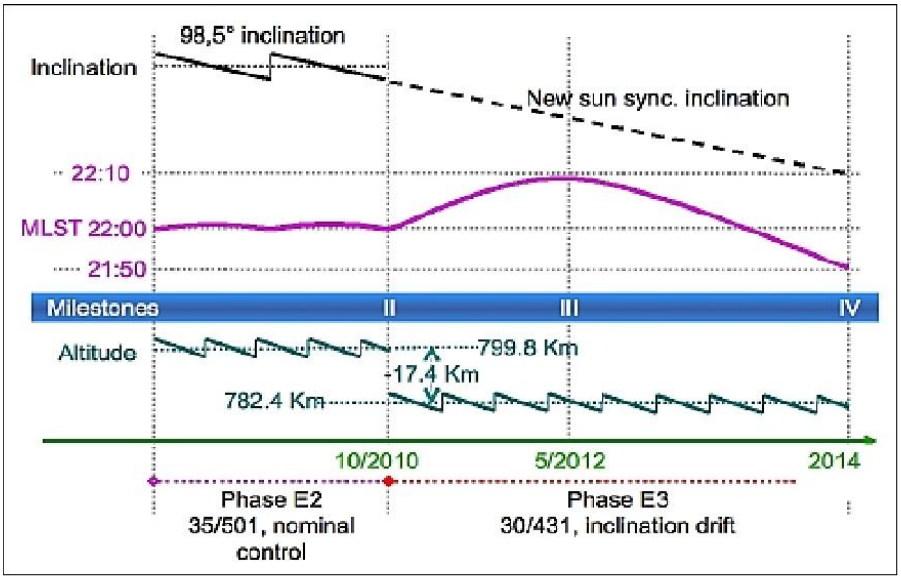

Figure 2.9: Schematic view of Envisat orbit changes (ESA, 2016a)

2.3.2. Dimensions

The following figures 2.10 and 2.11 show the general top and side dimensions of Envisat. The big Envisat satellite consists of three main parts, that is the main bus which holds the payload and the service module, the Advanced Synthetic Aperture Radar (ASAR) and the large tennis-court sized solar panel.

A measure in passive de-orbiting studies due to aerodynamic drag is the area-to-mass ratio (A/m). As Envisat's attitude affects the area being exposed, its exact A/m varies with time due to its attitude and solar array position. Based on simplifications, one could asses possible ranges wherein it varies. The top view in figure 2.10 clearly shows one of the largest area states. Combining the body, ASAR and solar panel, a total area of about 108 m^2 can be found. On the other hand, if one assumes the side view as in figure 2.11, a total area of about 26 m^2 is found. When considering a total mass as indicated in section 2.3.6 of 7827 kg the corresponding A/m would lie somewhere in the range of 0.0033 and 0.013 m^2/kg respectively. The A/m values are off course highly dependant on the solar array position, as it rotates towards the sun during an orbit as will be shown in the proceeding section 2.3.3. The specific values of area affect the drag and solar coefficients and thus the (long-term) predictions. Weigel et al. (2013) uses a a simplified cannon-ball model with an average cross-sectional area of 26 and 20 m^2 respectively for the drag and solar coefficient estimation in the orbit determination and prediction process. These values resemble almost the smallest possible surface areas. An along-track prediction error of about 200 m was found in 2013.

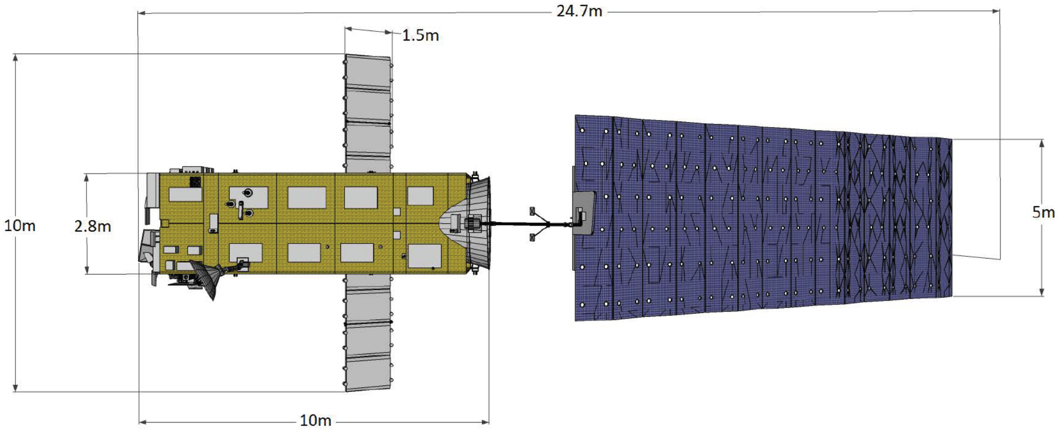

Figure 2.10: Top view of Envisat (Deloo, 2014)

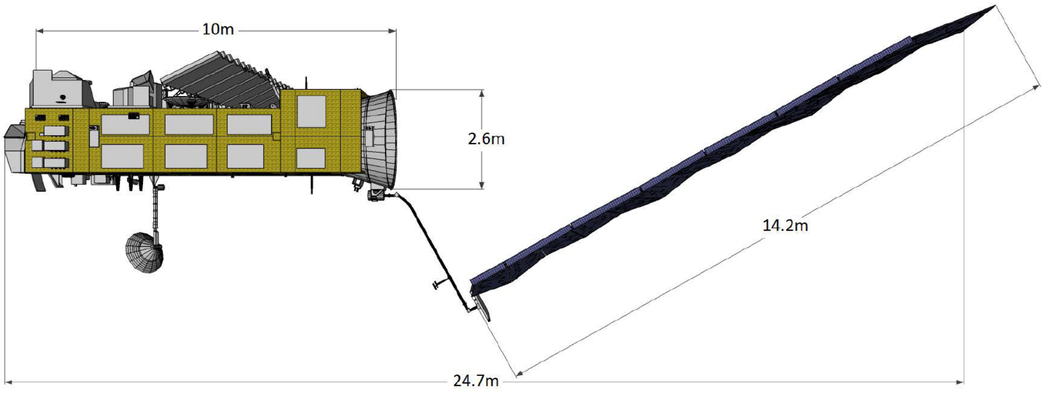

Figure 2.11: Side view of Envisat (Deloo, 2014)

2.3.3. Solar Panel

The foldable solar panel of 5x14m is designed as a movable part in order to rotate itself perpendicular to the sun at any point in the orbit while the spacecraft is kept nadir pointed at all times. This constant rotation rate is taken care of using the solar-array drive mechanism (ESA, 2016a). It moves from canonical position to canonical position. That is, when the normal to the solar array lies in the X_b-Z_b plane(b-frame see section 2.2), and points away from the Earth(at descending node). Due to seasonal variations the time of canonical position varies(when the true sun crosses the X_b-Z_b plane). The rotation rate needs thus to be slightly updated every orbit. According to Inverse Synthetic Aperture Radar (ISAR) and optical space-based images(figure 2.12) taken after April 2012, the solar panel was found not to be rotating and fixed in an anti-canonical position according to Lemmens et al. (2013). This is the exact opposite from the so-called safe-mode which was expected to be observed.

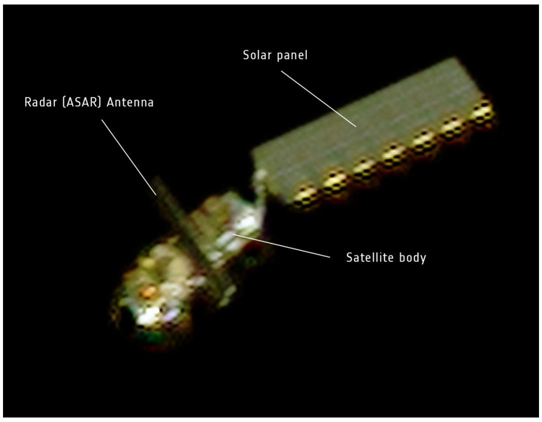

Figure 2.12: Pleiades image 15/04/2012 (ESA, 2012a)

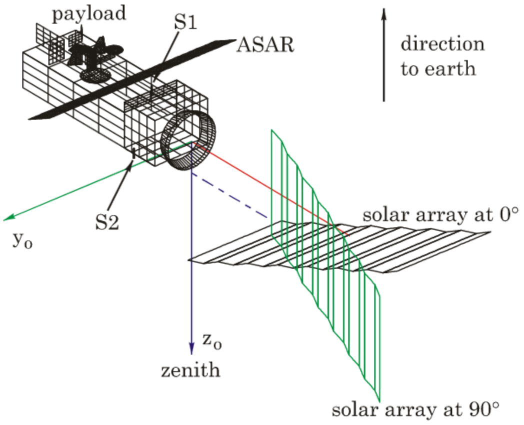

Figure 2.13: Solar panel orientation (Jensen, 2005)

Envisat is equipped with a so-called "safe-mode" attitude mode. This ensures that the Spacecraft's $Z_b(+)$ axis(b-frame see section 2.2 is pointed towards the sun, while the entire spacecraft rotates at a rate of 0.5° per second about the $Z_b(+)$ axis (Harvey et al., 1997). The rotation of the solar panel can be seen in figure 2.13. The solar panel is fixed under a constant angle of 22° with respect to the X_f-axis of the satellite as shown in figure 2.11. This angle is chosen as it aligns the solar panel perpendicular to the direction of the sun in the nominal orbit where the bodies positive X-axis always lies in the positive normal direction of the local orbit frame. It is directly linked to the nearly constant Sun angle as was discussed in section 2.3.1.

2.3.4. Propulsion system

Figure 2.14: ENVISAT service module (ESA, 2016a)

Envisat is equipped with four propellant tanks, which were fuelled at launch with about 314 kg of hydrazine mono propellant (ESA, 2016a). They are located on top of the service module cone as shown in figure 2.14. Based on the fuel consumption as will be given in section 2.3.6, about 35 kg of hydrazine remains still in the tanks. These hydrazine tanks are protected by thermostat-controlled heaters and is believed to remain pressurised (op till date) as they were working in a so called blow-down mode during communication loss (ESA, 2012b). This means, the propellant and the pressured gas are stored in the same tank, resulting in a pressure drop over time when propellant is burned. Current estimations state that the pressure inside the tanks is about six bar. This is quite low if one compares this to the Beginning of life (BoL) tank pressure, which was about 24 bar (ESA, 2012b). ESA analysed four possible failure modes of the propulsion system. These include structural degradation, collision, ignition and overpressure.

Even though Envisat has spend more than double its original planned lifetime in orbit, the corrosive agents like hydrazine are not regarded as a possible degradation cause as the tanks are designed for long service life. Furthermore, a possible collision is given a very low likelihood. Next, in order to have an ignition of the propellant, the hydrazine should be in its liquid/gas state. Due to the lack of thermal control, the propellant must be frozen, furthermore the batteries are believed to be fully discharged so a possible interference was discarded by ESA. Finally, overpressure was not considered as an option as well due to the fact that an increase of temperature greater than 100 K would be necessary to raise the tank pressure to over its design level of 24 bar (ESA, 2012b).

2.3.5. Retro reflector

Figure 2.15 shows a SLR station in contact with Envisat during nominal operations where the 20 cm diameter LRR is kept nadir pointed as it is mounted on the bottom(nadir) side of the bus. Its design holds eight symmetrical(and one nadir pointed) orientated Corner Cube Reflector (CCR) as illustrated in figure 2.16. Distance of each reflector to the LRR reference point as given in table 2.3 is azimuth dependent and varies from 48.7 to 53.7 mm (Pearlman et al., 2002). Envisat can be laser tracked at a full 360° (azimuth range) and has an half-cone angle of 60° (elevation range) (ESA, 1998). The current tumbling situation allows Envisat not to be tracked at every instant due to these restrictions and its position on the bus. The viewing cone information is an important parameter in the simulation and attitude determination process.

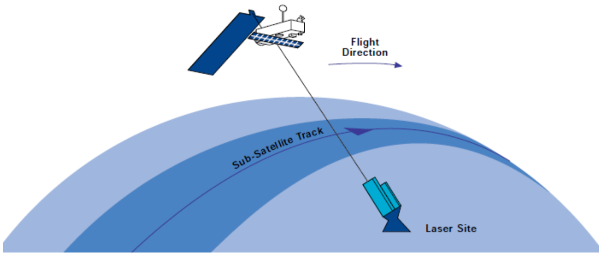

Figure 2.15: Nominal SLR condition (ESA, 1998)

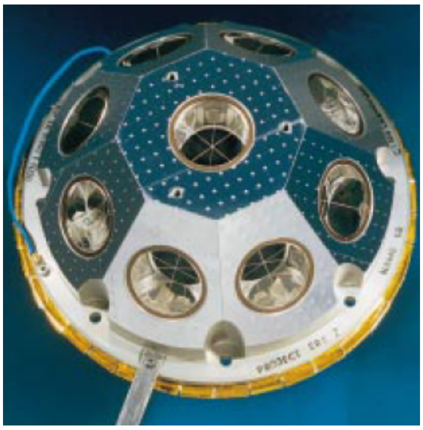

Figure 2.16: Laser Retro-Reflector (ESA, 1998)

The LRR is located from the satellite coordinate origin according to the Envisat f-frame as defined in section 2.2 and given in table 2.3.

Table 2.3: LRR array offset in Envisat f-frame (Pearlman et al., 2002)

Direction	X [m]	Y [m]	Z [m]
Value	-4.920	+1.350	-1.180

The LRR has an efficiency of less or equals than 0.15 at end-of-life and its reflection coefficient is less or equal than 0.80 at end-of-life (ESA, 2002). According to Degnan (1985), SLR devices typically have a quantum efficiency of about 10-15 percent(which resembles the ration of emitted electrons to the number of incident photons). The working principle of the SLR with a LRR is based on the round-trip time of a laser pulse from a ground station. The corner cubes are designed in such a way that it will reflect the lase pulse parallel to the direction from which it came, such that the laser station can detect the incoming signal. Due to the velocity of the satellite, there exists a position difference in the time of emission and reception of the laser pulse which is about 40 m for Envisat (ESA, 2002). The CCR's are designed in such a way that it compensates for this by reflecting the beam slightly non-parallel.

2.3.6. Mass distribution

The exact location of the center of mass is an important property in all flight dynamics operations. Due to depletion of fuel and orientation of the solar panel, this location varies over time. Based on the information from the ILRS, the Center of mass (COM) location variations can be illustrated in figure 2.17. All distances are measured in Envisat's fixed f-frame as defined in section 2.2. Its initial and final mass as well as the initial and final center of gravity location(defined in the f-frame) are given in table 2.4 together with the variation of the relative offset between the COM and the LRR.

Table 2.4: Evolution of COM location and total mass in f-frame (Pearlman et al., 2002)

	Initial	Final
X_{com} [m]	-4.3650	-3.905
Y_{com} [m]	-0.0020	-0.009
Z_{com} [m]	-0.0390	0.003
m_{tot} [kg]	8106.4	7827.86
COM-LRR |offset| [m]	1.854	2.068

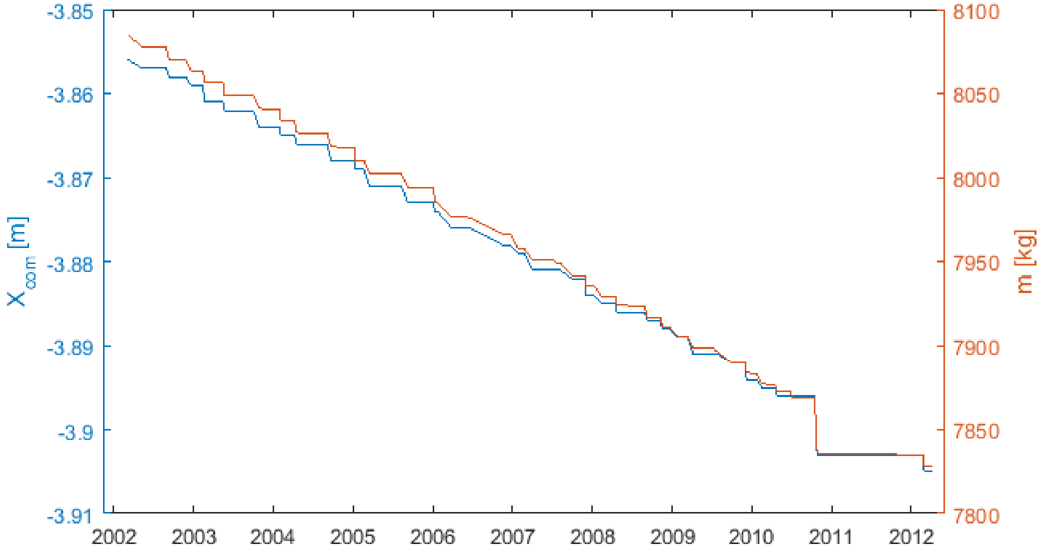

Figure 2.17: COM variation in X_f direction over Envisat's lifetime

Figure 2.17 clearly shows a different initial X_f-position of the center of mass. This might be explained due to the unfolding of the solar array during the first stage of the mission which shifts the center of mass in the positive X_f direction. A small difference in initial total mass can be seen as well between figure 2.17 and table 2.4 which might be explained due to initial orbit manoeuvres during the first phase of the mission which consumes a bit of fuel. The big step around October 2010 indicates the lowering of Envisat's orbit with 17.4 km (ESA, 2016a). After that phase, no further inclination correction burns where performed as can be seen at the stable evolution after October 2010. A small change drop is however visible on the first of March 2012. When looking at the manoeuvre history file from the ftp servers from the International Doris Service (IDS) the entire manoeuvre history of Envisat can be plotted in radial, along-track and cross-track direction in figure 2.18.

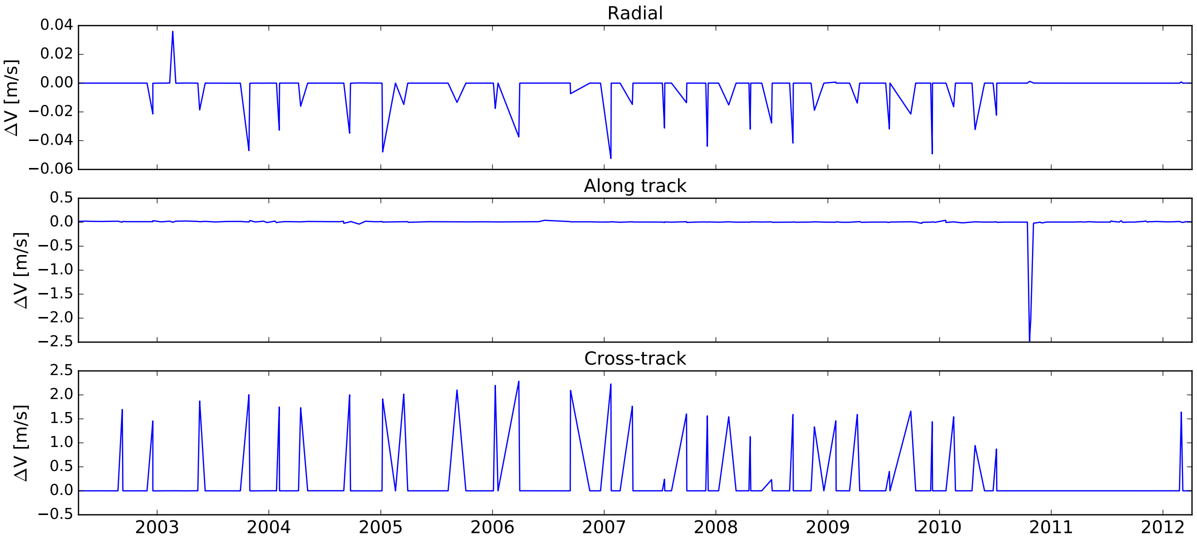

Figure 2.18: Manoeuvre history burns Envisat 2002-2012 in all three directions in the ESA defined s-frame

This overview shows that the total mass and center of mass variation in March 2012 are due to a large burn of about 1000 seconds in the cross-track direction which results in a total ΔV of 1.64 m/s as can be seen on the right hand side of figure 2.18. Cross-track(or out-of- plane) burns are mainly in charge of inclination corrections. These burns took place about three times a year as can be seen in figure 2.18 and as was mentioned by Rudolph et al. (2005b). This is contradictory to the previous mentioned fuel-saving phase which would cancel all inclination changes after October 2010.

The $\mathrm{Y_f}$ and $\mathrm{Z_f}$ components of the COM location barely change over time. If one continues to assume no further leakage of fuel or significant degradation the COM location can be regarded constant past April 2012 (ESA, 2012b).
The corresponding moments of inertia of Envisat are given in table 2.5.

Table 2.5: Moment of Inertia's of Envisat (B. Bastida Virgili, 2014)

I_{xx} $[kgm^2]$	I_{yy} $[kgm^2]$	I_{zz} $[kgm^2]$	I_{xy} $[kgm^2]$	I_{yz} $[kgm^2]$	I_{zx} $[kgm^2]$
17023.3	124825.7	129112.2	397.1	344.2	-2171.4

As the center of mass location depends mainly on the amount of fuel burned, this must be given careful consideration. Bargellini et al. (2006) already mentioned in 2006, a fuel usage uncertainty of about 3%.Furthermore, the assumption of the anti-canonical position could introduce another small deviation in the exact moment of inertia.
A common simplification implies re-writing the full inertia tensor to its principal axes only. These three orthogonal axes are defined in such a way that their products of inertia are zero, and therefore the inertia matrix becomes diagonal. This full moment of inertia term can be re-written to the principal axes of inertia using the eigen-decomposition of the inertia tensor as

$$I = VDV^T \tag{2.3}$$

Where D represents the principal axes inertia matrix(eigenvalues) and the columns of V represent the direction of the axes(eigenvectors) such that

$$\begin{bmatrix} 17023.3 & 397.1 & -2171.4 \\ 397.1 & 124825.7 & 344.2 \\ -2171.4 & 344.2 & 12911.2 \end{bmatrix} =$$

$$\begin{bmatrix} -0.998 & 0.0052 & -0.0190 \\ 0.0037 & 0.9970 & 0.0771 \\ -0.0194 & -0.0770 & 0.9968 \end{bmatrix} \begin{bmatrix} 16979.74 & 0 & 0 \\ 0 & 124801.21 & 0 \\ 0 & 0 & 129180.25 \end{bmatrix} \begin{bmatrix} -0.998 & 0.0052 & -0.0190 \\ 0.0037 & 0.9970 & 0.0771 \\ -0.0194 & -0.0770 & 0.9968 \end{bmatrix}^T \tag{2.4}$$

Due to Envisat's semi-axi symmetrical shape the principal axes lie almost perfectly in the direction of the body-axis principal axes frame as is seen from the eigenvector V. Throughout the thesis, both inertia expressions(full and principle-axes only) will be used.

2.3.7. Attitude mode

Due to orbital perturbations and technical constraints of the instruments, Envisat had to perform several burns in order to correct for these perturbations and to stay in a more or less stable orbit. The orbit control strategy was designed in such a way to achieve the requirement of a one kilometre deadband accuracy within its stable reference orbit (Rudolph et al., 2005a). Next to orbital manoeuvres, attitude stabilisation was necessary as well. Controlling the stable attitude was performed by reaction wheels/magnetic torquers and hydrazine thrusters (Gottwald et al., 2010). The 3-axis stabilized attitude mode is chosen such that its local relative orbital reference coordinate frame forms an orthogonal right-handed system as defined in the spacecraft body frame(b-frame) in figure 2.4.

Stellar Yaw Steering Mode The Stellar Yaw Steering mode during nominal operations is used most often as it offers the best pointing performance (Gottwald et al., 2010). Yaw steering(around Envisat's body fixed Z_b-axis) is required by the microwave imaging instrument to compensate for the rotational velocity of the Earth at the sub-satellite point. The rotational transformation is a combination of roll, pitch and yaw, which imposes a sinusoidal wobble of the platform around the flight direction. Maximum yaw amplitude is about

±3.92° (Gottwald et al., 2010).
The following rotations are defined in the ESA-defined s-frame and follows a specific rotation order. First rotating around Z_s over a positive yaw (ψ) angle, then around X_s over a negative pitch (θ) angle and finally around Y_s over a negative roll (ϕ) angle respectively in order to transform the satellite reference frame to the satellite relative reference(s-frame to s'-frame, see section 2.2). Equation 2.5 shows the appropriate transformation expression and equations 2.6, 2.7 and 2.8 the corresponding rotation angles.

$$\hat{r_{e'}} = R_z(\psi)R_x(-\theta)R_y(-\phi)\hat{r_e} \tag{2.5}$$

$$\phi = C_y \cdot \sin(U_{lat}) \tag{2.6}$$

$$\theta = C_x \cdot \sin(2U_{lat}) \tag{2.7}$$

$$\psi = C_z \cdot \cos(U_{lat}) \cdot [1 - (C_z \cdot \cos(U_{lat})^{2/3}] \tag{2.8}$$

Where U_{lat} represents the satellite osculating true latitude in the true of date coordinate system and the coefficients C_z,C_y and C_z represent the rotation amplitudes which are given to be +0.1672°, -0.0501° and +3.9130° respectively (Alvarez, 1997). Using star trackers and two gyro's, Envisat's highly accurate yaw steering mode (pointing accuracy requirement of about 0.035 °for each axis) is achieved using the reaction wheel actuators (Bargellini et al., 2006).

Satellite Safe mode Next to the Stellar Yaw Steering mode, a satellite safe mode existed. This mode had to ensure a survival state after a major anomaly. The mode was programmed in such a way that the Z_b face was pointed heliocentric, together with a spinning motion around the Z_b axis as was mentioned briefly in section 2.3.3

2.3.8. Panel model

Next to a simple cannonball model(where the entire spacecraft is modelled as a simple sphere with constant cross-sectional area), a more sophisticated spacecraft model can be used. Envisat's 6+2 face macromodel of plate surfaces as defined by Centre National d'Etudes Spatiales (CNES) can be found in table 2.6. The normal direction is defined according to the body-fixed frame(b-frame) as defined in section 2.2.

Table 2.6: 6+2 macromodel Envisat (Cerri et al., 2016)

		Normal in sat ref frame			Reflectivity properties		
nr	Surface $[m^2]$	x	y	z	Specular	Diffuse	Absorption
Main bus							
1	15.64	1	0	0	0.1170	0.4510	-0.0780
2	15.64	-1	0	0	0.0980	0.4340	0.0370
3	22.92	0	1	0	0.1460	0.4590	0.2040
4	22.92	0	-1	0	0.1460	0.4420	0.2220
5	38.26	0	0	1	0.1840	0.2640	0.4010
6	38.26	0	0	-1	0.1630	0.2740	0.4060
Solar panel							
7	71.12	towards the sun			0.2080	0.0520	0.7400
8	71.12	opposite to the sun			0.1120	0.4480	0.4400

Next to surface area's the reflectivity properties of each panel are given by the macromodel as well. These are used by the solar radiation pressure coefficient estimation process in the orbit determination process. The total pressure(or force when the effective cross-sectional area is taken into account) consists of three parts: specular reflection, diffuse reflection and absorption as illustrated in figure 2.19. During a shadow-pass the torque exerted on the spacecraft due to the solar radiation pressure is zero.

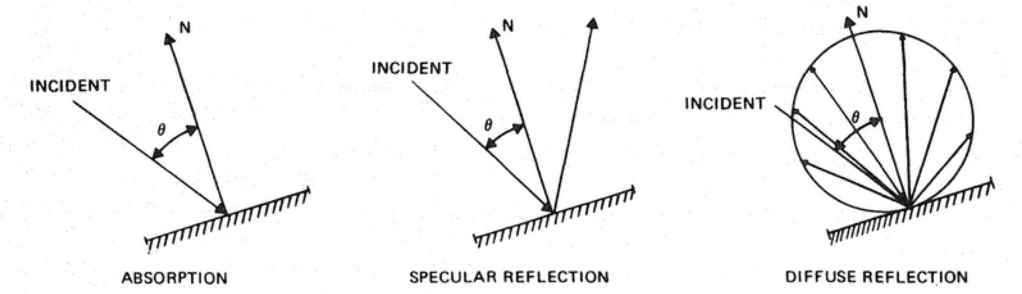

Figure 2.19: Absorption and reflection types of incident radiation (Wertz, 2012)

This model can be used in the orbit determination process by GEODYN. The normal of the solar panel however needs to be processed according to the new passive state. The following calculations are based on the assumption that the solar panel is fixed in its anti-canonical position as shown in figure 2.20.

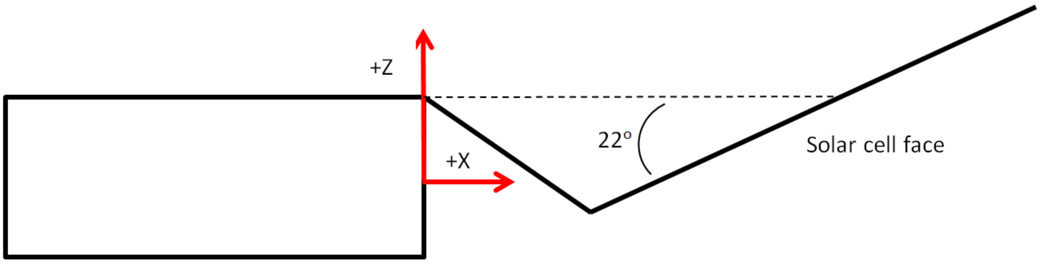

Figure 2.20: Anti-canonical position of Envisat

The Z and X component of the normal in Envisat's f-frame easily follow from the sine and cosine of 22° respectively. This results in the following passive solar panel macro-model as given in table 2.7.

Table 2.7: Macromodel Envisat solar panel (Cerri et al., 2016)

		Normal in sat ref frame			Reflectivity properties		
nr	Surface $[m^2]$	x	y	z	Specular	Diffuse	Absorption
Solar panel							
7	71.12	$\cos(22°)$	0	$-\sin(22°)$	0.2080	0.0520	0.7400
8	71.12	$-\cos(22°)$	0	$\sin(22°)$	0.1120	0.4480	0.4400

2.4. Conclusion

The past chapter has shown the past and actual state of Envisat with all its relevant information for the current thesis work. After failure in 2012, the large spacecraft started drifting away from its original sun-synchronous orbit. Several observations where made after which it was observed Envisat failed to enter in the so-called safe-mode. The solar-panel is assumed to be locked and fixed in its anti-canonical position. All propellant is furthermore assumed to be in the frozen state which greatly simplifies the model to a rigid spacecraft. Finally all relevant center-of-mass information together with the retro reflector location are given as well. Finally a macro model has been presented which represents the passive state of Envisat which can be used by the orbit determination process.

3

Rotational dynamics

"Who would not rather have the fame of Archimedes than that of his conqueror Marcellus?"
— *William Rowan Hamilton,* Inventor of quaternions

This chapter will discuss the approach used to set up a rotational model of Envisat. It is divided in the following structure. First the equations of motion of a torque-free rigid body will be defined in section 3.1, after which these will be implemented in the attitude integrator in section 3.2. The integrator will then be tested, validated and evaluated in section 3.3. The chapter will end with a few simulations of specific Envisat examples and show the rotation of the LRR around its COM in section 3.4.

3.1. Equations-of motion

The kinematic equations of motion used throughout this section are based on the work of Wertz (2012). First a suitable attitude parametrization technique must be selected. Wertz (2012) mentions several different attitude parametrization techniques, but chooses the Euler symmetric parameter or quaternion representation as the most suitable one for spacecraft kinematics analysis. The biggest advantage is the fact that it remains singularity free compared to Euler angles, Rodrigues parameters and Modified Rodrigues Parameters and requires less computational effort. These four quaternion parameters are given by:

$$q_1 = e_1 \sin\frac{\Phi}{2} \tag{3.1a}$$

$$q_2 = e_2 \sin\frac{\Phi}{2} \tag{3.1b}$$

$$q_3 = e_3 \sin\frac{\Phi}{2} \tag{3.1c}$$

$$q_4 = \cos\frac{\Phi}{2} \tag{3.1d}$$

The parameter ϕ indicates the Euler angle, which follows Euler's Rotation Theorem *"The most general displacement of a rigid body with one point fixed is a rotation about some axis".* The vector ê represents a vector along the axis of rotation and is composed of three components($\mathrm{e}_1, \mathrm{e}_2, \mathrm{e}_3$). The complete quaternion representation thus consists of a vector part($[q_1, q_2, q_3]$) and a scalar part(q_4). Equations 3.1 satisfy the following relation denoted as the unit quaternion rule which has a norm which equals one.

$$q_1^2 + q_2^2 + q_3^2 + q_4^2 = 1 \tag{3.2}$$

A complete quaternion representation is often given in matrix form as shown in equation 3.3.

$$\mathbf{q} = \begin{bmatrix} q_1 \\ q_2 \\ q_3 \\ q_4 \end{bmatrix} = \begin{bmatrix} q_v \\ q_4 \end{bmatrix} \tag{3.3}$$

3.1.1. Dynamic equations of motion - Torque free

The most simple case in attitude dynamics is the motion of a rigid rotating body in space entirely free from perturbations, external forces or torques. This assumption is chosen, as most passes only cover a couple of minutes and Envisat's orbit is located at 800 km altitude, where aerodynamic, solar and gravity-gradient angular accelerations are in the order of 10^{-10},10^{-9} and 10^{-6} $1/s^2$ respectively (B. Bastida Virgili, 2014).

From Euler's equations, the dynamic equations of motion of a rigid spacecraft are given as:

$$\frac{d}{dt}\mathbf{L} = T_{tot} - \omega \times \mathbf{L} \tag{3.4}$$

Where the angular momentum vector **L** equals

$$\mathbf{L} = \mathbf{I}\omega \tag{3.5}$$

Where the spacecraft's angular velocity vector ω needs to be resolved in the body-fixed reference system(b-frame). The total torque(T_{tot}) in equation 3.4 includes all the internal and external torques. **I** represents the inertia matrix of the rigid body about a body-fixed reference frame with the origin in its center of mass and consists of the following elements:

$$I = \begin{bmatrix} I_{xx} & I_{xy} & I_{xz} \\ I_{yx} & I_{yy} & I_{yz} \\ I_{zx} & I_{zy} & I_{zz} \end{bmatrix} \tag{3.6}$$

The dynamic equations of motion can be written in their full form as follows from equation 3.4 and 3.5:

$$\frac{dI\omega}{dt} = -\omega \times I\omega \tag{3.7}$$

Considering torque free motion, thus when T_{tot} can be set to zero in equation 3.4, the Euler equations can be written when considering only the principal moments of Inertia I_{xx},I_{yy},I_{zz} in a principal axis-reference frame as:

$$\frac{dL_x}{dt} = I_{xx}\dot{\omega}_x + \omega_y\omega_z(I_{zz} - I_{yy}) = 0 \tag{3.8a}$$

$$\frac{dL_y}{dt} = I_{yy}\dot{\omega}_y + \omega_x\omega_z(I_{xx} - I_{zz}) = 0 \tag{3.8b}$$

$$\frac{dL_z}{dt} = I_{zz}\dot{\omega}_z + \omega_x\omega_y(I_{yy} - I_{xx}) = 0 \tag{3.8c}$$

3.2. Attitude simulation

In order to simulate the attitude dynamics of a spacecraft, the equations of motion as described in section 3.1 need to be integrated. Solving the differential equations is achieved using a direct integration one-step method. The Runge-Kutta method is chosen as a suitable integrator. First the methods of this integrator will be explained after which the integrator will be tested.

3.2.1. Runge-Kutta method

The fourth order Runge-Kutta family (RK4) is the most used version of the R-stage integrator family as it results in the maximum order(and minimum truncation error) for a given R Wertz (2012).

If **y** represents an unknown function at a certain time t_n where n represents the nth step from the initial step at time t_0, where each nth step follows after a fixed step size **h** then:

$$y_{n+1} = y_n + \frac{h}{6}(k_1 + 2k_2 + 2k_3 + k_4) \tag{3.9}$$

and

$$t_{n+1} = t_n + h \tag{3.10}$$

The vectors k_i represent time derivatives at the nth point and are given by

$$k_1 = f(t_n, y_n) \tag{3.11a}$$

$$k_2 = f(t_n + \frac{h}{2}, y_n + \frac{h}{2}k_1) \tag{3.11b}$$

$$k_3 = f(t_n + \frac{h}{2}, y_n + \frac{h}{2}k_2) \tag{3.11c}$$

$$k_4 = f(t_n + h, y_n + hk_3) \tag{3.11d}$$

Where f(t,y) represents the derivative of the unknown function **y**.

Quaternion normalisation From time to time the quaternions should be normalized to satisfy the unit length constraint of the quaternions as given in equation 3.2 . After each integration step the normalization of the new quaternion vector is performed. The difference between a normalized set of quaternions(after each integration set) and a set which does not normalize the quaternions over time in the RK4 propagator has been evaluated for two different time scales. After an hour of propagation, the error is well within 10^{-9} [-] limits as can be seen in figure 3.1. The situation significantly changes after 10 hours of propagation forwards in time as can be seen in figure 3.2, where differences of up to 10^{-2} are found with a constant step size of one second.

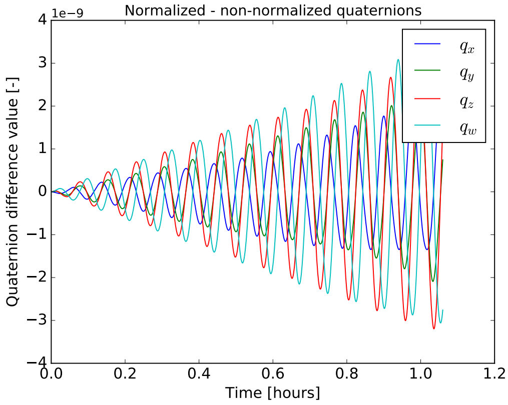

Figure 3.1: One hour quaternion difference

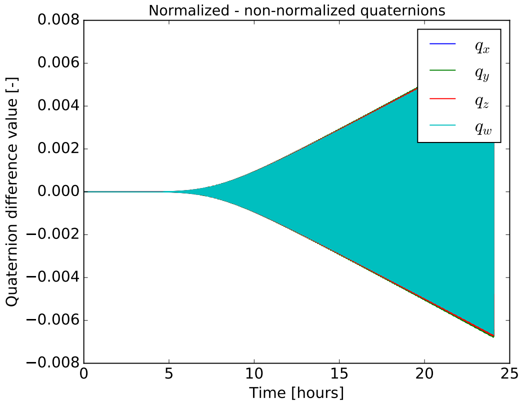

Figure 3.2: 24 hour quaternion difference

Simulator state vector The attitude of a certain torque-free rigid body can be described by using the four quaternion parameters describing the orientation of a body with respect to a specific frame. The three angular velocity parameters describe the rotational motion of the body within this same frame. Both are necessary inputs for the simulator in order to propagate a certain state to the other. The simulator state vector of a rotating rigid body is thus expressed using seven parameters which combine into:

$$\vec{X}_{sim} = \begin{bmatrix} \vec{q} \\ \vec{\omega} \end{bmatrix} \tag{3.12}$$

Next, the derivative of this state vector must be known. From Wertz (2012) the kinematic equations of motion follow:

$$\frac{d\vec{q}}{dt} = \frac{1}{2}\Omega\vec{q} \tag{3.13}$$

Where Ω is the skew symmetric matrix given by

$$\Omega = \begin{bmatrix} 0 & \omega_3 & -\omega_2 & \omega_1 \\ -\omega_3 & 0 & \omega_1 & \omega_2 \\ \omega_2 & -\omega_1 & 0 & \omega_3 \\ -\omega_1 & -\omega_2 & -\omega_3 & 0 \end{bmatrix} \tag{3.14}$$

and the derivative of the rotational velocity which represents the dynamic equations of motion follow from equations 3.8 and are given in 3.15 when considering only the principal axes.

$$\frac{d\omega_x}{dt} = -\frac{(I_{zz} - I_{yy})}{I_{xx}}\omega_y\omega_z \tag{3.15a}$$

$$\frac{d\omega_y}{dt} = -\frac{(I_{xx} - I_{zz})}{I_{yy}}\omega_x\omega_z \tag{3.15b}$$

$$\frac{d\omega_z}{dt} = -\frac{(I_{yy} - I_{xx})}{I_{zz}}\omega_x\omega_y \tag{3.15c}$$

Which follows from equation 3.7 and can be re-written as:

$$\dot{\omega} = I^{-1}(-\omega \times I\omega) \tag{3.16}$$

3.2.2. Spin axis location

A given spin axis location at a certain moment in time can be translated to a three dimensional rotational velocity vector which is required by the integrator.

If the local orbit frame(l-frame) is selected as a frame in which the body-frame(b-frame) rotates, the spin axis can be defined as follows. As a starting point a set of two spherical angles and a velocity magnitude define an initial rotation axis location in the l-frame. The angles can be represented by an Azimuth (Az) angle and an Elevation (El) angle, which together with a corresponding vector magnitude($|\omega_\text{i}|$) form the three-dimensional vector itself which is illustrated in a spherical coordinate system representation in figure 3.3.

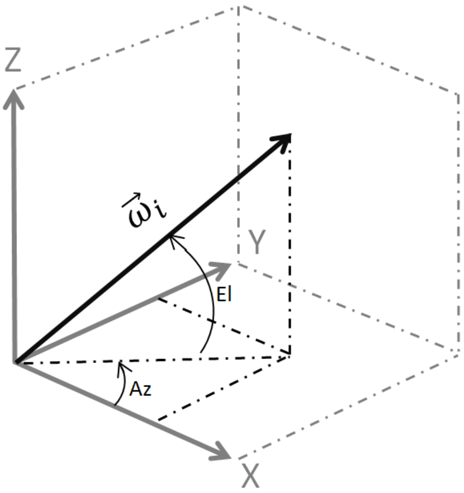

Figure 3.3: Spherical coordinate system with rotational velocity vector(ω_i) in the local orbit l-frame

In order to map the spherical representation to a three-dimensional Cartesian representation of the spin axis($[\omega_\text{i,x}, \omega_\text{i,y}, \omega_\text{i,z}]$) the following relations need to be applied according to the conventions used in figure 3.3.

$$\omega_{i,x} = |\omega_i|\cos(El)\cos(Az) \tag{3.17a}$$

$$\omega_{i,y} = |\omega_i|\cos(El)\sin(Az) \tag{3.17b}$$

$$\omega_{i,z} = |\omega_i|\sin(El) \tag{3.17c}$$

As mentioned in section 3.1.1 the angular velocity vector ω in the dynamic equations of motion(equation 3.4) needs to be used along body-fixed axes in order to be used by the RK4 integrator as the moment of inertia tensor is expressed along this frame. This means the spin-axis location as given in the spherical coordinate system needs to be transformed to Envisat's specific b-frame, such that the rotation of the b-frame with respect to the l-frame is achieved.

If the spherical representation of the angular velocity vector of the spin axis is given in the local l-frame, its corresponding value along the b-frame can be achieved using a Direction Cosine Matrix (DCM) multiplication from a suitable attitude parametrization set(euler/quaternion) as is shown in appendix A.

3.2.3. Step size performance

Selecting a suitable step size which is within a certain threshold of accuracy could increase the CPU speed of the simulator. This is noticeably important when one needs to propagate the attitude till the next station pass, which can reach values from 3 up to 13 orbits or 300 to 1300 minutes respectively as will be shown in section 4.6.3. As a first test case, a two hour propagation time has been selected. The error of different step sizes over time is expressed relative to a one second step size in figure 3.4. It resembles the norm of the differences of the LRR-COM position vector at every epoch relative to the one second step size version. As initial condition a rotational period of 125 seconds is chosen. When considering only a single pass of a couple of minutes(figure 3.5, the errors show small osculations and again a 5 second step size shows to have a significant lower error with respect to the 15 and 20 sec case. This is expected due to the relative rotational period of 120 sec.

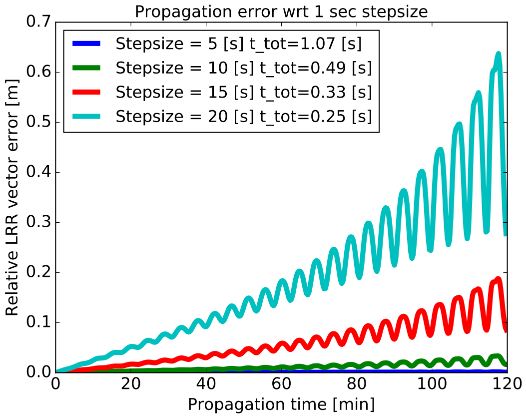

Figure 3.4: Steps size choice for a long term propagation

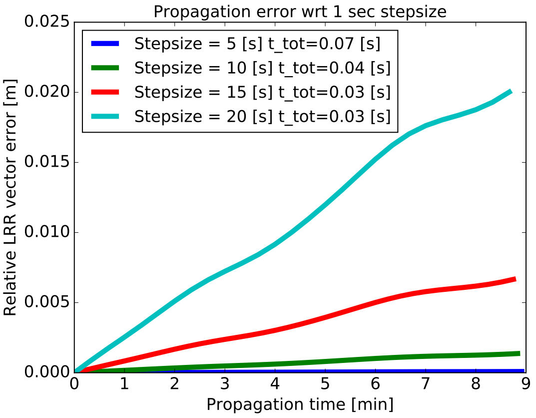

Figure 3.5: Steps size choice for a single pass

It is clearly visible that the range in which the relative error oscillates, increases non-linear over time. A step size of five seconds is nearly perfect even after an entire orbit of propagation. The oscillations in the errors are due to the fact that the spin axis is not aligned with the principal axis causing slight precession. When this error increases over time the oscillations and thus the precession increases even more. For short arc problems a step size of one second can easily be selected. But when considering longer arcs, a slightly bigger step size is worth consideration in order to reduce computational time. Together with the produced error a suitable choice for a step size for the problem at hand can be made.
Figure 3.4 also shows the computational time required for different step sizes. To put things into perspective, propagating 120 minutes of quaternions with a one second time step takes about five seconds of computational time. The computational speed is directly proportional to the step size. So doubling the step size would result in a decrease of the computational time by 50%. Off course the error is also dependent on the rotational speed. A faster rotation would need corresponding faster evaluations. When longer periods of several hours need to be propagated, the errors become larger and larger and the integrator becomes unstable after a certain number of iterations as can be seen in figure 3.6. After about 3 to 5 hours the integrator diverts to significantly larger values. The reason why a maximum limit of 4 m of error is kept is due to the maximum offset of 2 m between the COM and the LRR(see table 2.4. If both runs point in exactly the opposite direction the error becomes twice the size of this offset.

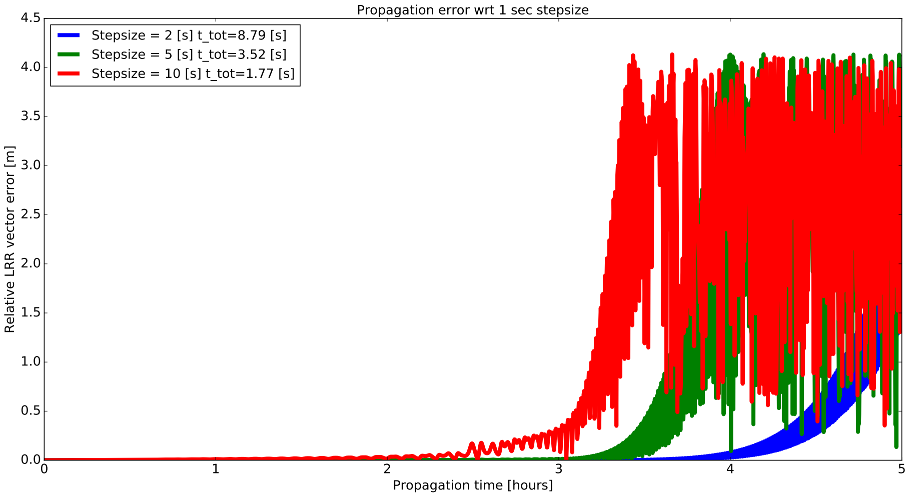

Figure 3.6: Long propagation time

This clearly shows that for long term propagation the stability of the RK4 integrator is highly dependant on the step size. Decreasing the step size underneath rapidly rises the propagation time to about 30 seconds and higher.
If however only the principal moments of inertia are taken into account and the spin axis is aligned with it in a torque free environment, the performance of the step size changes significantly. The rotation becomes a lot more simple as it rotates with a constant rate around a principal axis. The result is illustrated in figure 3.7.

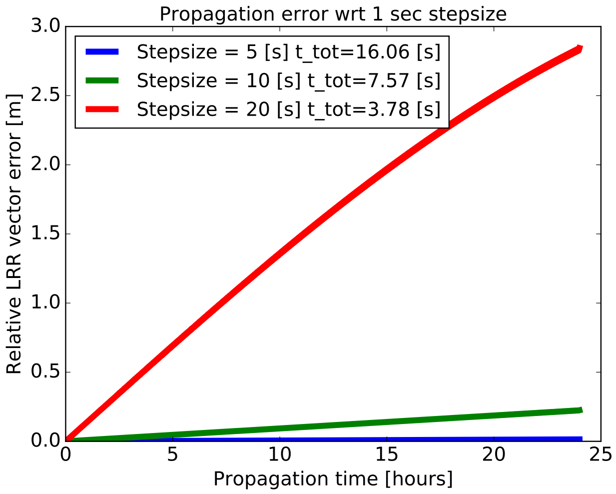

Figure 3.7: Long term orbit propagation LRR error with spin axis aligned with principal moments of inertia

The induced wobble as seen in figure 3.4 clearly disappears and smaller errors over time are visible. This shows that for long-term propagation a one second step size using the principal axes only results in a highly accurate propagation. This is however only valid when assuming a torque free environment and a spin axis which is aligned with one of the principal axes. For more complicated attitude situations, a step size smaller than one second must be selected for propagation times longer than three hours.

3.3. Validation of attitude model

This section will show the results of the validation of the attitude model. A simple torque-free rigid body case will be assessed as an example to validate the model with the work of Tewari (2007). As an input, a rigid spacecraft is chosen with initial parameters as given in table 3.1

Table 3.1: Tewari validation example

Moments of Inertia [kgm^2]			Initial angular velocity [rad/s]			Initial attitude [rad]		
I_{xx}	I_{yy}	I_{zz}	$\omega_x(0)$	$\omega_y(0)$	$\omega_z(0)$	$\psi(0)$	$\theta(0)$	$\phi(0)$
4000	7500	8500	0.1	-0.2	0.5	0	$\pi/2$	0

Tewari (2007) uses a build-in function in MATLAB(ode45.m) which uses a fourth-order Runge-Kutta algorithm as well, where the nonlinear, torque free Euler and kinematic equations are solved. A 3-1-3(Z-X-Z) Euler transformation sequence is used together with a time step of one second. The angular velocities in the spacecraft body-centred frame as well as the corresponding euler angles are are given in figures 3.9 & 3.11 where 40 seconds of data have been simulated. The same input variables as well as the 3-1-3 transformation sequence are used in the simulation model and its results are compared to Tewari's plots as given in figures 3.8 & 3.9.

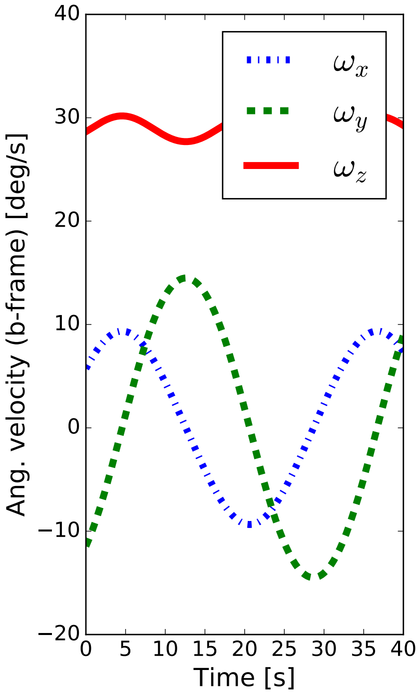

Figure 3.8: Model example ω

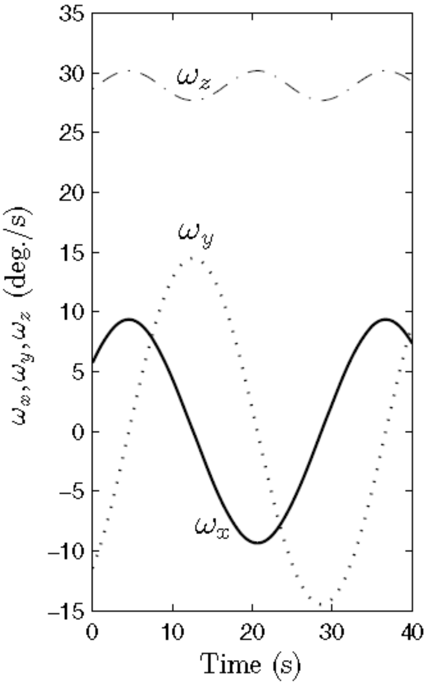

Figure 3.9: Tewari (2007) example ω

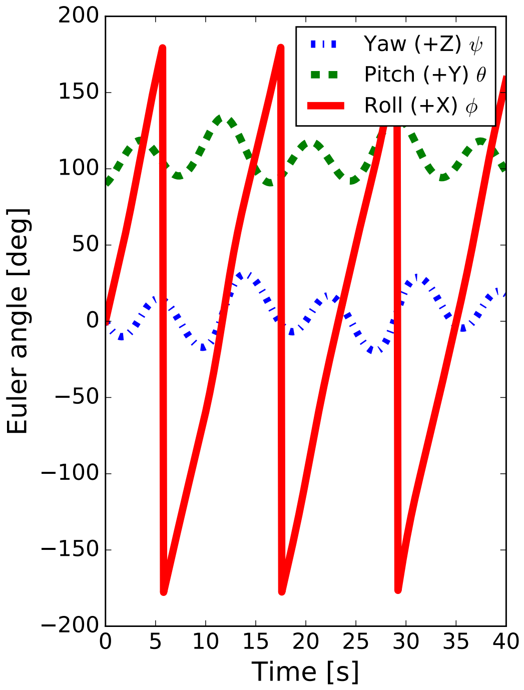

Figure 3.10: Model example euler angles

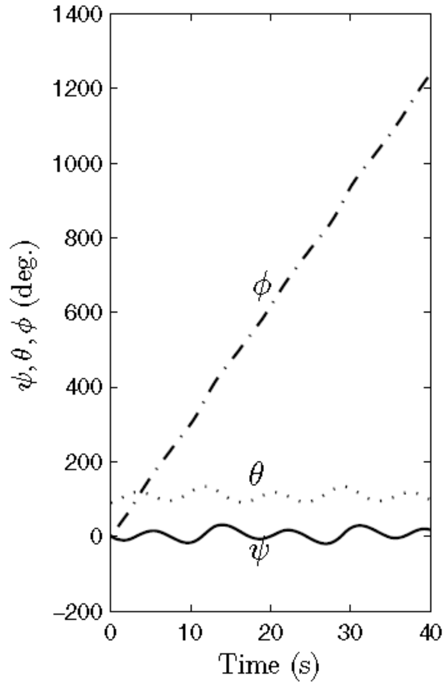

Figure 3.11: Tewari (2007) example Euler angles

The precession in ω_x,ω_y,ψ,ϕ is clearly visible in both cases. The osculation of ω_z, as defined as the nutation, is visible as well in both cases.

The work of Terze et al. (2016) also provides another validation example of a rigid body RK4 integrator. Table 3.2 shows the input elements used. A fixed step-size of 10^{-3} sec has been selected. Terze does however use an additional torque in its rotational equations, which results in a slight increasing offset between both models which can be noticed between figures 3.14 and 3.15.

Table 3.2: Terze validation example

Moments of Inertia [kgm^2]			Initial angular velocity[rad/s]			Initial quaternion [-]			
I_{xx}	I_{yy}	I_{zz}	$\omega_x(0)$	$\omega_y(0)$	$\omega_z(0)$	q_1	q_2	q_3	q_4
0.234375	0.46875	0.234375	0	150	-4.61538	1	0	0	0

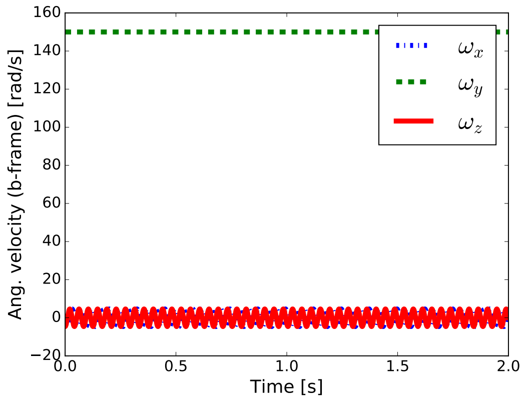

Figure 3.12: Model example angular velocities

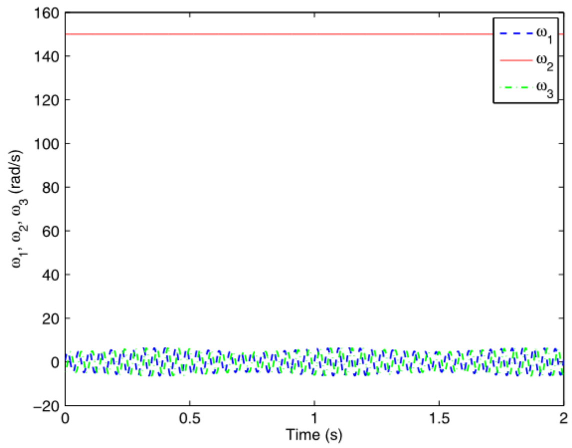

Figure 3.13: Terze et al. (2016) example angular velocities

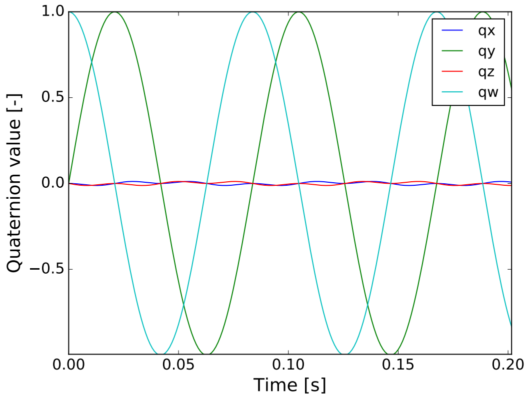

Figure 3.14: Model example quaternions

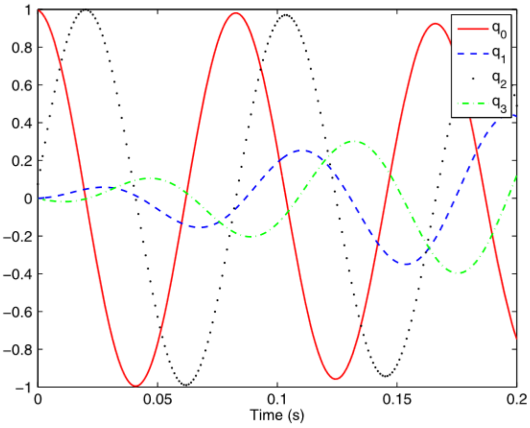

Figure 3.15: Terze et al. (2016) example quaternions

Again both the angular velocity as the attitude parametrization show good resemblance of the produced RK4 model and found example results from literature.

3.4. Attitude simulation: a test case

This section shows the outcomes of the RK4 integrator as described in the previous section with a direct implantation on Envisat data . Kucharski et al. (2014) already analysed Envisat's spin axis location with the help of SLR. By fitting a reflection cone of the LRR together with the observation laser vectors, the spin axis location was found to lie in a so-called Radial Coordinate System (RCS) at corresponding angles: Longitude (Lon)= 269.22° and Latitude (Lat)=28.14° as can be seen in figure 3.16. Here an important assumption was made that the found spin axis location should be parallel to the symmetry axis of the LRR. This implies that the spin axis should lie in the body-fixed Z_b axis direction. Schildknecht et al. (2015) already showed that this assumption might not be true as will be further analysed in chapter 5. For this small example, the found orientation of Kucharski will be used.

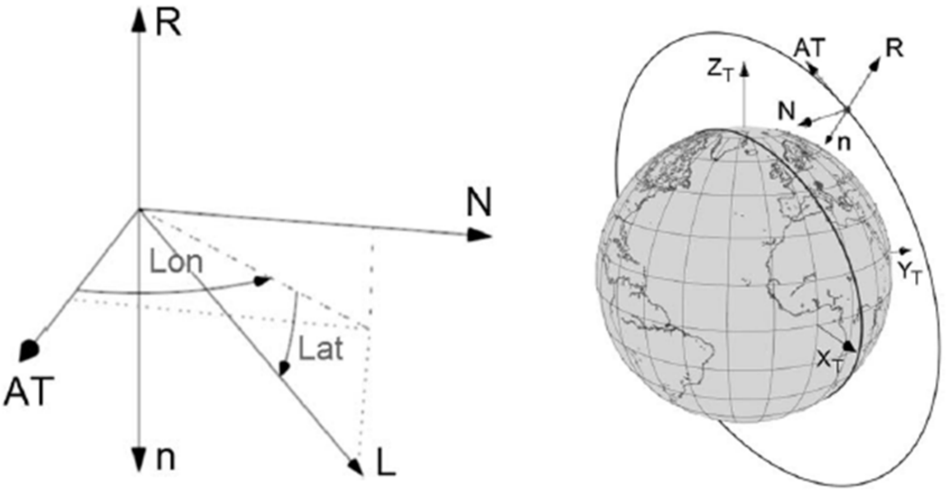

Figure 3.16: RCS system as defined by Kucharski et al. (2014)

The RCS system is centred in the COM and composed of a Along-track (AT), Normal (N) and Radial (R) vector which is the direct opposite to the Nadir (n) vector pointing towards the center of the Earth. The RCS system can thus be regarded as the previous defined l-frame where the along-track vector corresponds with the $+X_l$-direction, the normal vector with the $+Y_l$-direction and the radial vector with the $+Z_l$ direction. Here the radial axis is chosen as the principal axis where in the l-frame the velocity vector which lies along track is chosen as the principal axis. Envisat's orbit is slightly non-circular which would imply that the along-track axis is not necessary parallel to the velocity vector. The eccentricity of Envisat's orbit is however that low that this approximation would not result in major differences. The latitude and longitude orientation angles from Kucharski furthermore correspond with the previous azimuth and elevation angles respectively as defined in the spherical coordinate system in figure 3.3. Kucharski shows a positive latitude angle in figure 3.16 defined as negative with respect to the spherical coordinate system in figure 3.3. This is only to make clear that the spin axis(L) is pointed in the nadir direction.

Table 3.3 summarizes the first set-up input parameters of the rotational model. As a reference epoch, the first of January 2014 has been selected. This date corresponds(according to Kucharski) to an inertial spin period of about 138 seconds or an angular velocity of 2.6 deg/sec(0.045 rad/sec).
As a last input the initial attitude must be specified. Kucharski makes the assumption that the orientation of Envisat's spin axis remains stable and is parallel to the the orientation of the LRR. The LRR is mounted on the bottom side of Envisat and points towards the $-Z_b$ direction in the b-frame. In order to comply with this assumption the original b-frame must be rotated in order to align with the spin axis. Kucharski assumes the RCS frame coincides with the nominal flight mode orientation.

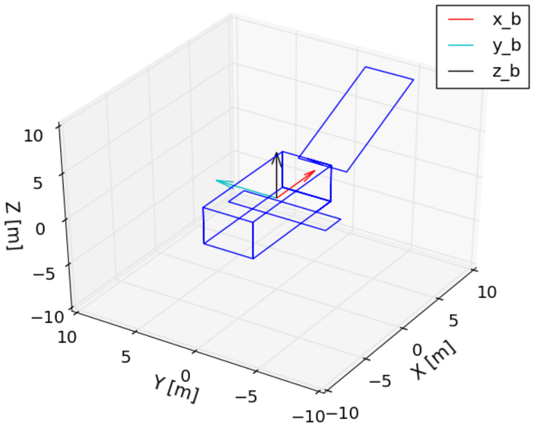

Figure 3.17: Envisat b-frame in l-frame

In order to align the initial attitude with the spin axis as proposed by Kucharski the following transformations are executed. Using a "ZYX" transformation, the corresponding rotation angles(ψ_0,θ_0,ϕ_0) given in table 3.3 need to be used in that particular order which aligns the Envisat's b-frame Z_b axis with the angular velocity vector in the l-frame. Figure 3.17 shows a sketch of Envisat in its original position in the l-frame where no transformation have been carried out. The body axes of Envisat's b-frame thus correspond to the local orbit axes(l-frame).

Table 3.3: Attitude setup 1, based on Kucharski et al. (2014)

	Az [°]	El [°]	P_0 [s]	ψ_0 [°]	θ_0 [°]	ϕ_0 [°]
Value	269.22	-28.14	138	179.22	0	61.86

The results of this transformation can be seen in figure 3.18 where a simple panel model of Envisat is included to illustrate the orientation and axis conventions. Note that the panel model, consisting of the main bus, solar panel and ASAR, is only a sketch and does not resemble the exact satellite in great detail. The solar panel is shown in its anti-canonical position.

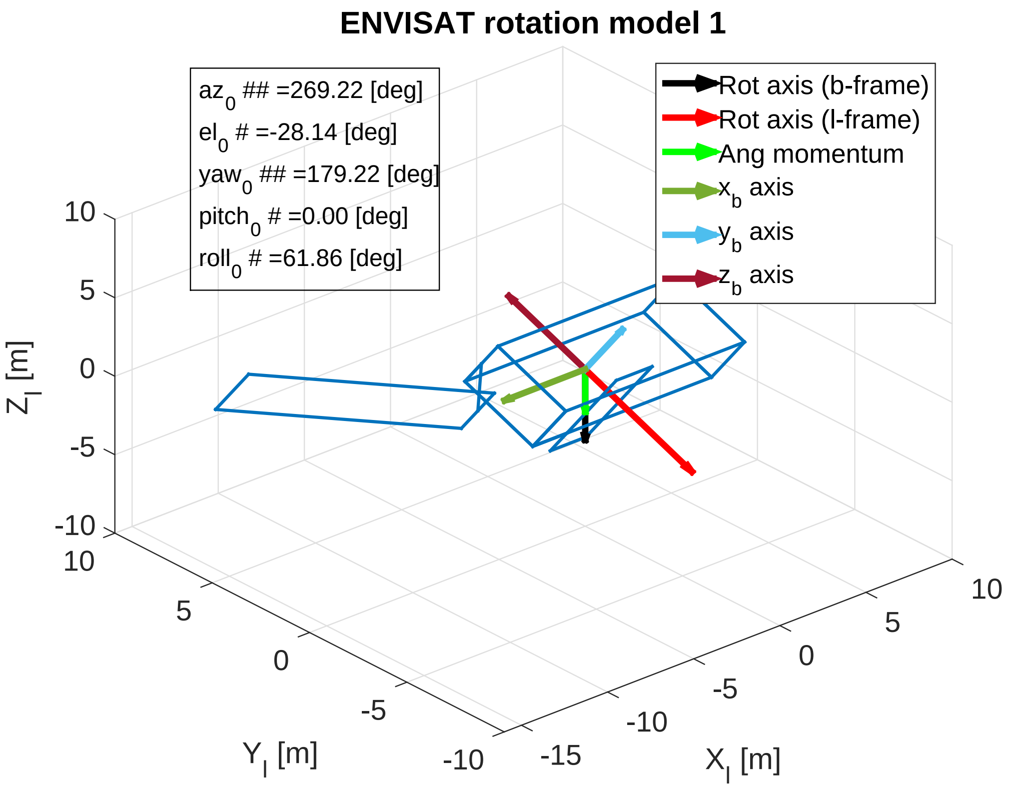

Figure 3.18: Initial attitude and spin axis based on Kucharski

Figure 3.19 shows the rotational velocities between the b-frame and the l-frame expressed in the b-frame of Envisat. Figure 3.20 show the corresponding euler angles using the "ZYX" transformation sequence.

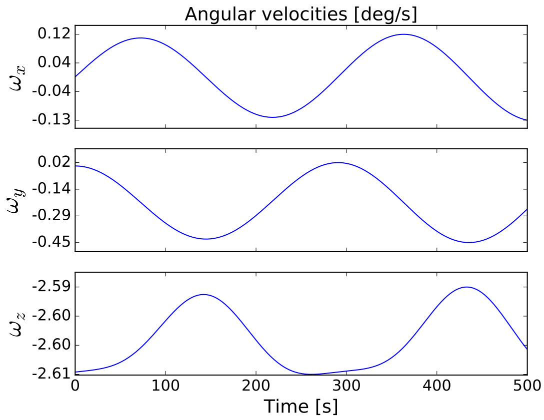

Figure 3.19: Angular velocity in b-frame

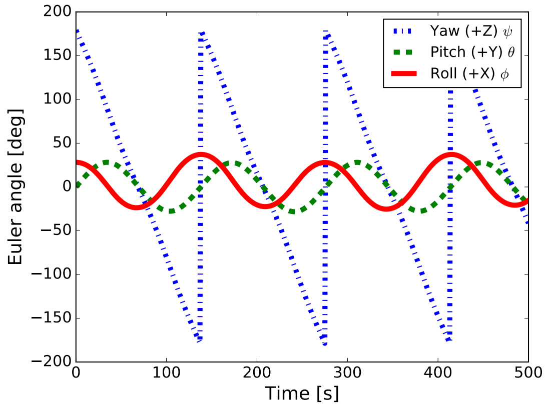

Figure 3.20: Euler angles (ZYX)

The position of the LRR within the l-frame is plotted over time which is shown figure 3.21, 3.22 and 3.23 for various different settings.

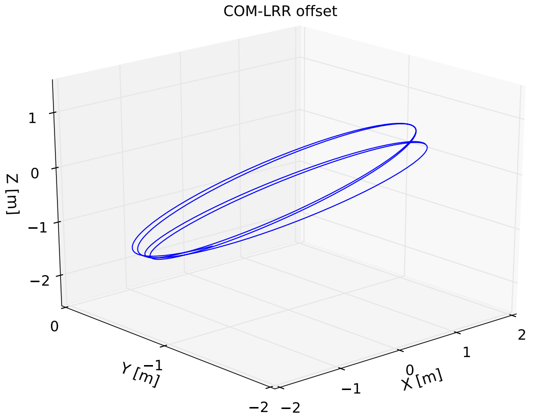

Figure 3.21: 500 sec simulation full inertia

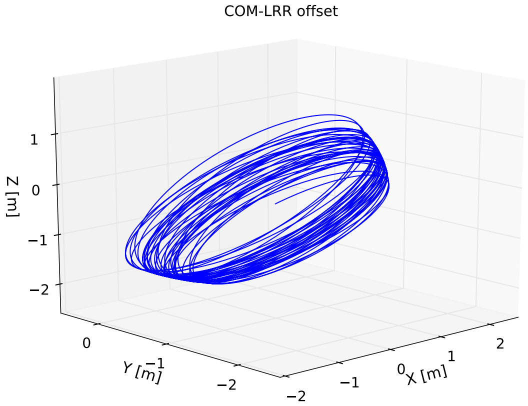

Figure 3.22: 5000 sec simulation full inertia

A clear offset from each revolution over time can be seen which evolves over time when the simulation time is increased from 500 to 5000 sec. This is due too the the use of the full Inertia matrix where non-principal Inertia elements (Ixy etc) are also taken into account. The initial spin axis is aligned with the body's Z_b-axis, however this is clearly not the true principal axis. This results in conical motion or wobbling also known as precession. It is a known effect when the satellite spins around a principle axis of inertia which is not aligned with the axis of symmetry. The effect is clearly illustrated when only taking the principal moments of Inertia(Ixx,Iyy,Izz) and aligning it with the spin axis which results in a perfect circular behaviour of the LRR point as can be seen in figure 3.23. This is a purely theoretical case when no external or internal torques or forces are acting on the spacecraft.

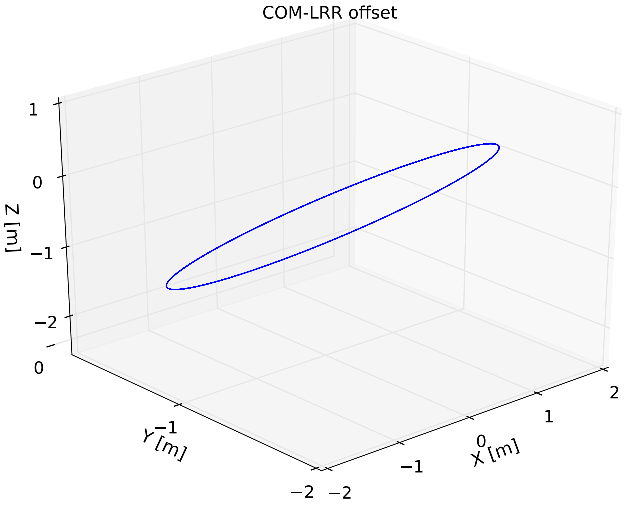

Figure 3.23: 500 sec simulation principal axis aligned with spin axis

3.5. Conclusions

The torque-free rigid body attitude simulator has been build which takes seven parameters as variable inputs. These include the initial rotational axis in the l-frame which are defined using the spherical representation(AZ,El,w_0). Secondly, there is the initial attitude of the body which is represented using the quaternion parametrization([q1,q2,q3,q3]).

The use of the model has been validated with two simple rigid body examples assuming torque free motion. If long-term propagation is needed(longer than three hours), small step sizes(<1 sec) in the integrator are required. Furthermore, the conical motion of the LRR in the l-frame has been demonstrated based on the spin axis assumptions made by Kucharski. It is clearly visible that this motion shows to divert from a stable condition when the spin axis is not aligned with one of the principal axes.

4

Orbit determination

> *"Look up at the stars and not down at your feet. Try to make sense of what you see, and wonder about what makes the universe exist. Be curious. "*
> — *Stephen Hawking* , English theoretical physicist

In Envisat's current passive state, the active DORIS and S-band tracking systems are not available any more which leaves only the passive SLR system to be used for accurately tracking and orbit determination of Envisat. Radar based methods are not considered for this thesis work. This chapter will briefly start with a small introduction about the orbit determination software GEODYN in section 4.1. Here, the new SLR data format and its implementation in GEODYN will be addressed. Next, in section 4.2, the orbit determination options and specific models will be shown. Next, in section 4.3, the use of an external attitude model is validated in GEODYN using an induced external attitude model during the active period of Envisat. Section 4.4 will then show the force model parameters after which in section 4.5 the orbit propagation errors are given based on the simple cannonball model. Section 4.6 will cover all relevant station pass statistics such as availability, pass length and quality. From the produced range residuals, the apparent spin period will be extracted and an analyse of the visibility of Envisat during its passes over ground stations will be given in section 4.7.

4.1. GEODYN

Geodyn II is a orbit determination program written by EG&G Washington Analytical Services Center Inc for NASA's Goddard Space Flight Center, which has been operational since November 1985 (McCarthy et al., 1972). GEODYN is not only used for orbit determination solutions but also for all kinds of satellite geodesy analysis using a large variety of tracking data. For this thesis, the 2007 edition has been used which runs a 32-bit version. The program uses three main steps indicated as the Tracking Data Formatter (TDF), the GEODYN II Setup (GIIS) and the Geodyn II Execute (GIIE) step. The "II" indicates the second series of the GEODYN package. The TDF step of GEODYN converts the given input data to a usable blocked GEODYN II binary format. GEODYN can not read the standard CRD SLR format into its TDF step. This conversion from CRD to a suitable GEODYN binary format has been developed by Bart Root in his MSc Thesis (Root, 2012) as will be given in section 4.1.1.
After successful insertion of the input data, the GIIS step is executed. Here GEODYN reads and interprets all user-defined input options and models which will be given in section 4.2. The IIS step thus prepares GEODYN based before the IIE step can be run. The actual orbit determination(or parameter estimation) process and all necessary calculations will be executed in the last and final GIIE step.

This step uses a Bayesian least squares statistical estimation procedure for parameter estimation. As more observations than parameters are available, the parameters are said to be overdetermined which requires a statistical estimation scheme which estimates the best combination of parameters which match these observations. The relation between the made observations and the orbital parameters are considered non-linear

such that an iterative procedure is necessary which solves the resultant non-linear normal equations. In order to solve these, GEODYN uses a standard Newton-Raphson iteration procedure.
If a vector of n independent observations is defined as $\vec{b}$ which can be expressed using a known function f of m parameters defined as the vector $\vec{x}$, the following relation holds:

$$\vec{b} = f(\vec{x}) + \epsilon \tag{4.1}$$

where ϵ is an n-sized vector including noise of the measurements. For a given set of measurements $\vec{b}$, the function f and a certain amount of statistical information of the measurements (ϵ), a certain set of parameters $\vec{x}$ exists which match equation 4.1 as close as possible. The Bayesian method tries to find this set of parameters by maximizing the probability density function often referred to as a maximum likelihood problem. For a full explanation of this estimation method the reader is referred to Tapley et al. (2004) and Montenbruck and Gill (2001).

4.1.1. SLR data format

The International Laser Ranging Service (ILRS) is the main global provider and distributor of satellite and lunar laser ranging data. Previous data formats which the ILRS used consisted of three different types. A full-rate, normal point or quick look type. The full rate type was composed of all the raw information possible. The normal point data type is a more manageable type due to the combination of several measurements into one single data point. A common normal point is a combination of 15 seconds of data. The (engineering) quick look data served as a way to gather the necessary information of the station during a certain pass. In 2007, the ILRS released a new SLR format, called the Consolidated Laser Ranging Data Format (CRD). Ricklefs and Moore (2009) mention that the recent technology changes(like the increased use of kilohertz firing rate lasers (e.g. Graz (Kucharski et al., 2014)) are the key driver for the use of new format. This resulted in the re-evaluation of the existing three data types: full rate, sampled engineering and normal point. The main purpose of this new format would be to provide a flexible, extensible format for all three types. Next to the ability to handle the new high-repetition-rate data, the added feature of transponder data was a key motivation as well to change the format. Table 4.1 shows the key advantages of the new CRD format.

Table 4.1: CRD format advantages (Ricklefs and Moore, 2009)

Item	Advantage
Flexibility	Simple and compact for kiloHertz ranging
Structure	Including and emitting particular record types as needed by a certain station
Configuration	Adressed in a more explicit, logical and extensible manner
Use	Single integrated format usable for current and future data
Including	Multiple data, modes and configurations as well as multiple types can be included within a single file
Future	Expansion and upgrades are easily implemented
Extensibility	Ability to extend to eXtensible Markup Language (XML)
Compatibility	Configuration sections are compatible with the SLR engineering data file format

The CRD format of a particular pass consists of three main parts. First a header section is provided which provides data like station, target and time information. Secondly, configuration data of the laser system is addressed and last the actual laser transmit and receive times are given together with other dynamic information (Pearlman et al., 2002). An example of the CRD format can be seen in figure 4.1.

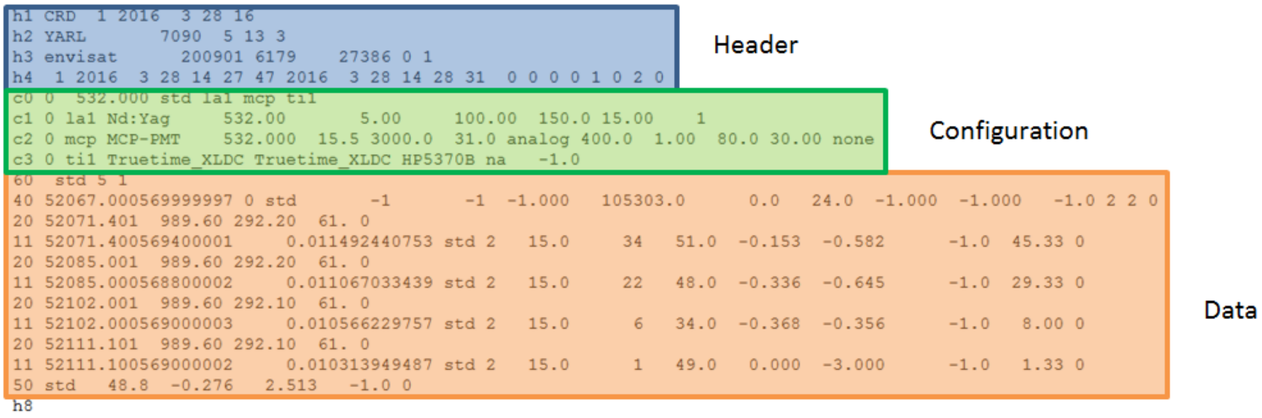

```
h1 CRD  1 2016  3 28 16
h2 YARL        7090  5 13 3
h3 envisat       200901 6179    27386 0 1
h4  1 2016  3 28 14 27 47 2016  3 28 14 28 31  0 0 0 0 1 0 2 0
c0 0  532.000 std la1 mcp ti1
c1 0 la1 Nd:Yag      532.00        5.00      100.00  150.0 15.00    1
c2 0 mcp MCP-PMT     532.000  15.5 3000.0  31.0 analog 400.0  1.00  80.0 30.00 none
c3 0 ti1 Truetime_XLDC Truetime_XLDC HP5370B na   -1.0
60  std 5 1
40 52067.000569999997 0 std        -1        -1  -1.000   105303.0      0.0   24.0  -1.000  -1.000   -1.0 2 2 0
20 52071.401  989.60 292.20  61. 0
11 52071.400569400001     0.011492440753 std 2   15.0      34   51.0  -0.153  -0.582      -1.0  45.33 0
20 52085.001  989.60 292.20  61. 0
11 52085.000568800002     0.011067033439 std 2   15.0      22   48.0  -0.336  -0.645      -1.0  29.33 0
20 52102.001  989.60 292.10  61. 0
11 52102.000569000003     0.010566229757 std 2   15.0       6   34.0  -0.368  -0.356      -1.0   8.00 0
20 52111.101  989.60 292.10  61. 0
11 52111.100569000002     0.010313949487 std 2   15.0       1   49.0   0.000  -3.000      -1.0   1.33 0
50 std   48.8  -0.276   2.513   -1.0 0
h8
```

Figure 4.1: CRD format example

The data record type "11" in the first two columns of the data part as seen in figure 4.1, indicates a range record which contains the accepted measurement data formed into a normal point containing the measured time-of-flight in seconds. The time-of-flight is given as the one or two-way flight time depending on the range type indicator. As Envisat is a passive object, it can only be used with one or multiple stations in the two-way ranging mode. Next, data record type "20" contains a set of meteorological data like surface pressure, temperature and relative humidity at the surface. Finally, data record type "10" corresponds to the full rate or sampled engineering(quicklook) format. These contain single-shot measurement data. As can be seen in a data line of figure 4.1, a normal point window length of 15 sec is used in this example of a station pass from Yarragadee (YARL), located in Australia, to Envisat on the 28th of March in 2016. Each pass ends with a "h8" entry.

The full-rate and normal point data can be downloaded via the Crustal Dynamics Data Information System (CDDIS) or the EUROLAS Data Centre (EDC). It is common to have monthly or daily files with all passes gathered in one single file. An entry "h9" indicates the end of the file. All further information relative to all inputs of the CRD format can be found in the technical note "Consolidated Laser Ranging Data Format(CRD)" as published by the ILRS, and written by Ricklefs and Moore (2009).

CRD converter Geodyn II's TDF program accepts nine different input data formats in order to process it to the latter blocked GEODYN binary format. These include the NASA archaic data format (PCE), Geodyn binary Format (GBF), GBF extended for Altimetry, GEOS-C Card Image, Metric, VLBI, Merit II, Merit-X and Doppler 90 Byte. Previous SLR formats where commonly written in the MERIT II format (Pearlman et al., 2002). A converter thus needs to be used in order to read the new CRD format into GEODYN. Root (2012) developed a CRD-GBF converter during his master thesis in 2012 which was used during the conversions of Crysoat-2 SLR data sets. Root extensively tested and validated the converted CRD format in its newly GBF format using SLR data from Cryosat-2.

4.1.2. Center of mass correction

Equations of motion of a body in orbit always refer to the object's center of mass. Orbit determination software mostly takes the SLR CRD ranging data as an input, assuming the distance between the station and the satellite is accurately given by this range. For Envisat however, there exists a relative difference of about two meters between the actual contact point of the laser (LRR) and the actual center of mass as was given in table 2.4. The orbit determination software thus interprets the varying SLR range data as the satellite's orbital center of mass position. The COM-LRR offset is illustrated in figure 4.2. A lot of stations already use a dedicated COM correction software for several satellites like LAGEOS, Etalon and Ajisai, as these geodetic spherical satellites need mm scale accuracy. For spherical bodies this correction is relatively easy, as this results in the effective radius of the sphere. When the (active) attitude mode is known, the offset correction can be implemented in GEODYN, which is done for instance for Envisat, Cryosat and the ERS missions. Correction vectors for non spherical satellites which are rotating uncontrollable, like Envisat, become significantly more complicated and are highly reliant on their specific attitude state at a certain moment in time.

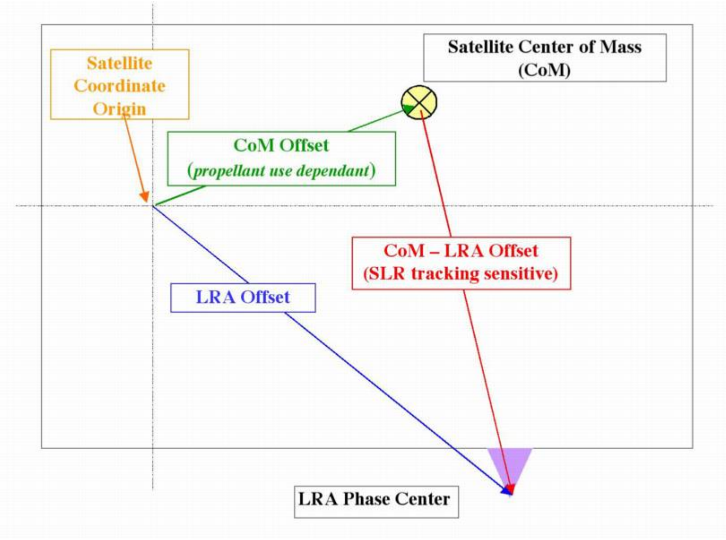

Figure 4.2: Center of mass correction vector (Pearlman et al., 2002)

Whether or not the correction is applied to the SLR data can directly be seen in the CRD file format(see figure 4.1) of the data in the header section, row type "H4", where element 52 indicates the center of mass correction applied indicator(0=not applied, 1= applied). There is no indication that Envisat has this correction applied to its measurements.

4.2. Orbit determination set-up

This section will describe the used models and set-up options in GEODYN. Two main satellite models will be used throughout this thesis. First, with the lack of attitude information, a simple cannonball model will be presented and used. In a later stage, a panel model can be used for both active and passive orbit determination when the precise attitude sate of Envisat is known.

4.2.1. Cannonball model

The most straightforward orbit model which can be used in orbit determination is the so-called cannonball model. In contrast to the more sophisticated macro or panel model as discussed in section 2.3.8, the cannonball model simplifies itself to a spherical geometry with constant and uniform properties. That is, it has a constant mass and constant cross-sectional area. The choice for this model in the first stage of the orbit determination is necessary due to the lack of an appropriate attitude model. Without an attitude model, the COM-LRR corrections as discussed in section 4.1.2, can not be executed. For Envisat, the following cannonball model properties have been selected as shown in table 4.2.

Table 4.2: Cannonball model Envisat properties

	Mass [kg]	Cross-sectional area [m^2]
Value	7827.86	25

The constant cross sectional area of 25 m^2 has been carefully selected after several considerations. First, a study conducted in 2013 by Weigel et al. (2013), showed the orbit determination performance of Envisat past its end-of-life. Weigel et al. (2013) assumes a cross sectional area of 26 m^2 and 20 m^2 for the atmospheric drag and solar radiation pressure coefficient estimations respectively. This model is used for non gravitational force parameter estimation as it assumes constant force on the model at a specific time as well as assuming no torques acting on the body. As mentioned by McMahon and Scheeres (2015), these simplifications are an effective way to represent the average non-gravitational forces if the object is tumbling freely. This results in an equal probability of attitude orientation with respect to the Sun. McMahon and Scheeres (2015) mentions that this approximation is adequate enough for orbit determination of objects that tumble much faster than their orbital rates, especially for low-area-to-mass ratios, which is the case for Envisat.
At first sight this area approximation might seem too low for Envisat's dimensions as was shown in section 4.2.

The effective assumed drag area of 26 m^2 corresponds to the drag area exposed when considering Envisat's orientation as seen in figure 2.11. For comparison reasons, this cross-sectional area is kept the same although in reality it might lie a bit higher. For short term orbit determination, shortcomings of non-gravitational parameters will not be dominating over the meter size residuals and empirical accelerations will absorb non-modelled effects in the orbit determination process, as will be shown in section 4.4.

4.2.2. GEODYN input options

The GIIS step of GEODYN reads all requested inputs from the user as given in a setup file with so-called GEODYN input cards. This section will discuss the chosen models and choices made which will be used for the entire thesis.

As a data arc, a seven day period is selected and is shifted forward each run with one day. In this way seven overlapping residuals and orbits will be created where each run consists of a unique set of SLR data which creates the opportunity to asses the residual and orbit quality based on its given amount of SLR data. This process is illustrated in figure 4.3.

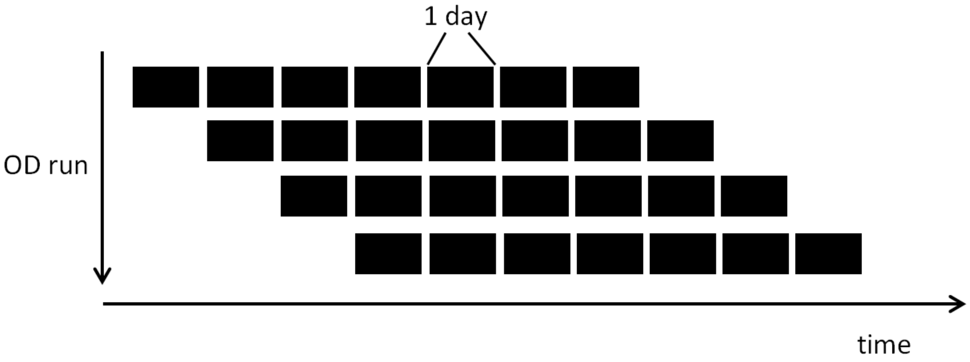

Figure 4.3: Orbit determination sequence method

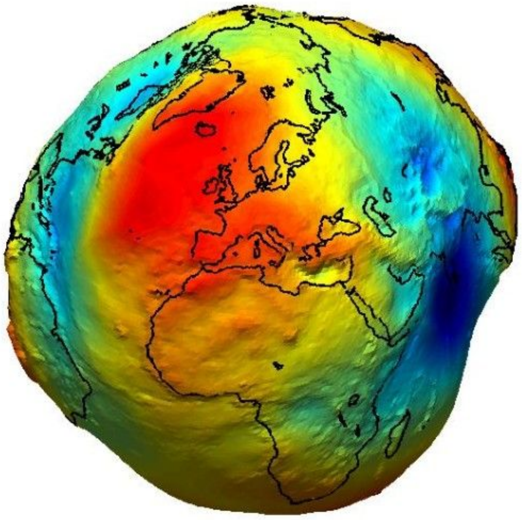

Figure 4.4: Goce gravity model (ESA)

The irregular shape of Earth Gravity model (as seen in figure 4.4) results in a non-uniform gravitational attraction. These relatively large differences result in a slightly perturbed orbit. Using a spherical harmonic coefficient approximation, the Earth's irregular shape is modelled. The second coefficient, often denoted as J_2 is the largest of the geopotential terms as it represents the Earth's oblateness. The effect of the coefficients rapidly decreases after the second coefficient. In each Orbit Determination (OD) run coefficients up to degree and order of 70 are used based on gravity model from the Gravity Field and Steady-Stae Ocean Circulation Explorer (GOCE). The "GOCE03S" model is used which combines Grace and Champ space gravity and SLR observations which improves the standard GOCE03 geoid model (Pail et al., 2011).

The initial orbital elements used by GEODYN to be used in the orbit determination process are taken from TLE data which can be downloaded on *space-track.org*. Although the accuracy of the orbital elements resulting from TLE data is in the order of km's (Bennett et al., 2012), it can be used by GEODYN just like Schrama et al. (2010) demonstrated as the orbital elements lie close enough to the solution for GEODYN to converge to the true solution within a reasonable amount of iterations. Typically about six to seven iteration were found.

Atmospheric corrections, to the laser ranging data, are especially needed when the satellite appears at low elevations below 10° horizon level relative to the station. In this region, range-errors of more than 13 m can occur. Near-zenith situations, increase the average optical path length to about 2.5 m (Abshire and Gardner, 1985). This is quite severe, and needs definitely to be implemented when considering precise orbit determination. Luckily standard models already exist in order to compensate, up to a certain degree, for this refraction. The Marini Murray tropospheric correction model for laser data is used in the proceeding analysis together with a cut-off elevation angle of 10 degrees. This means all measurements below 10° elevation angle relative to the station will be neglected.

The initial drag coefficient of Envisat past its end of life in 2013 is estimated to lie around 4, as was estimated by Weigel et al. (2013). A standard deviation of 1 is selected, which allows deviations due to varying atmospheric conditions as will be shown in section 4.4. Two different surface models are used throughout this thesis. At first, a cannonball model will be used as described in section 4.2.1. Next, when the attitude is combined in the orbit determination process, a 6-face surface/panel model will be used as described in section 2.3.8. These choices influence the coefficient estimation process in GEODYN.

As a static atmospheric density model, the MSIS-86 Empirical drag model is used. GEODYN offers three different atmospheric models: MSIS-86 (Hedin, 1987), Jacchia 1971 (Jacchia, 1970) and a French drag model (DTM-78) (Barlier et al., 1978). Akins et al. (2003) compared the Jacchia and MSIS model by comparing the orbit determination and propagation of 4500 satellites below 1000 km altitude. From this test, the MSIS model showed slightly better results than the Jacchia model. The difference however is found to be that small, that there is no model which stands out to be better according to Akins et al. (2003). According to Sutton (2003), the MSIS-86 model estimates the total density slightly better than the DTM-78 model by comparing measurements from Champ. The MSIS-86 model is therefore chosen as the model to be used throughout the thesis.

The solar radiation coefficient is estimated as well from the work of Weigel et al. (2013) with a value of 2 and a standard deviation of 1. Again first a simple cannonball model will be used, after which the panel model will be used together with its appropriate reflectivity properties as given in tables 2.6 and 2.7 which will provide better estimations of the solar radiation coefficient.

Due to induced tides on the Earth, the Earth's moment of inertia slightly shifts over time. This can be corrected in the OD process using the solid earth tide coefficients of the second and third kind(h_2 and l_2), which are taken from the IERS (Krásná et al., 2013). The ocean and earth tides due to the Sun, Moon and combination of both are taken from the Earth Gravitational Model 1996 (EGM96) model. Finally, a specific ocean load model is added (FES2004) as well for each specific SLR station just like Schrama et al. (2010).

Adjustments of general/empirical accelerations are taken into account on two-day subarcs. Often, daily arcs are used, but due to the limited amount of SLR data and the number of parameters needed to be estimated, the amount of general acceleration parameters has been reduced. The purpose of these accelerations are to absorb not modelled signals in all the models used in the orbit estimation process. Just like the orbit estimation as performed by Schrama et al. (2010) only along track and cross track directions are taken into account for SLR data.

As the along-track and radial components of the l-frame are coupled it is hard to estimate both acceleration directions at the same time. Therefore, the radial component is often disregarded in the estimation procedures. The radial component of the SLR measurement are often the most accurate (Root, 2012). Lageos(figure 4.5) achieves SLR Root Mean Square (RMS) error values of 1 cm in radial direction (Pearlman et al., 2002), and thus makes it (almost) unnecessary to include in the model. For the passive Envisat there exits an offset between the COM and the LRR, thus creating higher RMS values with respect to the orbit, the exact range to the LRR in radial direction remains highly accurate. The em-

Figure 4.5: Lageos (eoPortal Directory)

pirical acceleration is split up in a cosine and sine coefficient which combine to:

$$\ddot{r}_{emp} = C_i \cos(\theta) + S_i \sin\theta \tag{4.2}$$

Where the cosine and sine coefficients are estimated and returned by GEODYN and θ represents the argument of latitude of the satellite in its orbit (Root, 2012). The accelerations will thus vary harmonically with the orbital period.

Each corner cube reflector(section 2.3.5) has its own small offset with respect to the symmetry axis of the LRR itself. Therefore a small additional correction can be applied as well in order to match the exact contact point with the assumed LRR position(symmetry axis) in the Envisat body frame. Usually this is of importance for highly accurate orbit determination, like for instance is the case for Lageos. For Envisat, a constant offset of 5.12 cm is used (Pearlman et al., 2002). When a cannonball model of Envisat is assumed this small cm size correction will not have a large effect on the meter size residuals but is anyhow still included in the cannonball model as the rotational dynamics will be based on the LRR symmetry axis contact point.

Daily magnetic and solar flux tables are required in GEODYN as an input for the atmospheric drag model and solar radiation pressure model. These values are taken from the National Geophysical Data Center (NGDC) which can be download through their ftp servers: *ftp.ngdc.noaa.gov*.

GEODYN posses the option to manual or automatic delete bad measurements. The latter is done after comparing them to a certain rejection level. These ground based measurement errors might occur due to various reasons like for instance using slightly wrong tracking station coordinates, atmospheric effects, instrument modelling, clock accuracy and tectonic plate motion(Tapley et al., 2004). GEODYN does not take into account measurement for which:

$$\left|\frac{O-C}{\sigma}\right| > k \tag{4.3}$$

where O represents the actual observation, C the computed observation, σ the a priori standard deviation association with the observation and k the rejection level which is defined as:

$$k = E_M \cdot E_R \tag{4.4}$$

where E_M is the input multiplier and E_R the weighted RMS of the previous global iteration. An initial value of E_R needs to be specified by the user in the setup file. For Envisat, an observation standard deviation used in forming the normal equations is set at 2m. This is required as the offset between the COM and the LRR can reach values up to 2m. An editing multiplier is chosen at 3.5 which is the default GEODYN option The editing RMS was set at 10^6.

Table 4.3 summarise the entire GEODYN inputs and models used for the orbit determination process.

Table 4.3: GEODYN option input cards summary

Option	Choice	Comments
Earth Gravity Field	70x70	Goce03s gravity model
Initial orbital elements	–	TLE data
Center of Gravity	x:-3.905[m],y:-0.009[m],z:+0.003 [m]	See section 2.3.6
Tropospheric correction model	Marini Murray for laser data	Elevation cut-off angle = 10°
Drag coefficient estimation	4 [-] σ=1	Cannonball model and Panel model
Thermospheric density model	MSIS-86	
Solar radiation coefficient	2 [-] σ=1	Cannonball and panel model
Tidal modelling	h_2 = 0.6090 [-] , l_2 = 0.0852 [-]	IERS, modelling using EGM96
Acceleration coefficient adjustments	0 with σ $1{\cdot}10^{-5}$	Along-track and cross-track only, update every two days
Editing	σ=2 [m], E_M=3.5, E_R=10^6	
Data arc	7 days	-

4.3. Orbit determination pre 2012

During nominal operations, Envisat had a particular attitude motion as described in section 2.3.7. During nominal operations the COM-LRR vector of Envisat was not corrected directly in the CRD normal point SLR data. This would thus have to be completed in the orbit determination process. The OFFSET card of GEODYN, in combination with a suitable internal or external model, provides an easy solution to this problem. The goal of this section is to validate the use of GEODYN in combination with a known attitude model. First the difference between a cannonball model and the use of a attitude correction model will be given, after which a full quaternion set will be derived and implemented in GEODYN using Envisat nominal attitude laws.

4.3.1. Cannonball vs attitude corrections

This section will illustrate the difference between a simple cannonball model vs one with envisat attitude information. Table 4.4 shows the input differences in both models. For this orbit determination run a data set of about 1000 normal points from twelve different SLR stations is used in the seven day arc ranging from the first to the seventh of February in 2012. This region does not contain any known manoeuvres.

Table 4.4: Difference between cannonball and Envisat model input parameters

Option	Cannonball model	Envisat model
SLR σ	2 [m]	2 [cm]
Automatic OFFSET	no	yes
Center of mass correction	no	yes
Surfaces	none	From panel model (sec.2.3.8)
Attitude	none	Envisat nominal law (sec. 2.3.7)
LRR correction	none	5.12 [cm]

A standard deviation of about two meters is assumed in the cannonball model due to the offset between the LRR and the COM which is not corrected as no attitude is available for the cannonball model. The following figures 4.6 and 4.7 show the difference in the residual between both models.

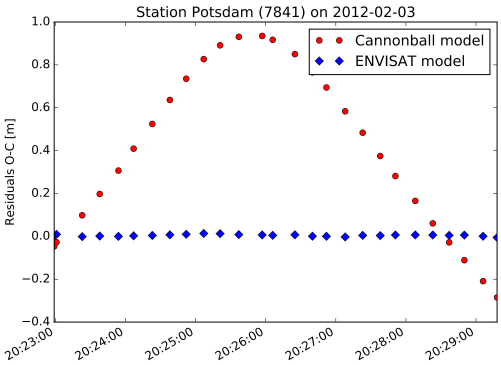

Figure 4.6: Cannonball vs Envisat model example 1

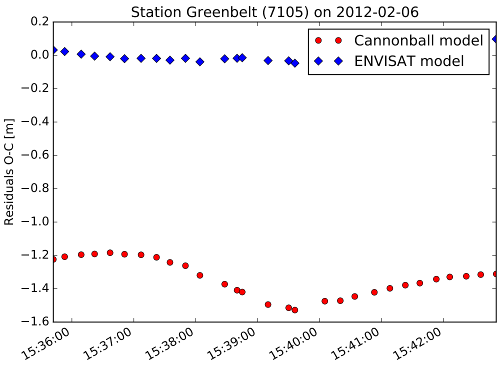

Figure 4.7: Cannonball vs Envisat model example 2

Clearly the Envisat model shows far smaller residuals than the Cannonball model. Figure 4.6 shows an ascending pass over a station whereas figure 4.7 shows a descending pass. For all cases it can be seen that the residuals tend to grow during a pass until a local maximum/minimum. The exact shape of the residuals obviously depends on the pass geometry. Positive and negative residuals could indicate the direction of the SLR vector with respect to the computed orbit. To illustrate this difference, figure 4.8 is created. It shows a sketch of Envisat's XY plane in the b-frame.

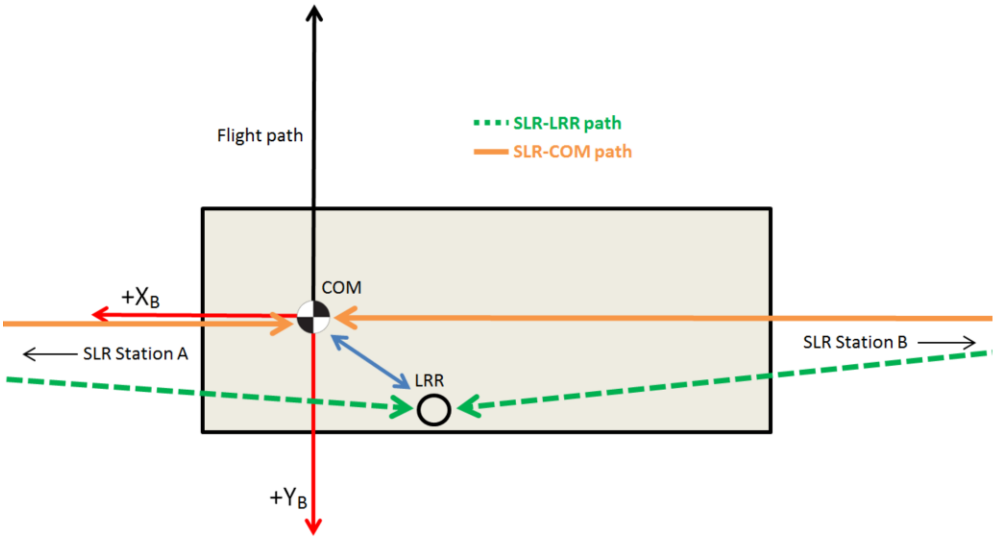

Figure 4.8: Sketch of COM-LRR offsets for 2 different stations in the XY body frame plane, nadir looking

Figure 4.8 illustrates a pure hypothetical case where Envisat is being tracked simultaneously by two SLR stations from both sides, one being in the positive X_b direction, the other in the negative X_b direction. In the case of station A, the range to the LRR will be longer than the calculated range to the COM. This will result in a positive residual as it follows the observed-calculated convention. On the other side, station B will result in a shorter path length than the one directed towards the COM and will therefore result in a negative residual. Generally speaking this would be a valid situation, however in reality this is not the case. The number of stations coming from a specific direction could influence the entire orbit, resulting in an orbit which is slightly pulled towards that specific side. From which direction the SLR stations are in contact with Envisat should be considered when evaluating these residuals.
If the orbit would have a tangential error, the residuals would look a theoretical example from Tapley et al. (2004) in figure 4.9. The figures show the residuals due to an induced orbit error in the radial direction which effects an increasing orbit error in tangential direction over time.

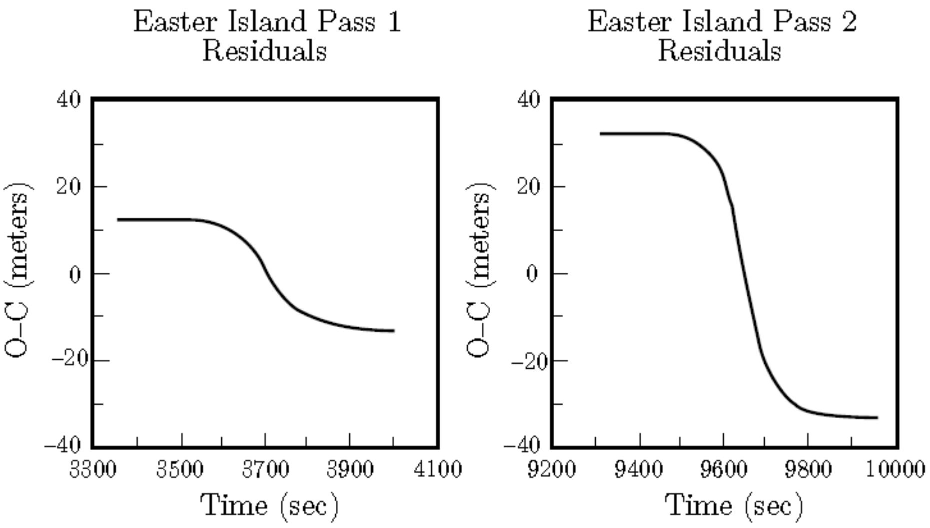

Figure 4.9: Theoretical residuals from a stable attitude state (Tapley et al., 2004)

This shows that a constant offset between the observed and calculated results in these plots which resemble the shape of an inverse range-rate plot. Due to the double effect of a possible orbit error and the constant offset between the LRR and the COM which changes orientation during a pass, a convex/concave residual plot is created just like figures 4.6 and 4.7.

4.3.2. Validating the use of external attitude in GEODYN

By implementing an external attitude file into GEODYN with the exact known conditions as specified by GEODYN's internal model, one can easily investigate and validate the validity of the model in GEODYN. This is achieved using the Envisat internal model which is governed by Envisat's nominal attitude law as described in section 2.3.7. The active attitude motion is dependant on Envisat's orbital position as is given by the true argument of latitude (U_{lat}) in equations 2.6-2.8 which represents the angle between the ascending node of the orbit and the satellites position in the True of Date reference frame and ranges from 0 to 360 degrees. It is often given by the sum of the argument of perigee and true anomaly (Wakker, 2015). The same equations as found in GEODYN are used in order to calculate this orbital parameter. These can be found as well in the work of Montenbruck and Gill (2001) as is given in equations 4.5. The conventions use the actual position([x,y,z]) and velocity([$v_x v_y v_z$]) vector of the satellite in a true of date reference frame, and thus cover the osculating elements of the actual orbit (which is required in the Envisat nominal attitude law).
The argument of latitude is given by

$$U_{lat} = \arctan \frac{z}{-xW_y + yW_x} \tag{4.5}$$

Where the vector **W** equals **h**/h and h defines the angular momentum vector of the satellite at a certain instance given by

$$\mathbf{h} = \mathbf{r} \times \mathbf{v} = \begin{pmatrix} yv_z - zv_y \\ zv_x - xv_z \\ xv_y - yv_x \end{pmatrix} = \begin{pmatrix} h_x \\ h_y \\ h_z \end{pmatrix} \tag{4.6}$$

The elements W_x and W_y follow thus from equation 4.6 and correspond thus to h_x/h and h_y/h respectively where h represents the total angular momentum magnitude.
As a test case the seven day orbital arc as discussed in section 4.3.1 is used. From this calculated orbit, the corresponding orbital positions and velocities in a true of date reference system are used with a time step of 60 seconds. The results for several revolutions starting from the second of February can be seen in figure 4.10.

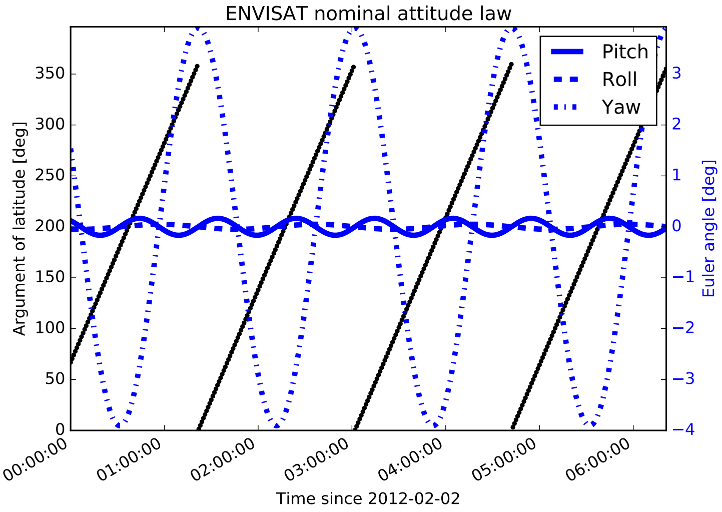

Figure 4.10: Envisat nominal attitude argument of latitude(left) vs euler angles(right)

Clearly, the largest amplitudes are visible in yaw. This mode is often referred to as the Stellar Yaw Steering mode (Alvarez, 1997). Maximum yaw amplitudes are visible around the equator (U_{lat}=180° at descending node or 360° at ascending node). This might be linked to the relative higher sub-satellite-earth velocity. The sinusoidal yaw wobble has its zero yaw angle close to the poles due to the lowest relative earth velocity. The maximum and minimum pitch amplitudes are located between the spacecraft equator and pole passes.

COM-LRR analysis By converting the Euler angles to a direction cosine matrix(transformation matrix) as described in appendix A, the appropriate wobbling COM-LRR offset can be found by multiplying this particular transformation matrix with the original COM-LRR vector.

The relatively large yawing motion clearly affects the COM-LRR offset in the XY plane. Due to this motion, the LRR reflector moves about 12 cm along both sides of its original position in Envisat's XY body frame.

Nominal attitude law to external attitude file The next step involves converting the achieved Euler angles to quaternions, after which an external attitude file is created which can be read by GEODYN. Converting the found Euler angles to the appropriate quaternions with a "ZYX" rotation sequence can be achieved using the transformation rules as shown in appendix A. These quaternions describing the full attitude state of Envisat. Several orbits on the second of February are plotted in figure 4.11.

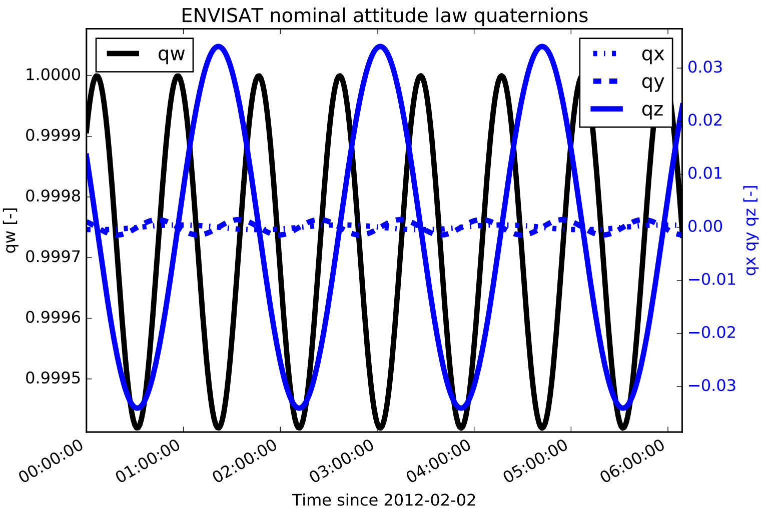

Figure 4.11: Nominal attitude mode quaternions Envisat scalar(left) vs vector(right)

The largest amplitudes are seen in the z direction of the quaternions, indicating the relatively large yaw amplitudes. The scalar part shows higher values as it only involves the cosine of small transformation angles, whereas the vector part takes the sine.
These quaternions can now be put in GEODYN's external attitude file format.

GEODYN external attitude file An external attitude file is created which contains a set of quaternions with interval of 60 seconds. This is regarded sufficient as the nominal yaw steering mode is a relatively slow rotation. It takes an entire orbit to rotate Envisat's Z-axis(yaw) over 7.8° which is equivalent to about 0.0012 °/s. In a minute of time interval between two subsequent quaternions, Envisat has rotated 0.077°. A smaller step size of 15 seconds has been tested and results in an SLR residual difference of about 2-4 mm.

GEODYN requires its time in the so-called Terrestrial Dynamical Time (TDT)(or Terrestrial Time (TT)) rather than in the common used Universal Time Coordinate (UTC). This time scale has been adopted by the International Astronomical Union (IAU) since 1992 and takes into account the difference between the proper time and the coordinate time by applying a constant offset from the International Atomic Time (TAI) at a specific epoch measured on the geoid as given by equation 4.7 (Montenbruck and Gill, 2001). The proper time would be a time measured by an atomic clock co-moving with a satellite, whereas the coordinate time is located at the geocenter. In a general relativistic framework, time is no longer an absolute quantity independent of location and motion.

$$\mathrm{TDT} - \mathrm{TAI} = 32.184\ \mathrm{sec} \tag{4.7}$$

The atomic time scale is based on various cesium atomic clocks around the world. By averaging over these clocks, stochastic variations can be minimized and thus TAI can be used as a pretty good approximation of a uniform time scale (Tapley et al., 2004). This offset is governed by the difference between the Ephemeris time and TAI. UTC is composed of the TAI time and the number of leap seconds. These leap seconds are necessary to maintain synchronization between UTC and Δ(UT1) within ± 0.9 seconds (Tapley et al., 2004). ΔUT1 is a measure of the variation of the Length of Day (LOD)). The variations of the LOD occur due to the changing orientation and magnitude of the earth's angular velocity vector, which are regularly observed by the IERS.

$$\mathrm{TAI} - \mathrm{UTC} = \text{number of leapseconds} \tag{4.8}$$

Table 4.5: Number of leap seconds from 1972 (IERS)

	<2002	1 jan 2006	1 jan 2009	1 jul 2012	1 jul 2015	1 jan 2017
TAI-UTC	32	33	34	35	36	37

For the arc chosen in this section(February 2012) a total correction of (+)66.184 seconds is needed on the UTC to end up at the correct TDT. When applied to the active nominal attitude law this should correspond to a small yaw angle difference of about 0.08°. The following two figures 4.12 and 4.13 show two pass residual examples where the internal and external model is used.

Reference frame Next GEODYN needs the quaternion in a Satellite Body Frame (SBF) to J2000 Earth equator and equinox inertial frame. This means a transformation is needed from the l-frame to the i- frame. Use of the rotation matrices is therefore necessary. The yaw, pitch and roll angles from the nominal attitude law refer to the motion of Envisat with respect to its orbit-fixed frame or the l-frame. This transformation can be re-written to a transformation matrix $\mathrm{R_{LB}}$ which holds the rotation of the body fixed frame (b-frame) in the local l-frame. Next, the satellite's l-frame rotates in the Earth inertial frame. The corresponding transformation matrix can be established using the afore mentioned relations from Tapley et al. (2004) as was given in equations 4.18-4.20.

Due to the fact that the inverse of a rotation matrix is its transpose, the rotation matrix from the local orbit frame to the inertial frame simply follows as

$$R_{IL} = (R_{LI})^{-1} \tag{4.9}$$

Multiplying subsequent rotation matrix with each other result in another rotation matrix which translates to the rotation from the body frame B to the inertial frame I can be written by:

$$R_{IB} = R_{IL} R_{LB} \tag{4.10}$$

Which is the GEODYN required rotation matrix SBF-J2000. The $\mathrm{R_{IB}}$ rotation matrix can be transformed in a corresponding set of quaternions using the transformations specified in appendix A.

Results Two examples are shown in figure 4.12 and 4.13 which clearly show that the internal model matches the produced external attitude model quite well. Small errors between the internal and external model are however still visible. This might be due to rounding errors and interpolation step sizes. Furthermore, a clear difference is visible when only SBF-local frame quaternions are inserted instead of the correct SBF-J2000 Inertial frame.

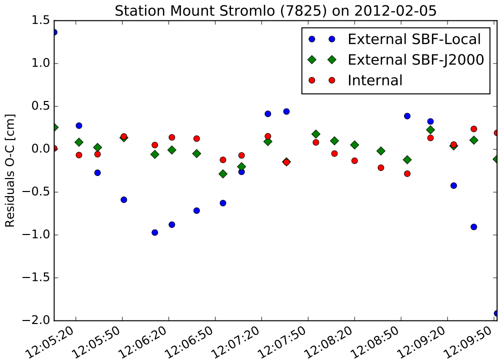

Figure 4.12: External vs Internal model example 1

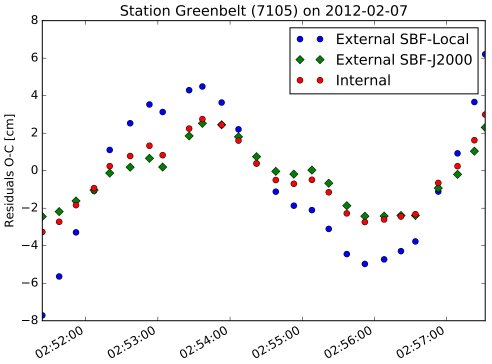

Figure 4.13: External vs Internal model example 2

A similar study has also been performed using Jason-2 data by Lemoine et al. (2009). The results are shown in figure 4.14 where both SLR and DORIS residuals are compared to the internal attitude model of GEODYN. Small differences exist as well in the residuals, which was still for an unknown reason according to Lemoine et al. (2009) and would be further investigated.

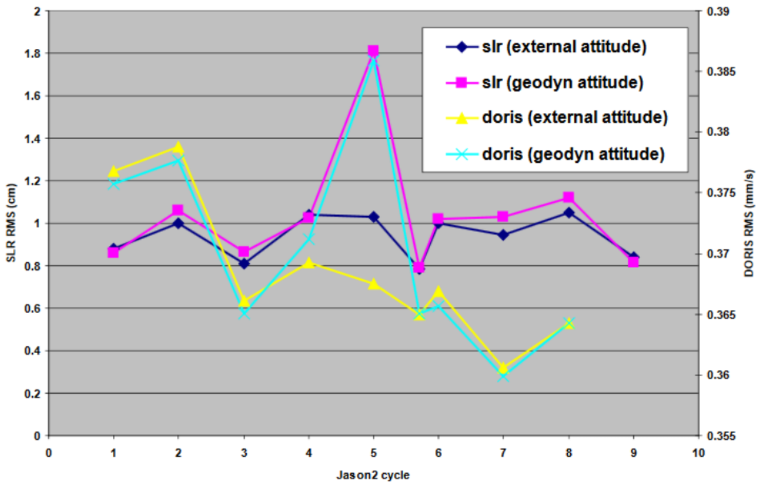

Figure 4.14: Internal vs external attitude use in GEODYN example with Jason-2 data (Lemoine et al., 2009)

.

4.4. Force model parameters

Each orbit determination run, force parameters are estimated to meet the best orbit based on used atmospheric models, shape and orientation of the spacecraft. The two most important parameters to be estimated are the atmospheric drag and solar radiation pressure coefficient. The atmospheric drag estimation procedure relies on the altitude, the frontal area perpendicular to the flight direction and the atmospheric model. The solar radiation pressure coefficient uses the daily F10.7 solar flux indices together with the spacecraft area facing the sun and the reflective properties of the specific sun-facing surface. Weigel et al. (2013) takes an average of 26 m^2 as Envisat's drag area considering a cannonball model approximation. This is about the same area when only Envisat's Z-X plane in the b-frame is considered(see figure 2.11). With this average Weigel estimated force parameters of about 5 and 2 for the drag and solar pressure respectively from may to October 2013. The reflective properties of Envisat as given in the panel model are not considered in the cannonball model as it is assumed that the orientation is unknown. The larger the estimated empirical accelerations, the larger the corrections applied. The cosine and sine coefficients which define the direction of the empirical acceleration can be transformed into corresponding amplitudes and phase angles using the following trigonometric rules:

$$\ddot{r}_{emp} = C_i \cos(\theta) + S_i \sin(\theta) = A \sin(\theta + \Phi) \tag{4.11}$$

Where A and Φ represent the amplitude and phase shift of the particular empirical acceleration direction. These quantities can be calculated using the norm of both cosine and sine coefficients and the arc tan of the cosine over the sine coefficients respectively. The results are given in figure 4.15.

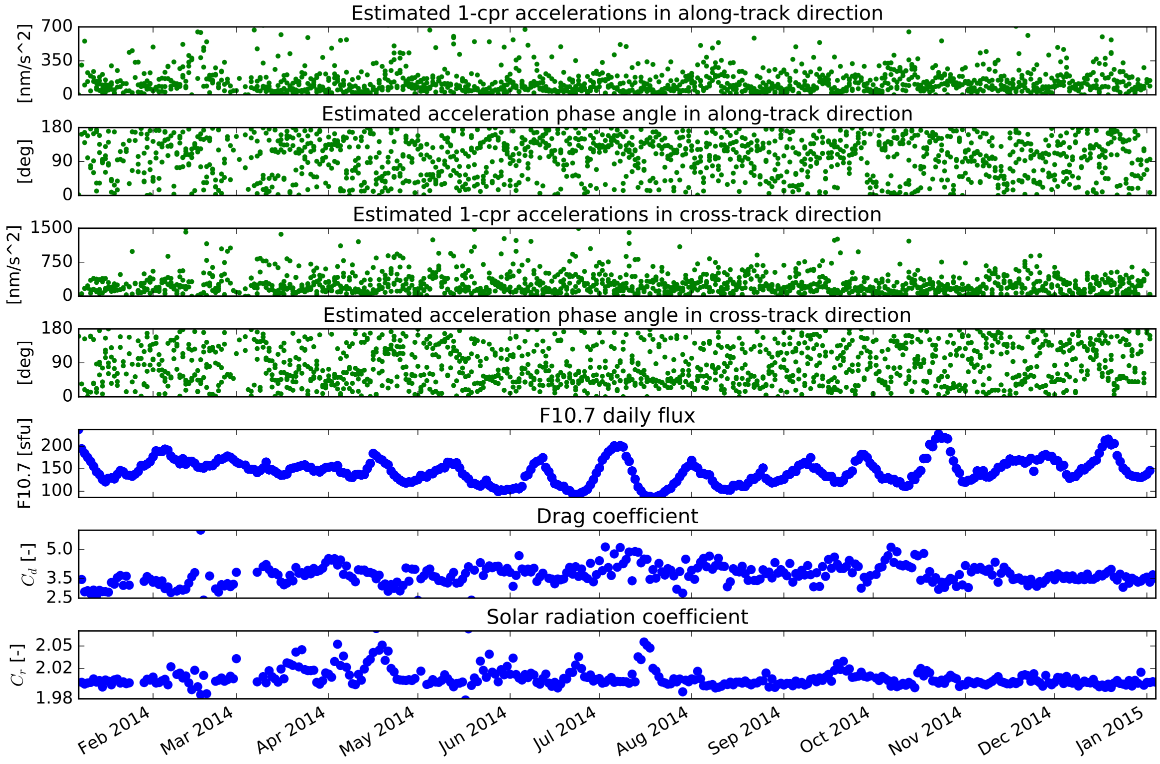

Figure 4.15: All estimated force parameters and daily solar indices

The empirical accelerations show to be rather big compared to the active accelerations as was calculated by Doornbos (2001) where along-track empirical accelerations in the order of 5-15 nm/s^2 where found. Furthermore no direct indication of a systematic trend can be distinguished in the empirical accelerations due to the large scattering. The solar radiation pressure coefficient show small variations over time whereas Weigel et al. (2013) found larger deviations. The drag coefficient estimates on the other hand clearly show larger deviations, but never reach values above 5, whereas Weigel did found values up to 6. A possible cause could be the use of a different atmospheric drag model. Longer time arcs could show better long term seasonal trends.

The effect of the empirical accelerations on the residuals can be seen in the following figures 4.16 & 4.17, where it is seen that a trend is visible within the residual signal without the ACCEL9 card compared to the 2-daily ACCEL9 version. The empirical acceleration correct for this trend by pulling the orbit slightly to a more levelled residual. This shows that apparently the large empirical accelerations are used effectively to correct the orbit slightly. This could explain the large accelerations which were found.

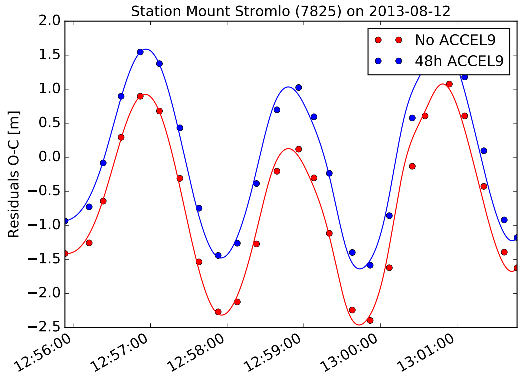

Figure 4.16: ACCEL9 card effect on residuals

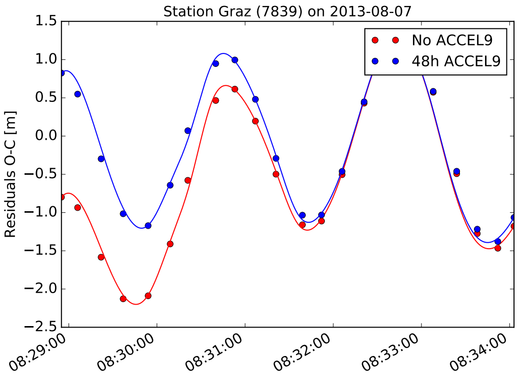

Figure 4.17: ACCEL9 card effect on residuals 2

4.5. Orbit propagation

A small analysis has been made of the propagation and orbit determination quality. As one of the goals of the thesis is to asses the possibility of decreasing the orbit propagation error, this section serves as a reference for the orbit determination without an attitude model.
A seven day orbit determination arc is selected from the 1st of August till the 8th of August 2013 which holds 374 normal points. The inertial i-frame orbit coordinates are compared with respect to the predicted i-frame coordinates in a True of Date reference system. These are created from a proceeding seven day arc, which runs from the 25th of July till the 31st of July 2013 with 286 normal points which is propagated to the first week of August. Both are subtracted from each other which results in figure 4.18. A clear increasing error over time is visible, whereas the norm of the orbit vector(|r|) shows a more steady behaviour after three days of propagation. When these errors are transformed to the l-frame directions (see equation 4.18), it becomes clear the the tangential direction shows an increasing error over time up to almost one kilometre after seven days whereas the radial and normal errors show to grow to about 50 m after seven days.

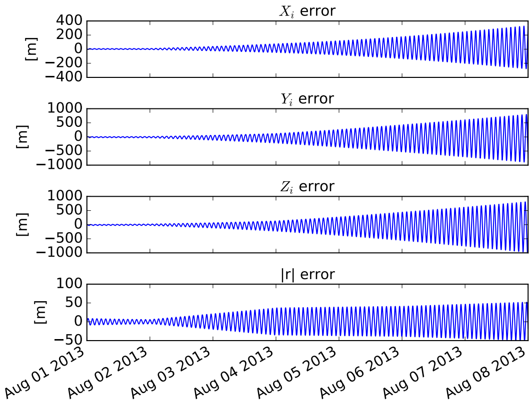

Figure 4.18: Orbit errors in the i-frame

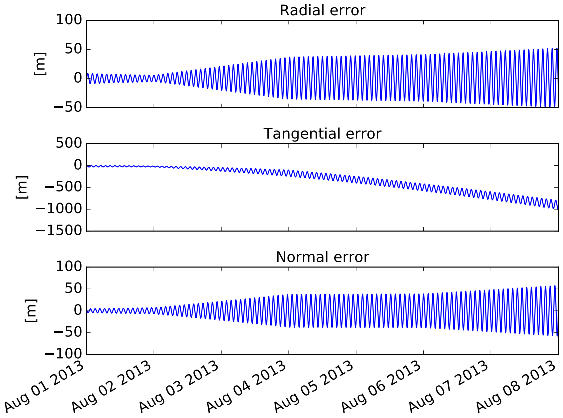

Figure 4.19: Orbit errors along the l-frame

4.6. Station analysis

This section will show the performance of the orbit determination based on on the options given in section 4.2. First a global overview of the availability and distribution of the stations will be given. Next, several station's individual performance will be analysed.

4.6.1. SLR station position

One of the first things needed in using SLR data is the exact location of these stations. Due to the dynamical behaviour of the Earth, station positions tend to shift over time. It is therefore important to use the correct and up-to-date station coordinates in a suitable reference frame. The ITRF is used as a reference frame to hold the estimated coordinates and velocities of the SLR stations. The server *ftp://itrf.ensg.ign.fr/pub/itrf/* is used to collect the most up-to-date station positions using the ITRF2014 system. Envisat was and is tracked by 37 stations, past its end-of-life up to now. These ILRS stations are presented in table 4.6 with their corresponding code and monument number as will be used throughout the thesis.

Table 4.6: ILRS SLR station involved in ENVISAT tracking past its end-of-life (Pearlman et al., 2002)

Monument	Code	Location Name, Country
1824	GLSL	Golosiiv, Ukraine
1868	KOML	Komsomolsk-na-Amure, Russia
1873	SIML	Simeiz, Ukraine
1874	MDVS	Mendeleevo 2, Russia
1879	ALTL	Altay, Russia
1884	RIGL	Riga, Latvia
1886	ARKL	Arkhyz, Russia
1888	SVEL	Svetloe, Russia
1889	ZELL	Zelenchukskya, Russia
1890	BADL	Badary, Russia
1891	IRKL	Irkutsk, Russia
1893	KTZL	Katzively, Ukraine
7090	YARL	Yarragadee, Australia
7105	GODL	Greenbelt, Maryland
7110	MONL	Monument Peak, California
7119	HA4T	Haleakala, Hawaii
7124	THTL	Tahiti, French Polynesia
7237	CHAL	Changchun, China
7249	BEIL	Beijing, China
7359	DAEK	Daedok, South Korea
7403	AREL	Arequipa, Peru
7407	BRAL	Brasilia, Brazil
7501	HARL	Hartebeesthoek, South Africa
7810	ZIML	Zimmerwald, Switzerland
7811	BORL	Borowiec, Poland
7820	KUNL	Kunming, China
7821	SHA2	Shanghai, China
7824	SFEL	San Fernando, Spain
7825	STL3	Mt Stromlo, Australia
7827	SOSW	Wettzell, Germany
7838	SISL	Simosato, Japan
7839	GRZL	Graz, Austria
7840	HERL	Herstmonceux, United Kingdom
7841	POT3	Potsdam, Germany
7845	GRSM	Grasse, France (LLR)
7941	MATM	Matera, Italy (MLRO)
8834	WETL	Wettzell, Germany (WLRS)

4.6.2. Global map

As mentioned previously in section 2.1, the ILRS network consists of 51 SLR stations. From this group, 37 stations have shown to be tracking Envisat past its end of life. However, due to the low priority of tracking of Envisat(currently on the 55th place), the amount of SLR data is limited. From these 37 stations, only a few are consistently tracking Envisat. When investigating the ground tracks in the year 2014, one can clearly see several high concentrations around Western Europe, the West coast of Australia and Northern China as illustrated in figure 4.20.

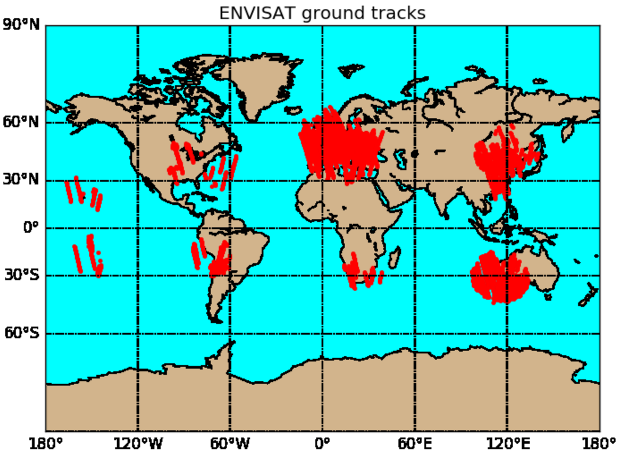

Figure 4.20: SLR ground track of Envisat in 2014

The number of passes over a total time period of two years(2014/2015) confirms the ground tracks in 2014. The four most used stations seem to be the Austrian Graz (GRZL), the Australian Yarragadee (YARL), the Australian Mt. Stromlo (STL3) and the Chinese Changchun (CHAL) SLR station. These four stations exceed by far the other 28 stations as can be seen in figure 4.21 in 2014 and 2015. Also noticeable is the total average length of a certain station, which can be seen as well in figure 4.21. It seems that the total arcs of the SLR station Graz posses significantly more normal points. This might indicate a different normal point window length, but this is not the case after examination of the normal point CRD files. A standard normal point window length of 15 seconds is found for all the stations. This implies two suggestions. The first being the option that Graz simply can track Envisat for longer periods of time. This could occur due to the faster establishment of a connection between the station and the satellite allowing longer arcs. The second option could be that several stations only choose to track Envisat when it passes slightly direct above the station, rather than passing at low elevations.

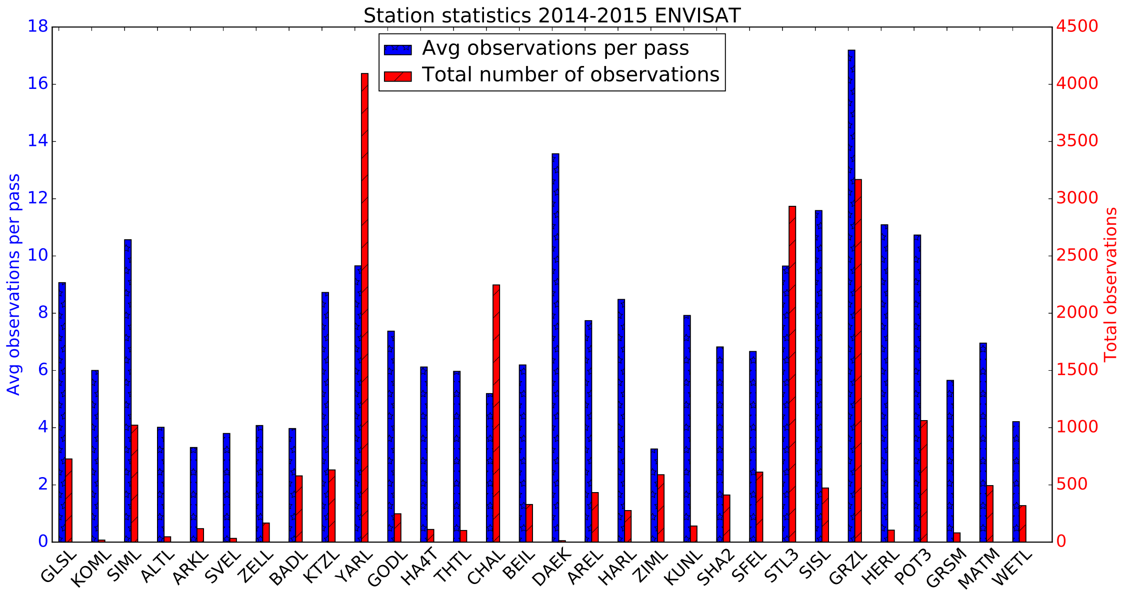

Figure 4.21: Total observations per station in 2014 and 2015

4.6.3. Time between passes

Another interesting item worth investigating is the separation between the individual SLR passes during Envisat's passive state. First an overview of all station passes is given in the period where Envisat is deliberately being tracked as a passive object from June 2013 to October 2016. The result is given as a bar plot in figure 4.22. In this time period, an average separation of about 300 minutes is found considering all normal points.

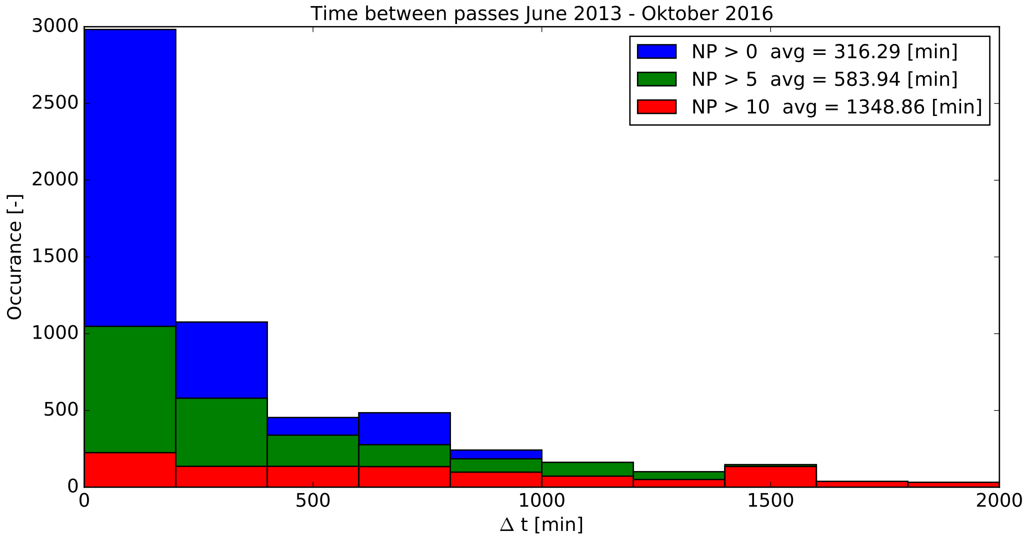

Figure 4.22: Time between passes of Envisat past its-end-of-life

Figure 4.22 shows that it takes on average about three orbital revolutions before Envisat is tracked again by another station no matter how long the arc is. When the minimum number of normal points is increased to higher values, the average separation time increases significantly. When one wants to asses, for instance, only passes with 20 NP's which corresponds to about two revolutions in this time period, the average time between two passes takes about 67 orbits. This is illustrated separately in figure 4.23. These average separation times are considered on a large scale. It would be interesting to see, if certain areas with denser data are available in order to identify smaller trends. Therefore the average of each month is calculated and plotted in figure 4.24. Here, a clear seasonal behaviour is seen. The winter months appear to have higher separations between the normal points. This might be explained by the far higher number of stations in the Northern hemisphere and in Europe where in winter months, the precipitation is higher than in the summer months which results in less SLR favourable conditions, resulting in fewer passes and thus larger gaps in the separation between SLR passes. The summer months thus show a denser distribution of SLR passes.

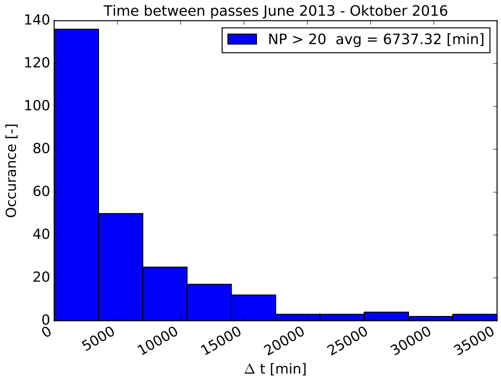

Figure 4.23: Minimum of 20 NP's

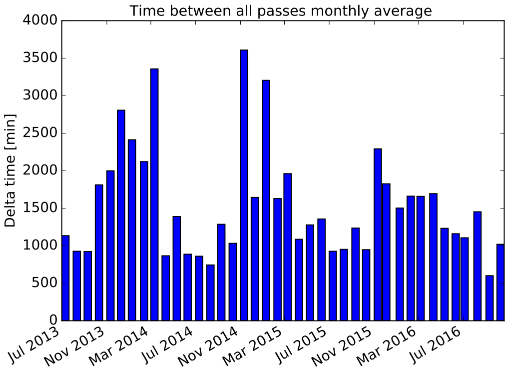

Figure 4.24: Monthly average NP>10

4.6.4. Station quality

Investigating the occurrence of a certain pass length per station shows how often a certain station observes long passes. In this analysis the three largest contributors of Envisat SLR data over the past years are evaluated. When considering Graz, no specific peak in NP-length occurrence can be seen in figure 4.25. On the other hand, Yarragadee clearly shows it has an uneven distribution of pass lengths as can be seen in figure 4.26. It clearly has a lot of small data arcs of about 5 normal points or about 75 seconds. This corresponds to slightly less than half a revolution.

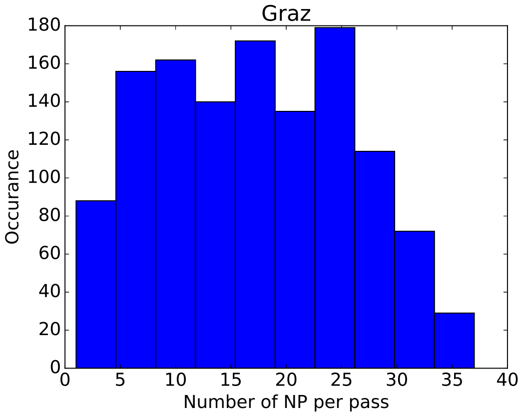

Figure 4.25: SLR station Graz 2014-2015

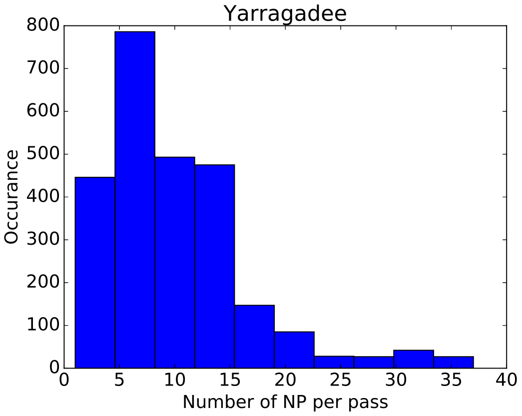

Figure 4.26: SLR station Yarragadee 2014-2015

The third largest contributor of SLR data of Envisat, Changchun, shows a similar NP histogram like Yarragadee as seen in figure 4.27, having primarily short arcs. The same can clearly be seen for SLR station Wettzell in figure 4.28.

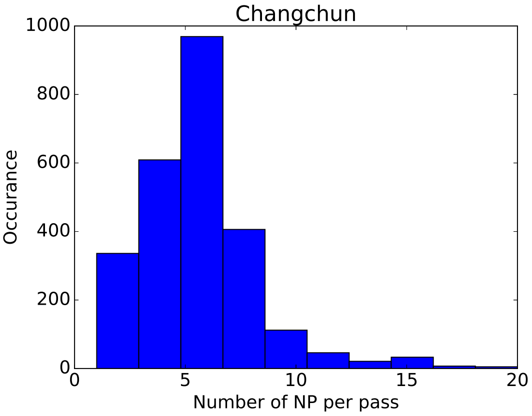

Figure 4.27: SLR station Changchun 2014-2015

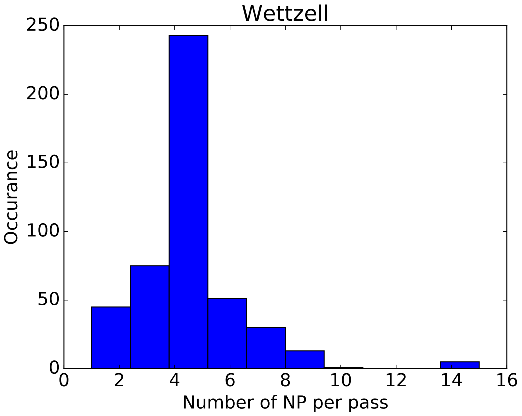

Figure 4.28: SLR station Wetzell 2014-2015

As Envisat has spinning periods larger than 130 seconds in 2014 based on the analysis done by Kucharski et al. (2014), short arc SLR passes could cause problems in the orbit and attitude determination which will be asses in the proceeding chapter 4 and 5. The large offset of about 2 m between the LRR and the COM could create confusing situations for the batched least-squares orbit determination process in GEODYN. Where long arcs which are regarded to be at least longer than one revolution osculate around a certain equilibrium, shorter ones do not.
Evaluating the performance of the orbit determination process for a total period of two years (2014-2015) resulted in the following statistics. Figure 4.29 shows the lowest RMS values of the produced residuals for each station. This could possibly identify a systematic error in a particular station.

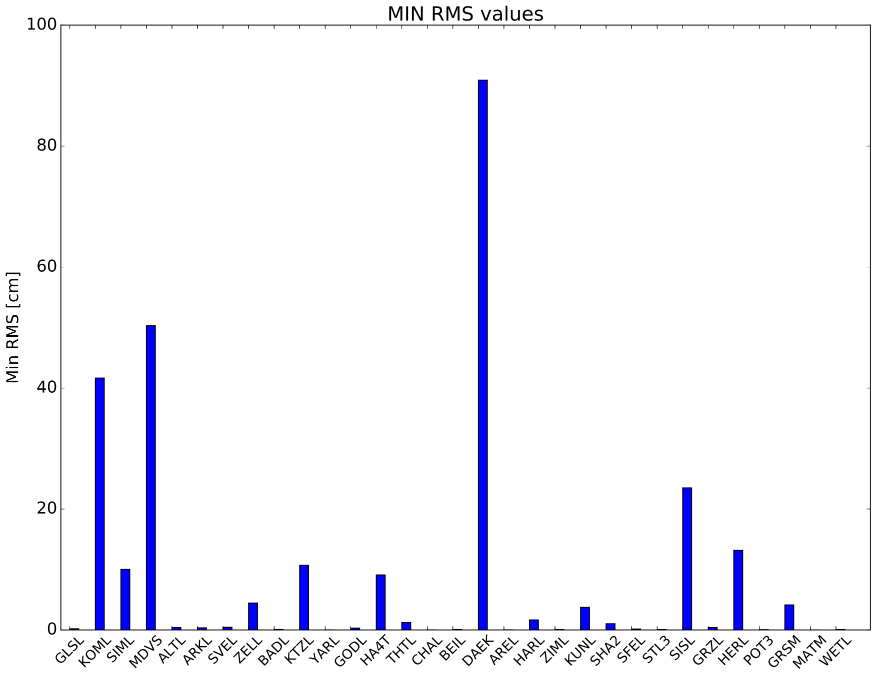

Figure 4.29: Lowest RMS value 2014 and 2015

Station Daedok (DAEK) shows a relatively high minimum RMS value, but holds one of the lowest amounts of NP data and thus is not representative when comparing it with other stations with much higher amounts of data.

Figure 4.30 illustrates the mean of each RMS of a pass for all normal point lengths. It shows that across all stations average RMS values lie in the range of 50-100 cm. This is due to the large amount of passes which do not cover an entire revolution. When considering long passes with one or multiple revolutions, the mean should be far closer to zero.

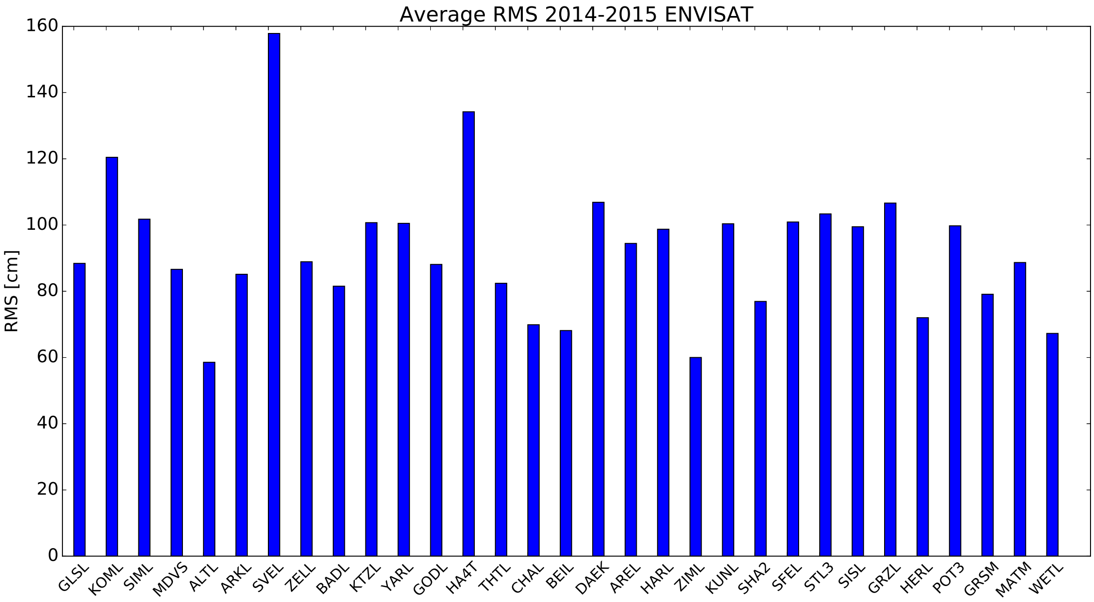

Figure 4.30: Average RMS value 2014-2015 Envisat

4.7. Residuals, a first look

Residuals are computed by subtracting a calculated (C) value from its corresponding observed(O) value. This is often indicated in literature by "O-C". A difference exists due to the fact that the orbital path is centred in the COM of the spacecraft, irrespective of a rotation involved in the spacecraft. The SLR station however does not measure the distance between the station and the COM of the spacecraft but between the station and the LRR. Due to the rotating behaviour of the satellite, an osculating range with respect to the true orbital path exists. The residuals can thus by found by subtracting the actual observed LRR-station vector with the calculated vector which evolves from the orbit determination process. Figure 4.31 shows the principle of the observed(shown in green) and calculated(shown in red) observations vectors.

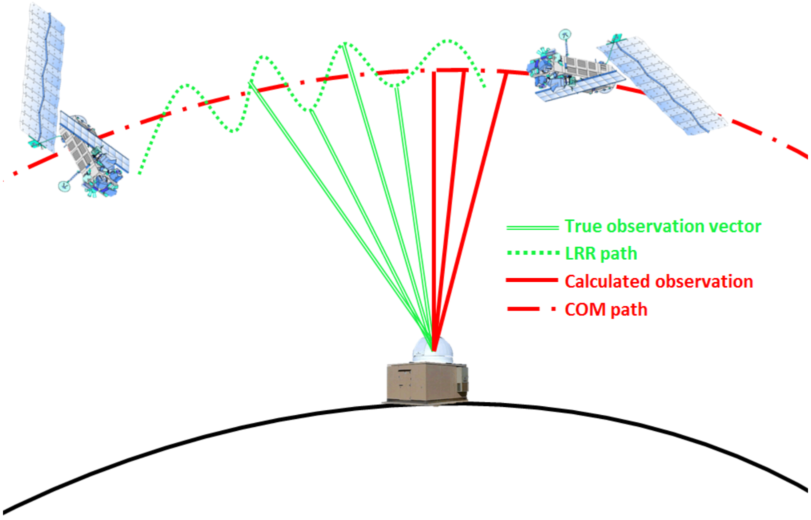

Figure 4.31: SLR residuals sketch

By analysing the residuals of the SLR measurements and the actual orbit one can clearly see an oscillating behaviour. This behaviour is a clear sign of a rotational motion of Envisat. Figure 4.32 shows a clear cyclic period of the rotation as observed by the SLR station in Shanghai. All normal points are evenly spread and the amplitude of about two meters shows the clear evidence of the LRR-COM offset of two meter. On the right hand, figure 4.33 shows an example of the residuals from Graz where a clear gap can be distinguished in the residuals. This type of observation could indicates that at that moment of time, the LRR was blocked by the satellite body or solar panel. Another reason could be that the SLR station at that time does not receive any laser photons back due to for instance atmospheric effects.

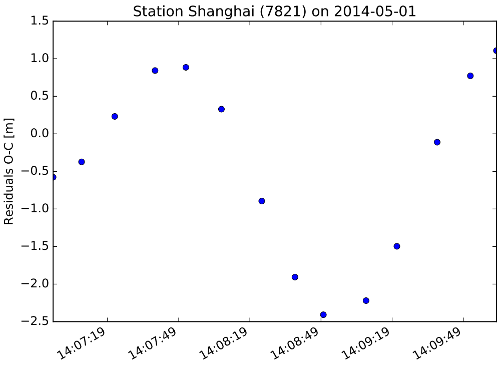

Figure 4.32: SLR residuals example 1

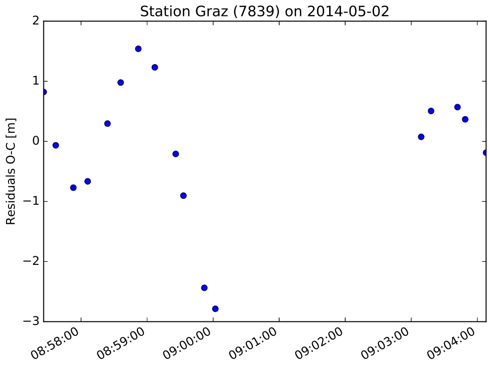

Figure 4.33: SLR residuals example 2

The residuals will form the basis of assessing the rotational behaviour during chapter 5. The Orbit determination process has been repeated for the time arc 2013/05 till 2016/02 and has created a database of residuals and orbit data.

4.7.1. Rotational period

As the residuals clearly shows a periodic behaviour, in the proceeding section, the rotational speed of Envisat will be determined. This analysis has already been performed by Kucharski et al. (2014) and showed interesting results. For this analysis the Lomb algorithm is used just like Kucharski did. This frequency analysis method uses a least-squares approach especially suitable for unequally spaced data (Lomb, 1976). The algorithm fits a sinusoidal signal with a particular frequency which matches the data set the best. The standard Fast Fourier Transform method could be used as well, but requires uniformly spaced intervals. For the case of normal points there should be a constant spacing between the points, but misfires or blocking of the LRR causes several gaps in the data, resulting in an unequally spaced data set. Therefore the Lomb method is preferred. These rotational periods represent the apparent spin period as seen from the ground and not the true inertial spin period of Envisat.

Apparent spin period

A pre build version in Python is used for this algorithm which is incorporated in the "scipy" package. There is however one major limitation in this analysis, which is the limited amount of long data arcs spanning an entire period as was mentioned in section 4.6.4. This results in wrong interpretation of the exact spin period. An example of the performance of a long arc and a short arc is illustrated in the subsequent figures 4.7a to 4.7h. The largest local maximum in the power function of Lomb indicates the specific frequency which matches the residuals.

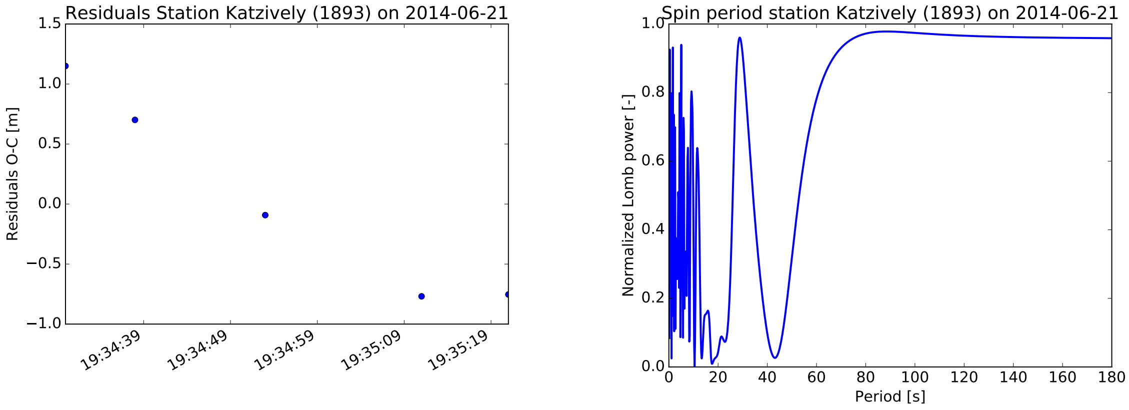

(a) Residual A

(b) Lomb A

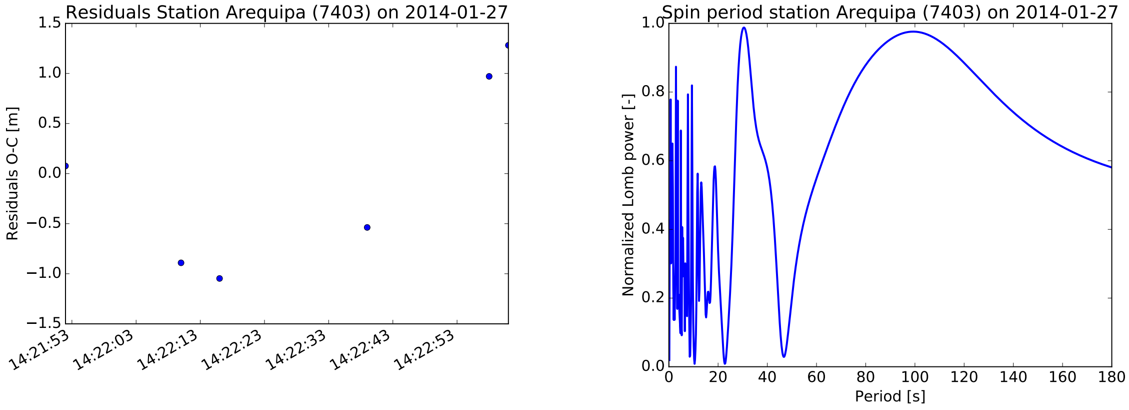

(c) Residual B

(d) Lomb B

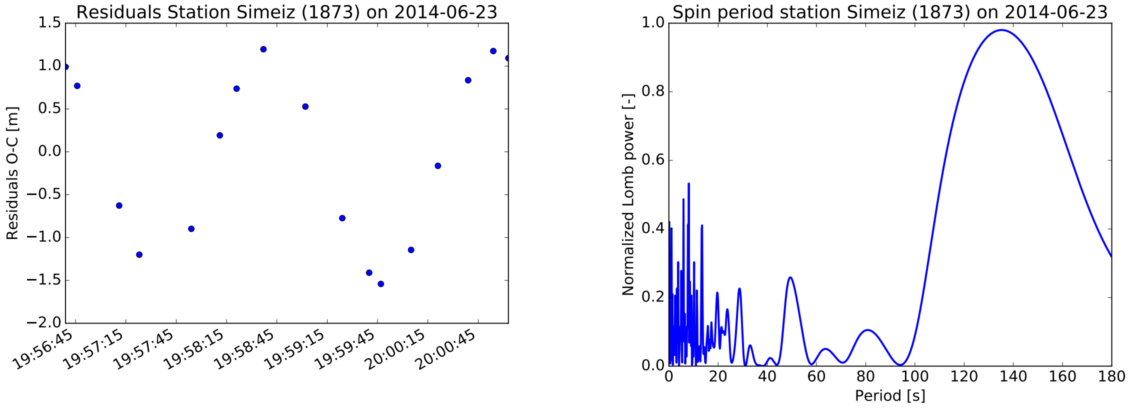

(e) Residual C

(f) Lomb C

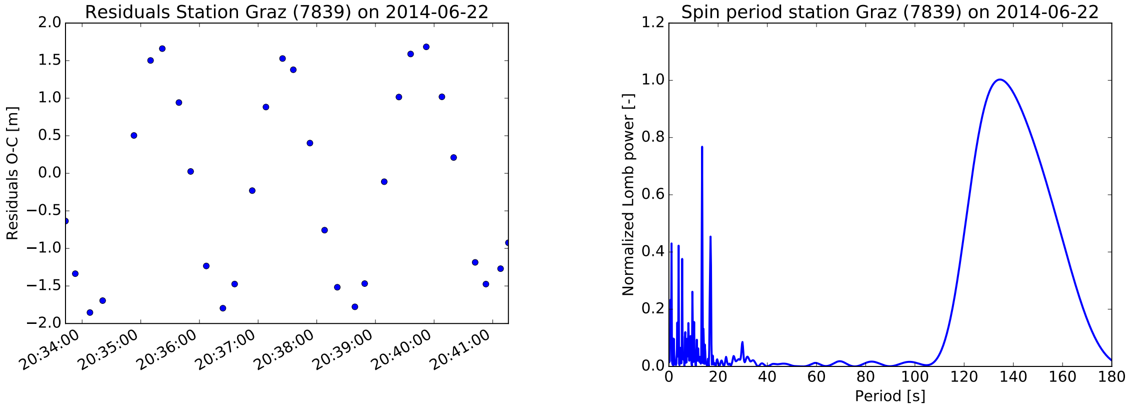

(g) Residual D

(h) Lomb D

Table 4.7: Apparent spin periods for different pass lengths

A way of solving this problem would obviously be to only take into account arcs which cover at least one to even two full periods. The effect of taking longer arcs is visible in figures 4.7a-4.7h. The total data set however strongly diminishes in this way. As seven day arcs are chosen for each orbit determination arc, slightly different residuals exist due to a different data set in the orbit determination run. This effect has been averaged by taking the mean of the period over the seven days. Furthermore, a threshold of a minimum of 25 NP's is selected as a good representation of a pass. This corresponds to a pass of about six minutes covering a minimum of two revolutions. If a linear trend function (least-squares fit) is used for this data set, the difference in RMS becomes clear between a threshold of 20 and 25 NP's as can be seen in figures 4.34 and 4.35. The apparent effect is quite significant for Envisat's case due to its relatively long spin period in relation to the pass duration as was noticed by Kucharski et al. (2014).

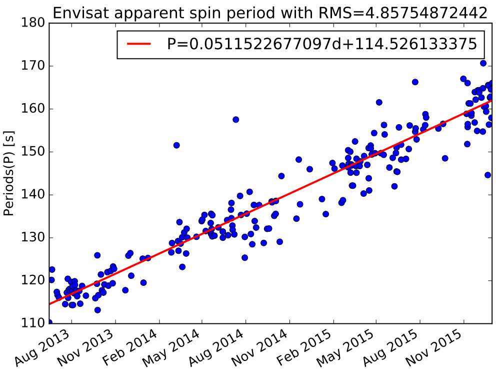

Figure 4.34: Apparent spin period with a threshold of 20 NP's following a Lomb frequency analysis

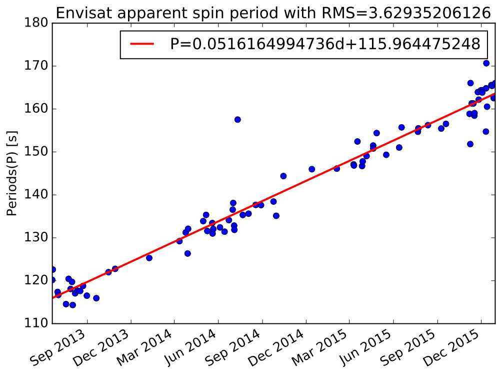

Figure 4.35: Apparent spin period with a threshold of 25 NP's following a Lomb frequency analysis

Inertial spin period

It is important to notice that the specific frequency from the SLR residuals is not the inertial true spin period, but an apparent one. As already mentioned by Kucharski et al. (2014) and Kucharski et al. (2009), the frequency signal of the residuals is affected during a pass as the incident angles of the laser beam in the l-frame changes. In order to correct for this effect, the specific station-satellite geometry/orientation should be taken into account as well as the orientation of the spinning satellite.

The work of Kucharski et al. (2013) involves simulating laser range residuals with a constant spin rate and a known orientation of its spin axis in the inertial reference frame. The spin rate is then varied over each run. By comparing the frequencies of the simulated range residuals with a known inertial input against the measured apparent frequencies and repeating the simulation until the difference between both achieves a minimum gives an indication of the inertial spin period.

Another method mentioned in Kucharski et al. (2009), relates the longitude and latitude shift of the laser beam in the l-frame to this apparent effect. The latitude and longitude angles refer to the spherical representation of azimuth and elevation in the l-frame. This will be calculated in section 4.7.2. Kucharski et al. (2009) uses the following analytical expression of the apparent longitude frequency effect:

$$df_{AL} = LON_{laser,sbc}/(360° \cdot t) \text{ [Hz]} \tag{4.12}$$

Where t represents the duration of the pass, $\text{LON}_{\text{laser,l}}$ the longitudinal change of the laser vector in the l-frame and df_{AL} the apparent longitude frequency shift in the l-frame. For the spherical laser-designed Ajisai spacecraft values where found in the range of 1 mHz. Ajisai orbits a near circular orbit at an altitude of about 1488 km and an inclination of 50°. Next to an apparent longitude shift there exists an apparent phase shift(df_{AP}) as well between the different CCR rings. Values for Ajisai where found to lie around 2 MHz. Combined these corrections result into

$$f_{inertial} = f_{apparent} - df_{AL} - df_{AP} \tag{4.13}$$

4.7.2. Spacecraft local frame (l-frame) passes

In order to asses the latitude and longitude change of a single pass within the l-frame, the vector between the satellite and the station in this frame needs to be known. From the orbit determination process in GEODYN, the position and velocity orbit parameters in a true of date inertial reference frame are already known. By subtracting the station inertial position vector from the satellite inertial position vector, the vector between the satellite and station can be found. Converting this vector from an inertial frame to a local frame results in the requested vector. From this vector, the corresponding latitude and longitude angles as defined in the local l-frame of the satellite can be defined. The conversions follow the conventions from a Cartesian coordinate system(x,y,z) to a spherical coordinate system(radius, azimuth, elevation) where the azimuth and elevation angles correspond to the longitude and latitude angles respectively as given in equation 4.14 and 4.15.

$$latitude = arccos\left(\frac{z}{\sqrt{x^2+y^2+z^2}}\right) \tag{4.14}$$

$$longitude = arctan\left(\frac{y}{x}\right) \tag{4.15}$$

The only unknowns in this analysis are the station coordinates in the i-frame and the conversion of the position vector in the i-frame to the l-frame.
As discussed before in section 4.6, the SLR station coordinates are given in an Earth-fixed reference frame (ITRF2014). This transformation requires a rotation matrix at a certain epoch as the Earth-fixed reference frame rotates with respect to the inertial frame. A script is thus created which takes as input the station ITRF coordinates and time during a pass which returns the station coordinates in the inertial frame at that specific epoch.

The conversions between theses frame is rather complex and requires information about precession and nutation of the earth's spin axis. The python package from the United States Naval Observatory NOVAS astronomy library (NOVAS) is used in order to complete this rotation. NOVAS is a powerful package which includes polar motion, Earth's rotation, precession and nutation. Computations are said to be accurate under a milli arc second. NOVAS' tool "ter2cel" is used which converts a geodetic position vector (terrestrial) to a geocentric(celestial) position vector. To be more specific, the function converts a position coordinate in the ITRF(rotating earth-fixed) to the Geocentric Celestial Reference Frame (GCRF). This is a local inertial non-rotating reference system. As another input it takes the x and y coordinates from the celestial intermediate pole with respect to the ITRS pole. This information is available from the IERS which produces these parameters each day. It can be downloaded from the Earth Orientation Center servers via *hpiers.obspm.fr*. Furthermore, a precession-nutation model IAU 2000 is selected where the Earth Orientation Parameters (EOP) are given with respect to the ITRF2008. Finally a Julian date in UT1 format needs to be given. The UT1 time format, commonly known as the Universal Time, is selected as it is independent of station location. Where UTC is linked to atomic clocks, UT1 is dependant on the specific length of day. The relation between both is linked through a specific offset as

$$UT1 = UTC + \Delta(UT1) \tag{4.16}$$

Where ΔUT1 can be found from the IERS website under Bulletins A and B. These values are by definition quite small with typical values under a second.

As the inertial orbital parameters of Envisat from GEODYN are not exactly given at the time of a certain Normal Point, this data should be interpolated accordingly to that certain time stamp. In order to do so, the python package "scipy.interpolate" is used where a cubic spline interpolation is used. Orbit data is generated each 10 seconds. The corresponding orbit data set which is selected to be interpolated consists of a data set ranging from the start of the pass until the end where these times are rounded to the previous and next time step. In this way the entire pass is enclosed by orbit data. As the interpolation occurs in a single dimension, each three-dimensional coordinate is treated separately after which they are re-combined to form a three-dimensional vector. Figure 4.36 shows an example of a pass which is being interpolated between the orbit and laser data.

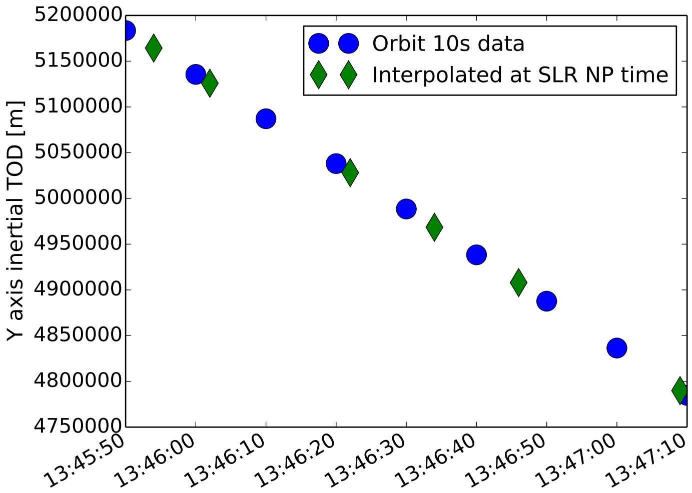

Figure 4.36: Interpolation example y-coordinate

After interpolation, the vector algebra can start. Vectors can be subtracted and added to/from each other if and only if they are defined in the same frame, in this case the i-frame. The observation vector can be deduced from the inertial orbit vector and station vector by using:

$$\vec{r}_{obs,com,i} = \vec{r}_{satellite,i} - \vec{r}_{station,i} \tag{4.17}$$

as can be seen in figure 4.37.

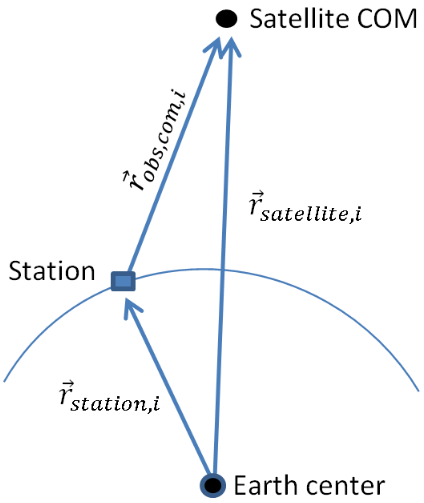

Figure 4.37: Observation vector in inertial frame

The observation vector has been defined in the inertial frame as well and should thus be converted to the local l-frame in order to evaluate the specific longitude and latitude information for each pass in the l-frame. By simply flipping the sign of $\vec{\mathrm{r}}_{\mathrm{obs,com,i}}$ one ends up with the vector from the satellite towards the station. In this case this vector is now centred in the satellite's COM.

Transformation from an inertial celestial frame to the local orbit l-frame are based on the following transformations as found in Tapley et al. (2004). Assumed is that the l-frame is fixed to the orbit at all times.

$$\begin{bmatrix} U_R \\ U_T \\ U_N \end{bmatrix} = R_{LI} \begin{bmatrix} i \\ j \\ k \end{bmatrix} = \begin{bmatrix} \epsilon_x & \epsilon_y & \epsilon_z \\ \delta_x & \delta_y & \delta_z \\ \alpha_x & \alpha_y & \alpha_z \end{bmatrix} \begin{bmatrix} i \\ j \\ k \end{bmatrix} \tag{4.18}$$

Where the unit vector $\mathrm{U_R}$,$\mathrm{U_T}$,$\mathrm{U_N}$ represent the radial, tangential and normal unit vectors as given in a local orbit frame where the radial direction is assumed to be the primary axis. The unit vectors i,j,k represent the unit vector between the satellite and the station in the inertial frame $\vec{\mathrm{r}}_{\mathrm{obs,com,i}}$. The elements of the transformation matrix($\mathrm{R_{LI}}$) itself follow from

$$U_R = \frac{\vec{r}_{sat}}{|\vec{r}_{sat}|} = \epsilon_x i + \epsilon_y j + \epsilon_z k \tag{4.19}$$

$$U_N = \frac{\vec{r}_{sat} \times \vec{v}_{sat}}{|\vec{r}_{sat} \times \vec{v}_{sat}|} = \alpha_x i + \alpha_y j + \alpha_z k \tag{4.20}$$

$$U_T = U_N \times U_R = \delta_x i + \delta_y j + \delta_z k \tag{4.21}$$

Where $\vec{\mathrm{r}}_{\mathrm{sat}}$ and $\vec{\mathrm{v}}_{\mathrm{sat}}$ represent the position and velocity vectors of the satellite's orbit in the inertial frame (i-frame).

Now that the observation vector is found in the local l-frame, the corresponding longitude and latitude angles may be defined. The standard conversion of Cartesian coordinates to spherical may be applied to the l-frame as well as was already denoted in equations 4.14 and 4.15. This results in the following conversion which follows the conventions as shown in figure 4.38

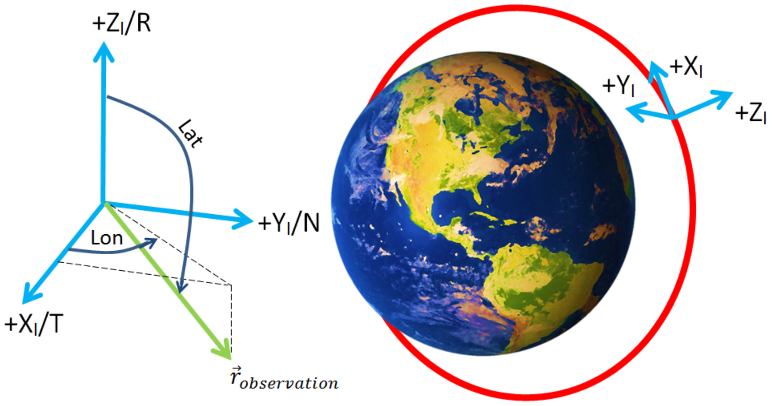

Figure 4.38: RTN frame to Lat/Lon angles

The local x-direction corresponds to the tangential along-track direction($\mathrm{U_R}$), the local -direction to the normal direction($\mathrm{U_N}$) and the local z-direction to the radial direction($\mathrm{U_R}$). Following these conventions of latitude and longitude, an overhead pass corresponds to latitude angles which passes 180°. The laser signal points in the direction of the station but the radial direction however points in the direction of the center of the Earth.

As the laser signal will always come from below the satellite in the local frame, the latitude range could lie between +90° and +180° together with a full 360° longitude range. An example is shown in figure 4.39 where data from June 2013 until December 2013 is plotted in a polar/skyplot. Next to it is the same figure from Kucharski et al. (2014) where data from April until October 2013 has been plotted. Both have the same longitude conventions, but different latitude conventions. Kucharski has taken its latitude positive from the XY(Tangential-Normal) towards the positive z-axis(in radial direction). This means that in figure 4.40 a latitude angle of -90° corresponds to the 180° pass of figure 4.39.

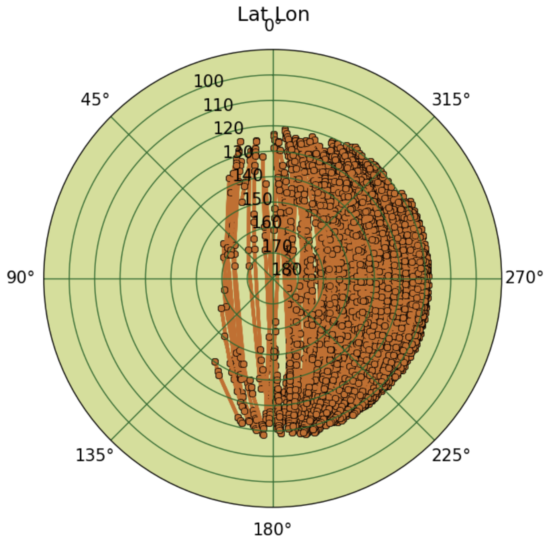

Figure 4.39: Lat/Lon 06/2013 - 12/2013

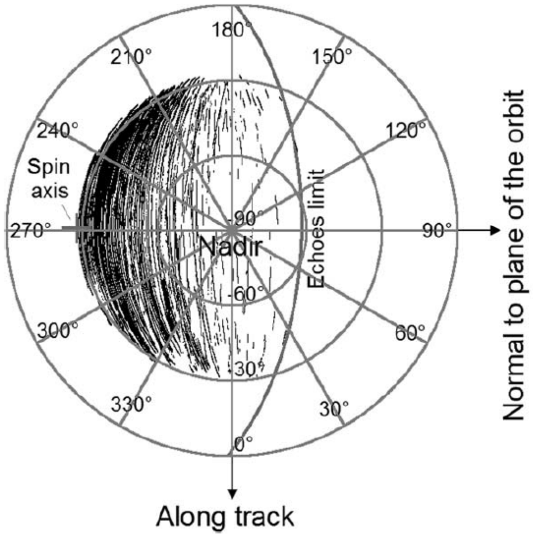

Figure 4.40: Lat/Lon 04/2013 - 10/2013 (Kucharski et al., 2014)

This figure already gives the first insights in the attitude state of Envisat and makes it possible to draw several first conclusions. Due to the viewing cone angle restrictions of the LRR, the satellite can only be observed in specific pass geometries. It is clearly visible that Envisat is mainly being tracked when it passes on the inverse normal side of its local orbit frame. This means that its orientation must lie in this direction such that it barely can not be tracked from the other side. A slight portion of passes do however show that it is possible to be tracked on the normal side. This indicates that its orientation is pointed slightly up with respect to the nadir vector. How much can be determined by using information of the viewing cone of the LRR which has a cone-half angle of 60°. It seems that indeed this angle can be found in the skyplot as the observations show clear limits. By making the assumption that the LRR lies parallel to the satellite's axis of rotation Kucharski found a spin axis location in the l-frame at a longitude angle of 269.22° and a latitude angle of -28.14° by fitting this reflection cone over the observations. This assumptions does not allow for the evaluation of any precession in the spin axis. When evaluating the sky plot over several years up till 2016 no indication of a change in pass direction is visible. This might confirm the assumption made by Kucharski that the spin axis orientation of Envisat is stable in the local orbit frame over the years.

4.8. Conclusions

The orbit determination process chapter has been existentially discussed the station analysis, the GEODYN program, the creation of residuals and attitude models for COM-LRR corrections and its implementation in GEODYN. The separation between Envisat passes reaches on average about three orbits. This values increases significantly when longer passes are considered. During the summer months longer passes show denser distributions. Using a cannonball model, the oscillating residuals are produced which shows the rotational behaviour of Envisat. Large empirical accelerations are found due to the low amount of data available in the orbital arc of seven days. This shows a significant effect on levelling the residuals. An apparent spin period shows the steady decrease of rotational velocity over the years. A skyplot showed that Envisat could only be observed from a certain direction in its local frame which remained stable over the years confirming the estimate of the spin axis direction as was found by Kucharski et al. (2014). Orbit determination of the active Envisat allowed to validate the use of the COM-LRR correction capabilities within GEODYN.

5

Simulated attitude determination

> *"There's really just one thing I can control: my attitude during the journey, which is what keeps me feeling steady and stable"*
>
> — *Chris Hadfield* Canadian astronaut

Now that the the simulator is created all pieces necessary for the attitude determination are available. As mentioned before, first only simulate data is considered as it allows validation of the found results. In chapter 6, the real SLR data determination is covered based on the conclusions from this chapter.

This chapter will study attitude determination processes based on simulated SLR residuals only. Several other passive attitude observation techniques exist as well, like using light curves. This technique analyses the reflected photometric signal from the body as a result from the scattered sunlight on particular faces of the body as is shown by Shakun et al. (2013). Another used method uses ISAR images from a ground-based station and matches a wireframe model to the observations in order to determine its attitude state as described by Fiege et al. (2013). SLR is chosen for this thesis due to the relatively large and constant availability of the data. First, in section 5.1, the process of creating simulated residuals is addressed. Next, in section 5.2, the estimation of these simulated residuals are evaluated using various techniques for local passes only. Section 5.3 shows the attitude determination process using multiple station options. Here, different estimation techniques are tested and several conclusions are drawn in section 5.4.

5.1. Simulated residuals

The simulated residuals are needed in order to validate the correctness of the attitude determination process. This is a approach which is commonly not used in previous research done by Kanzler et al. (2015) and Schildknecht et al. (2015). Now that the rotational model is created in chapter 3 and the orbit data is created in chapter 4, the simulated residuals can be created. This is done using the same vector algebra technique as applied for the range observation as given in figure 4.37 but now corrected for the rotating LRR offset in the l-frame. In order to create a pass of simulated residuals, four major consecutive steps need to be performed. First the position vector between the station and the COM of the spacecraft needs to be found. This occurs in the ECI frame. Then, a transformation between the ECI and the local l-frame needs to occur. The corresponding true observation vector follows from the rotating LRR vector and the COM observation vector in the l-frame. The simulated range residuals finally follow from the difference between the observed range and the true LRR position range. Figures 5.1 and 5.2 illustrate the transformations between the different vectors which is summarised in the steps below.

1. Vector between COM and station in an inertial frame: $\vec{r}_{obs,com,i} = \vec{r}_{sat,i} - \vec{r}_{stat,i}$

2. Transform observation vector to local frame $\vec{r}_{obs,com,i} \rightarrow \vec{r}_{obs,com,l}$, illustrated in figure 5.1 and 5.2.

3. Vector between station and LRR in local frame: $\vec{r}_{obs,lrr,l} = \vec{r}_{obs,com,l} - \vec{r}_{lrr,l}$

4. Simulated residuals: Observation - Calculated = $|\vec{r}_{obs,lrr,l}| - |\vec{r}_{obs,com,l}|$

The simulator takes seven initial inputs as given in equation 5.1 in order to create a set of simulated residuals over a certain time span. These seven can be subdivided in two groups. As a first set of arguments, spin axis information should be provided. Based on Euler's rotational theorem, a spin axis location and initial velocity and direction should be given. As mentioned in section 3.2.2, the spin axis can be given an initial location based on the spherical coordinate system which takes an azimuth (Az) and elevation (El) angle as input. Furthermore, the initial rotation velocity (ω_0) and direction (counter clockwise or clockwise) should be provided. Next, the initial attitude from where the rotational integrator takes over, needs to be given. In order to avoid singularity issues, a set of quaternions needs to be used in stead of Euler angles. This results in the following state vector:

$$\mathbf{A_0} = \begin{bmatrix} Az & El & \omega_0 & q_0 & q_1 & q_2 & q_3 \end{bmatrix} \tag{5.1}$$

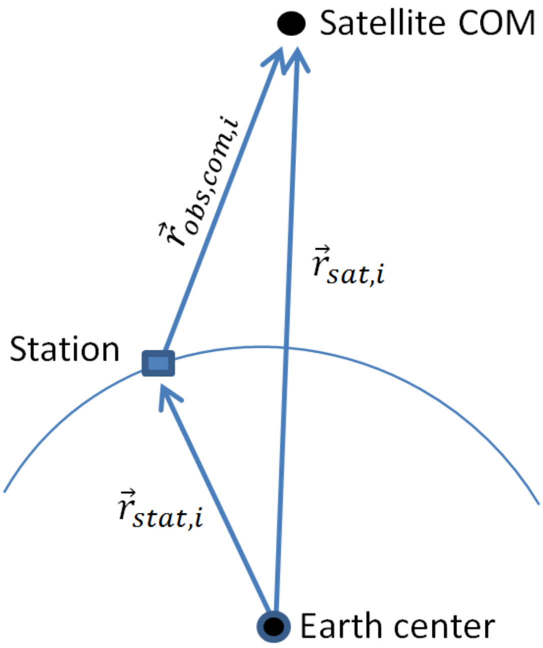

Figure 5.1: Inertial frame

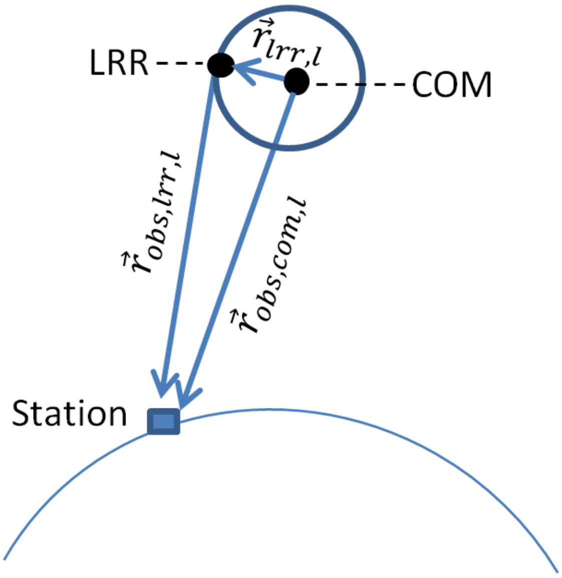

Figure 5.2: Local frame

As an example setup the following input parameters are given to the simulator where its corresponding vectors are plotted in figure 5.3 illustrating the inertial frame and figure 5.4 the local frame.

Table 5.1: Sample initial state variables

Az [deg]	El [deg]	ω_0 [deg/s]	q_w [-]	q_x [-]	q_y [-]	q_z [-]
270	-28	2.88	0	0	0.515	0.8571

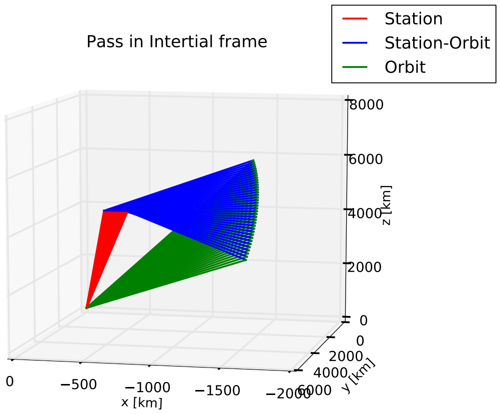

Figure 5.3: Position vectors in inertial frame

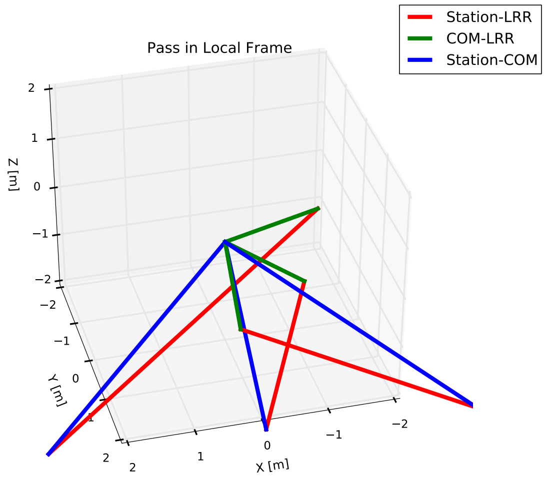

Figure 5.4: Position vectors in Local frame

The corresponding residuals are shown in figure 5.5 where a pass from Graz is simulated on the 1st of August 2013.

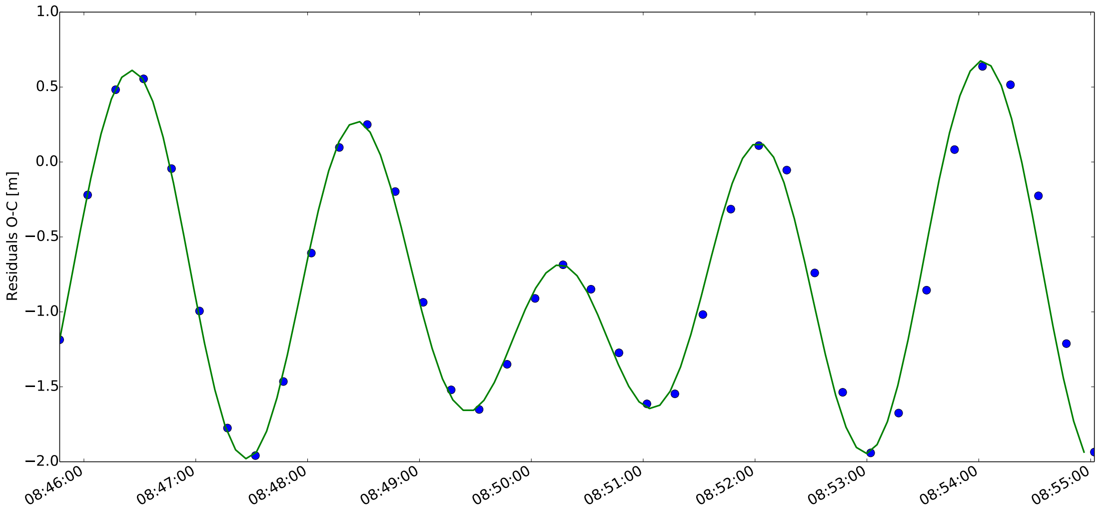

Figure 5.5: Example of simulated residuals of Graz on 2013/080/1 with interpolated line

5.1.1. Effect of COM variations on residual signal

The center of mass position was assumed to be fixed since end-of-life in the Envisat specific frame. If for some reason the left-over fuel would be vented even further, the x position in the f-frame of the COM would shift further in the negative direction. As is still unknown what exactly happened to Envisat a possible collision could also be a possibility. In this case the COM of the vehicle could also be shifted in all directions. Small offsets from the nominal assumed value are given in figure 5.6.

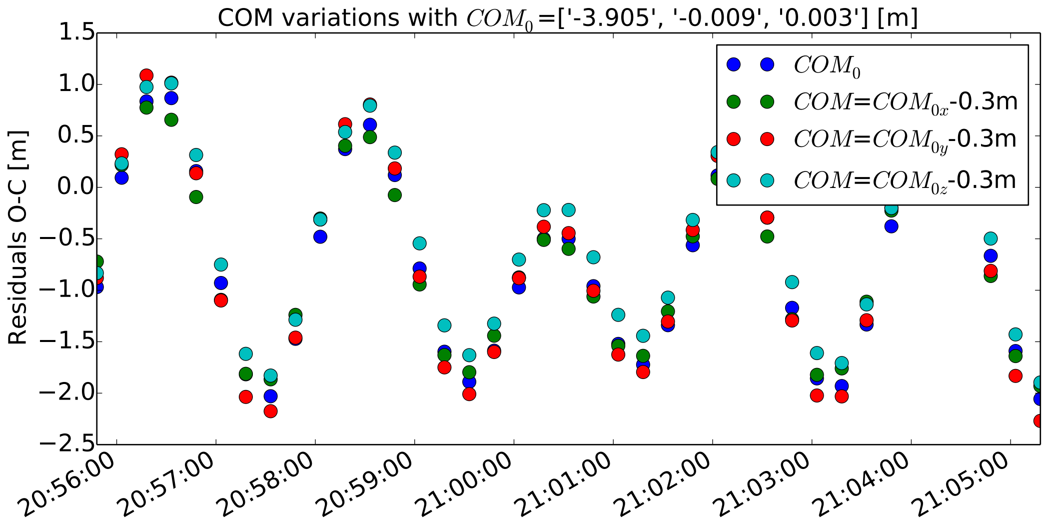

Figure 5.6: COM variations and their effect on the residuals

From this figure it is shown that slight variations in the COM position, have slight variations in the residual signal under the assumption that the inertia tensor remains constant. Moment of inertia changes will result in an increased offset over time, as it only effects the integration process. Taking into account shifts in moment of inertia is not considered in this thesis.

5.1.2. Station passes- Time in view

When considering simulated station passes, specific passes from all ILRS stations can be selected. This makes that specific station-satellite connection times could be derived first as this is a major input in the simulator. There are however three main constraints which are opposed to this analysis. First there is a ten degree station elevation margin which would eliminate major atmospheric(or other blocking) corrections. Next there is a visibility model. As was seen in figure 4.39, Envisat could only be observed from certain latitude/longitude combinations due to the orientation of Envisat and its relative LRR position. This results in blocking of the LRR. This constrains the amount of passes significantly. Last, there is the visibility cone of the LRR itself. The LRR has been designed in such a way that the half cone angle can not exceed 60° from its normal and does not have any restrictions in terms of azimuth such that a full 360° visibility is possible.

Theory Station pass geometry and earth coverage is a well studied subject. Wertz (2009) describes the necessary theory behind the computations. This section will show the analytical theory behind these station passes.

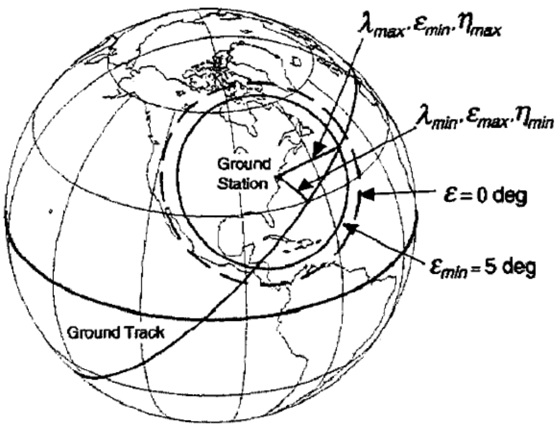

Figure 5.7: Earth coverage ground track (Wertz, 2009)

Figure 5.7 shows the standard case of a the access area of a satellite in orbit. From the minimum elevation angle (ϵ_{min}), the maximum Earth Central Angle (λ_{max}) and maximum nadir angle (η_{max}) can be derived using:

$$\lambda_{max} = 90° - \epsilon_{min} - \eta_{max} \tag{5.2a}$$

$$\sin\eta_{max} = \sin\rho\cos\epsilon_{min} \tag{5.2b}$$

$$\sin\rho = R_{\oplus}/(R_{\oplus} + H) \tag{5.2c}$$

Where the angular radius as seen from the satellite is expressed as ρ and is approximately 63° for Envisat. A clear circle is visible on the Earth, which shows that when the satellites visibility circle is within this range, a connection is theoretical possible.

The minimum Earth central angle, λ_{min}, is governed by the angle between the satellite's ground track and the particular ground station. Together with instantaneous latitude (ϕ) and longitude (λ) of the orbit pole (op) and ground station (gs) this angle becomes

$$\sin(\lambda_{min}) = \sin(\phi_{op})\sin(\phi_{gs}) + \cos(\phi_{op})\cos(\phi_{gs})\cos((\Delta\lambda)) \tag{5.3}$$

Where $\Delta\lambda$ equals the longitude difference between the ground station (gs) and the orbit pole (op). The orbit pole is defined as the pole of the orbit plane at the time of observations and its latitude and longitude is related to the following two relations

$$\phi_{op} = 90° - i \tag{5.4a}$$

$$\lambda_{op} = L_{node} - 90° \tag{5.4b}$$

The inclination (i) and longitude of ascending node (L_{node}), are thus the two parameters needed to describe the spacecraft's circular orbit with respect to the ground track. In the simplified case of a non-rotating earth the time in view (T) can then be found as

$$T = \frac{P}{180°}\arccos\left(\frac{\cos\lambda_{max}}{\cos\lambda_{min}}\right) \tag{5.5}$$

Where P equals the orbital period of the satellite.

This access time refers to the theoretical time in view of the satellite with respect to a certain ground station. The actual earth coverage however is governed by the the time the instrument (Laser Retro Reflector (LRR)) can actually be observed by the station. These access areas can be regarded the same if an omnidirectional antenna is selected. The LRR has however a particular viewing cone (cone half angle α) which together with its attitude pose constraints on this access area, also referred to as instantaneous footprint area (Wertz, 2009). What actually happens when the symmetry axis is shifted from nadir looking to a slight offset over an angle ϕ is sketched in figure 5.8.

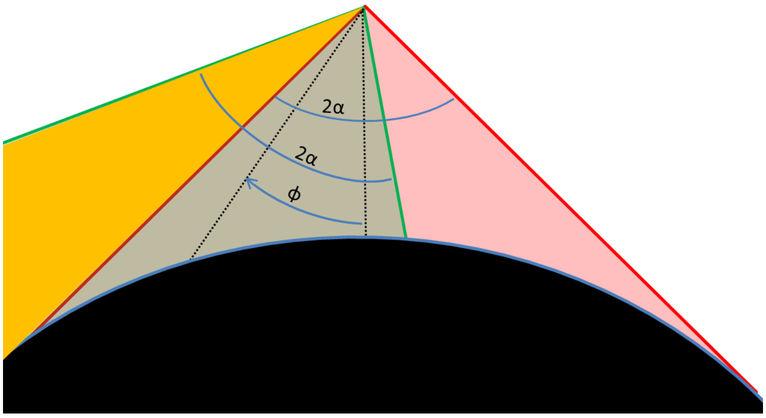

Figure 5.8: Field of view sketch of the viewing cone of the LRR with a half cone angle of α. Red: Nominal nadir looking. Green: With offset ϕ. Orange: outside maximum angular radius

A certain amount of the viewing cone(orange) will no longer be useful as it points outside the maximum angular radius ρ as shown by the red outer lines in figure 5.8. When the instrument is no longer nadir looking, the ground trace will no longer represent a circular access area as will be shown in figure 5.9. This sketch shows the case where the angular radius approximates the half-cone angle of the LRR. As is the case for Envisat, the angular radius is about three degrees larger than the half-cone angle. This results that an elevated spin axis would allow for a possible larger footprint area on the elevated side. It has been decided to use STK as a simulation tool to asses the start-stop times given a particular viewing cone orientation and size as will be discussed in the proceeding paragraph.

Systems Tool Kit (STK) When only considering minimum elevation angles the start-stop time of a specific station pass can be analysed. STK can be used to give a start stop time while allowing constraints on the cone angle, minimum elevation and orientation. Before STK is used as a tool to calculate the pass times a small verification is performed.
STK takes TLE data as an initial state and propagates the orbit using a simple SGP4 propagator. As a benchmark the real SLR start/stop times are compared to the ones from STK using the following simple settings for a seven day arc from the first of august 2013 till the 7th of August 2013. The LRR has a half cone angle of 60° and is rotated in the l-frame with corresponding azimuth and elevation spin axis angles of +270° and -28° respectively, together with the assumption that the Z_b-axis coincides with the spin axis as was assumed by Kucharski et al. (2014). Figure 5.9 shows the corresponding coverage (green) next to the coverage from the nominal attitude state with a nadir looking LRR (red).

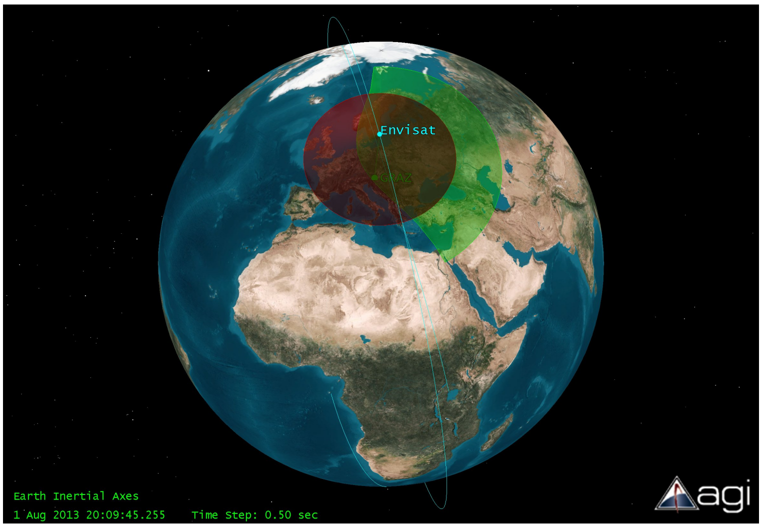

Figure 5.9: Nominal vs passive state LRR pointing using STK

Furthermore, an elevation cut-off angle of 10° is selected just like in the GEODYN orbit determination runs. Only one station (Graz, 7839) was considered as a sample case. The corresponding contact times are given in table 5.2. Where "***" indicates there is no corresponding pass. When comparing both lists some conclusions can be drawn. First there are quite some gaps in the real SLR data passes. This is easy to understand as each station in reality does not track each satellite it encounters. Graz is tracking Envisat regularly as from the 16 theoretical possible passes, only 4 are not being tracked. Next there seems to be some difference between the actual stop start times. This might be due to the fact that no rotation was assumed which could block possible signals or even point further. Other reasons could include slightly wrong orbit predictions which result in re-calibration during first contact, and other operational constraints.

Table 5.2: SLR vs STK

	Real SLR data		STK data	
Date	Start time [UTC]	End time [UTC]	Start time [UTC]	End time [UTC]
13/08/01	8:48:00	8:54:46	8:45:47	8:55:07
13/08/01	20:09:05	20:11:47	20:06:13	20:10:11
13/08/01	21:46:56	21:51:06	21:44:24	21:51:08
13/08/02	8:11:12	8:16:21	8:10:19	8:17:04
13/08/02	9:55:24	9:56:50	9:51:11	9:55:08
13/08/02	21:09:22	21:15:20	21:06:20	21:15:40
13/08/03	***	***	9:13:48	9:19:42
13/08/03	20:31:08	20:37:39	20:32:36	20:36:12
13/08/04	***	***	8:35:41	8:44:31
13/08/04	***	***	21:33:30	21:41:14
13/08/05	***	***	8:00:35	8:05:58
13/08/05	9:40:28	9:41:48	9:39:59	9:45:45
13/08/05	20:57:09	21:05:17	20:55:53	21:05:27
13/08/06	9:02:59	9:10:35	9:01:29	9:11:21
13/08/06	20:22:13	20:28:25	20:20:40	20:27:23
13/08/06	22:02:13	22:06:55	22:01:42	22:06:01

Overall it can be said that using STK provides a basic way of evaluating the specific start/stop times of certain passes based on a simple approximation of its attitude. As for simulation purposes, the accuracy of a specific start and stop times are not considered to have a large effect on the attitude determination performance, therefore STK will be further used for providing this data while using the assumptions on the spin axis.

5.2. Attitude Estimation

Now that a known residual set is created, a corresponding suitable estimation procedure must be found. By varying the initial parameters $\mathbf{A_0}$ as introduced in equation 5.1, a match with the simulated residuals can be found. The procedure in finding this solution is in fact an optimization problem, where the total difference between the estimated residuals ($\nu_{\text{estimated}}$) and the simulated (true) residuals ($\nu_{\text{simulated}}$) needs to be minimized. This results in the desired state where $\Delta\nu = |\nu_{simulated} - \nu_{estimated}|$ needs to be minimized where the norm is taken from the difference between all simulated residuals and all true residuals. A well-used approach in this optimization is the least-squares approach.

5.2.1. Least-squares

Determining attitude and orbital states based on a-priori-information and models relies on several estimation techniques. Just like the orbit determination procedure which relies on a least-sqaures approach, the attitude determination procedure can be set up.

State estimation uses the partial derivatives of the observables with respect to various solved-for parameters to correct an a priori estimate of the parameters. Updating the state vector can either occur sequentially or as a batch estimator. Sequential or recursive estimation uses a new estimate of the state vector after each observation. The batch estimator on the other hand uses the partial derivatives of all the observations in order to produce a single update of the state vector. Wertz (2012) argues that a sequential estimator is more sensitive

to individual data, thus converging to a solution more quickly, but on the other hand being less stable than the batch estimator.
All estimation techniques use three main elements. These are the actual state vector (**x**), the observation vector (**y**) and observational model vector (**z**). Table 5.3 shows the difference between the three elements.

Table 5.3: Estimation process parameters

	x	**y**	**z**
Dimension	m	n	n
Composition	Attitude variables needed for attitude determination	Observation measurements	Predicted values of observational vector based on estimated vector elements **z**=**g**(**x**,t)

Scipy-python An open-source python package called "scipy" which includes quite some optimization tools is used which is able to solve a nonlinear least squares problem. Within this package, several minimization methods can be selected such as the Trust Region algorithm which is suitable for large sparse problems with suitable bounds, a dogbex algorithm which is not recommended for rank-deficient Jacobians and the Levenberg-Marquardt algorithm which unfortunately does not handle bounds. As mentioned by Wertz (2012), the Gauss-Newton differential correction procedure (batched least squares) has the problem it sometimes does not converge unless the a priori estimate is close enough to a good appropriate value. The gradient search method may be used to overcome this problem, but this again has the disadvantage of slow convergence when the solution is approached. The solution lies in the algorithm from D.W. Marquardt(also called the **Levenberg-Marquardt** method) which optimizes both techniques. It chooses the appropriate method based on each situation. That is, when the parameters are far from their optimal value, the algorithm works like the gradient search method (steepest descent). On the other hand when the parameters are close to their optimal value, the standard Gauss-Newton method is selected (Gavin, 2016). The big downside off course lies in the fact that the algorithm can not handle bounds. Why this is a problem will be explained in section 5.2.2.

5.2.2. Bounds

By providing the estimation algorithm with constraints/bounds on the input parameters, the algorithm is forced to look for a suitable answer within these bounds. This will result in faster convergence to the desired output. The closer the a-priori initial state is to the exact true solution, the smaller the bounds can be. Concerning the spin axis and location, several bounds can easily be used under the following strict assumptions. A stable spin axis location is assumed based on the assumptions made by Kucharski et al. (2014) as well as the inertial spin period which can be bounded with a RMS of a couple of seconds around a certain value. As Envisat's rotational speed is slowly decreasing, a trend can be used to predict its spin period at a certain time. The initial quaternions however are quite hard to constrain. When these values are unconstrained, several local minima occur depending on the initial a-priori estimate. Furthermore equation 3.3 must hold satisfying the quaternion unit norm condition. Figures 5.10 and 5.11 show two such examples where several local minima have found after different initial quaternion state vector where provided. Both situations use the bounds as described in table 5.4

Table 5.4: Bounds to input variables

Az [deg]		El [deg]		ω_0 [deg/s]		q_w [-]		q_x [-]		q_y [-]		q_z [-]	
260	270	-30	-26	2.83	2.92	-1	1	-1	1	-1	1	-1	1

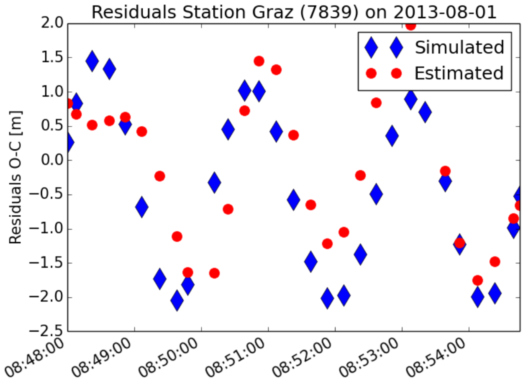

Figure 5.10: Local minimum example 1

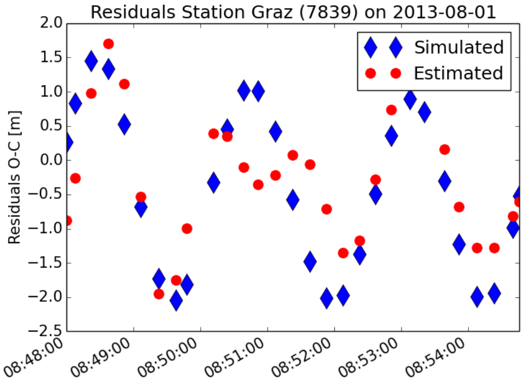

Figure 5.11: Local minimum example 2

5.2.3. Local optimization

If a certain initial condition is close enough to the true result, a local optimization algorithm could possibly suffice to provide the correct answer. A number of tests were performed to check the quality and performance of this search. Table 5.9 gives the inputs and its bounds which have been used for various simulations throughout this subsection.

Table 5.5: Bounds to input variables

	Az [deg]		El [deg]		ω_0 [deg/s]		q_w [-]		q_x [-]		q_y [-]		q_z [-]	
True conditions (Simulated):	250		-28		2.88		0.1488		0.08945		0.507		0.844	
Initial conditions:	240		-30		2.83		0.1		0.07		0.4		0.8	
Bounds:	200	300	-31	-25	2.83	2.92	-1	1	-1	1	-1	1	-1	1

Within scipy there are several local optimization tools which minimize a certain function. Several methods exist within this optimization. The two main options which support bounds or constrains on the problem are the Sequential Least Squares Programming (SLSQP) and Limited-memory Broyden-Fletcher-Goldfarb-Shanno with Bound constraints (L-BFGS-B) methods. A comparison between both methods has been made with the same conditions.

SLSQP The SLSQP algorithm is more or less similar to the Broyden–Fletcher–Goldfarb–Shanno algorithm (BFGS) method such that it evaluates a descent direction in each step and a variable step size. From 1970, this method has grown in popularity due to its ability to handle nonlinear constraints. Its fundamental idea is to model a given approximate solution using a quadratic programming sub problem which then uses this solution to construct a better approximation of the next solution. By iterating this process, a sequence of approximations is created which eventually would converge to the true solution (Boggs and Tolle, 1995).

A pass from Zimmerwald on the first of August 2013 taken from 21:43:14 till 21:51:14 is used for the upcoming evaluations. Figure 5.12 shows the evolution of all the input parameters with respect to the true solution from the simulated input.

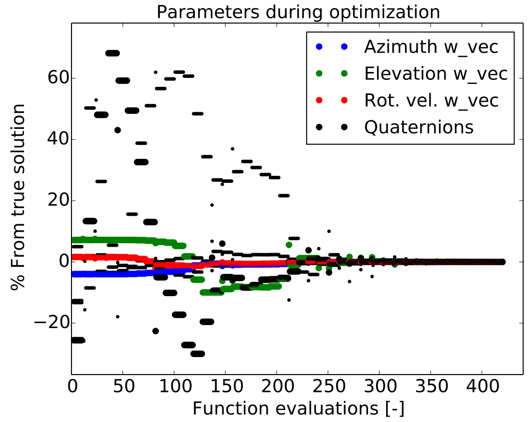

Figure 5.12: State variables SLSQP

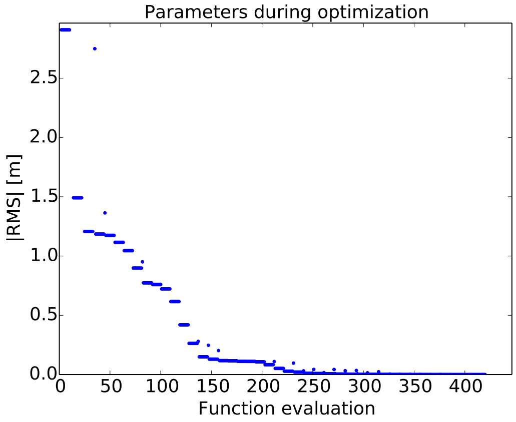

Figure 5.13: Convergence SLSQP

L-BFGS-B The L-BFGS-B method approximates the BFGS method but requires a limited amount of computer memory. Its principle is best compared to a quasi Newton optimization algorithm but uses an estimation to the inverse Hessian matrix (Dai, 2013). Instead of storing the entire Hessian matrix, the L-BFGS-B algorithm only takes a few vectors which are enough to reconstruct approximately the full Hessian (Liu and Nocedal, 1989). The L-BFGS-B method is compared against the SLSQP method with exactly the same parameters. The results are shown in the figures below.

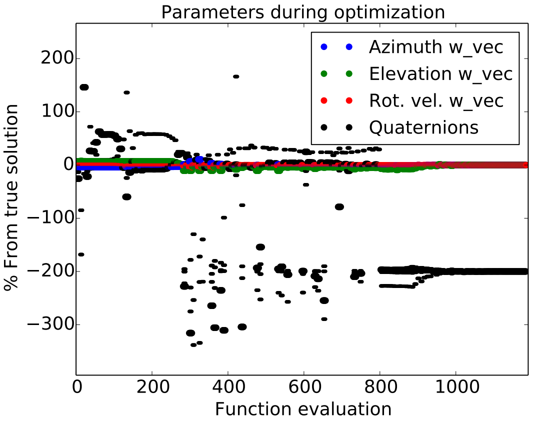

Figure 5.14: State variables L-BFGS-B

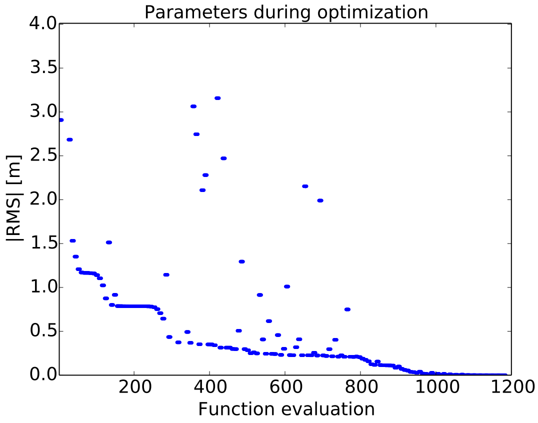

Figure 5.15: Convergence L-BFGS-B

It is clearly visible that the L-BFGS-B algorithm takes significantly longer to converge compared to the previousS SLSQP method. From figure 5.14 it is seen that the quaternions converge at a relative value of -200% of the true value. This matches the inverse quaternion which implies exactly the same rotation as the true quaternion.

Varying the initial conditions These initial guesses of the state lie rather close to the optimum. When the offset of the initial conditions are given a higher offset with respect to the true solution, the problem does not converge to the true solution, but to a local minimum. An example of a state vector which has randomly selected quaternions is given in table 5.6.

Table 5.6: Random quaternions initial state vs true attitude state

	q_w	q_x	q_y	q_z
True	0.1488	0.08945	0.507	0.844
Initial guess	0.5	0.8	0.1	-0.6

To illustrate what this looks like figures 5.16 and 5.17 are created. It is clear that the initial rotation where Envisat is put in, is totally different from the true solution. In both cases the spin axis properties remain the same.

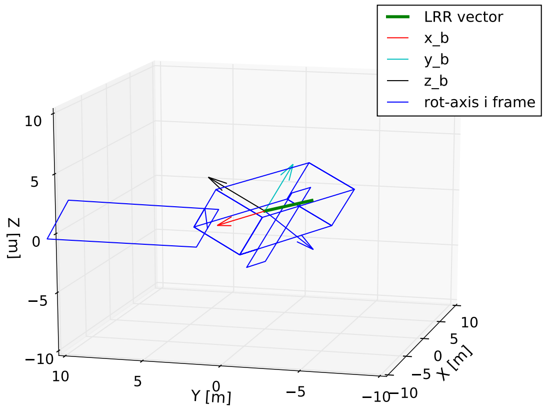

Figure 5.16: True initial attitude

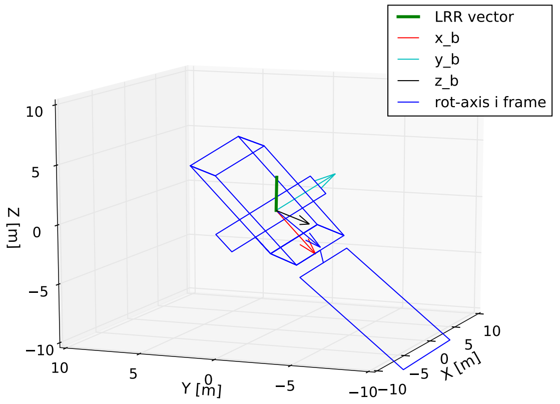

Figure 5.17: Initial attitude guess

The SLSQP algorithm is used and its results of the residuals are shown in figure 5.18 and the corresponding parameters during optimization are found in figure 5.19

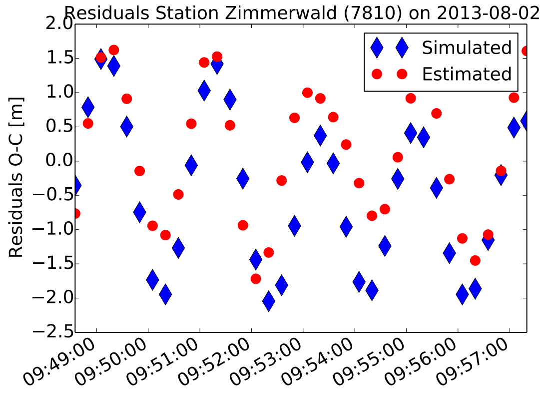

Figure 5.18: Residuals wrong quaternion offset

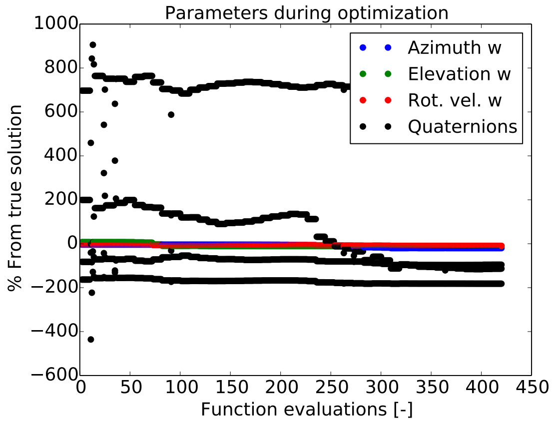

Figure 5.19: State parameters during least-squares fit

From this analysis, it can be seen that local minima occurs if the quaternion set is set too far apart from the true value. Bounds are thus crucial in a local optimization analysis. Figure 5.17 shows a position of Envisat which is actually not possible based on the skyplot analysis performed in section 4.7.2 and illustrated in figure 4.39.

This immediately results in a small next test where the initial condition lies within this assumed visibility range. If the initial orientation is set as the true initial position but rotated 90 degrees around its Z_b-axis such that it is oriented as in figure 5.20, the LRR should be in view for the selected station pass geometry. The same local optimizer is ran, and the converged residuals and parameters are shown in figures 5.21 and 5.22.

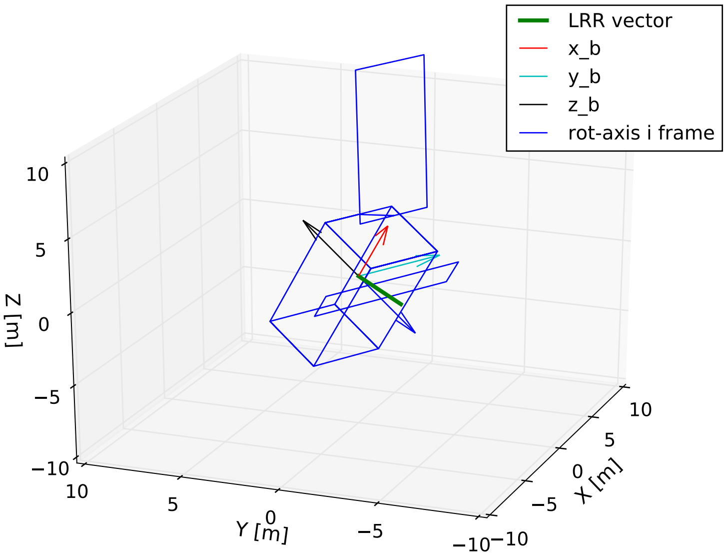

Figure 5.20: +90 degree rotation around Z_b from true initial attitude (figure 5.16)

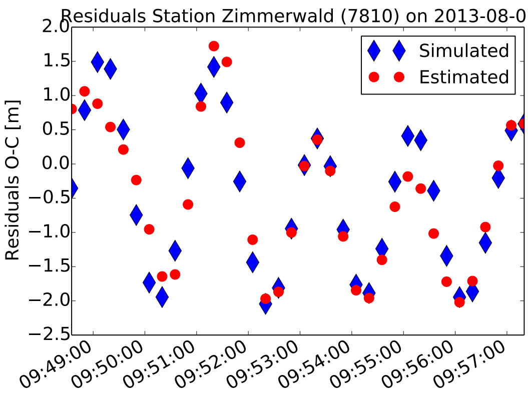

Figure 5.21: Residuals offset 90 deg

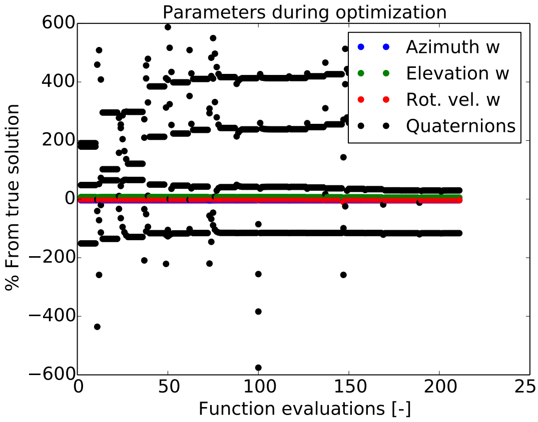

Figure 5.22: State parameters during least-squares fit with 90 degree offset

From the converged parameters one clearly sees that the solution does not resemble the true solution at all, although the residuals show a pretty good fit. This means that not only the initial plane where the LRR lies in is of importance(visibility constraints), but the total orientation should not lie too far apart from the true solution. This makes it quite hard to only estimate local passes based on no a-priori information using the proposed methods as before.

Euler Quaternion (EQ) When one assumes that the spin axis of the satellite approximately coincides with one of the principal axis, one could first try to determine the initial Euler angle around this axis, from which an estimate of the initial quaternions follows. This allows the full quaternion estimator to work with a guess which is as close as possible to the true value.
In order to demonstrate this capability, a slightly inclined new orientation is chosen with an Euler angle of 50 degrees from the true attitude(table 5.6) as given in table 5.7.

Table 5.7: Quaternions initial state where Z_b coincides with spin axis

	q_w	q_x	q_y	q_z
True	-0.22185	0.2954	0.4218	0.82796

The Euler angle itself converges relativity fast as is seen in figure 5.23. An initial guess was set at 160°.

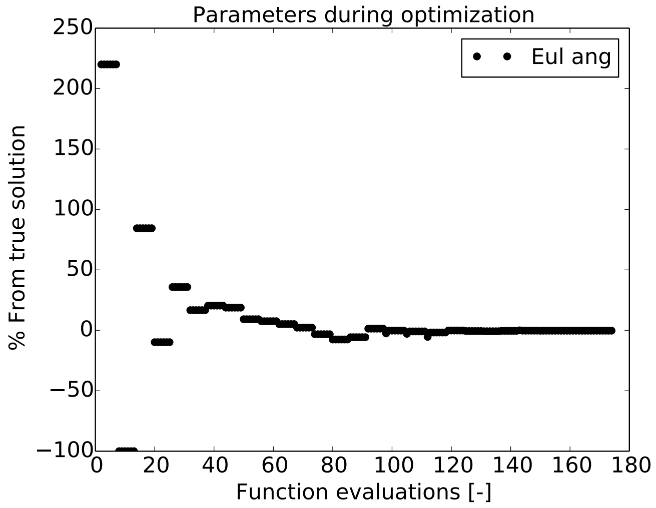

Figure 5.23: Euler angle convergence when Z_b-axis lies in the spin axis direction

The quaternions found from this iteration are that close to the true solution that an additional estimation with the quaternions as a full state vector is unnecessary. The method seems to work when the important assumption is made that the bodies z-axis coincides with the spin axis. This might not be the case as was speculated in literature before by Shakun et al. (2013). Therefore a new initial orientation is set-up which has a slight deviation of a couple of degrees between the z-body axis and the spin axis orientation which results in the following quaternion set as given in table 5.8.

Table 5.8: Quaternions initial state 3 with small precession

	q_w	q_x	q_y	q_z
True	-0.228236	0.27047	0.38627	0.851789

The Euler angles converges to a stable value after about the same number of iterations as in figure 5.23. The resulting parameters from this first guess are however slightly different than the true solution. This is expected due to the induced precession in this model, whereas the first part of the EQ-method assumes a stable spin axis. It however does have the rotational vector as an input state vector for which it tries to compensate the induced precession by varying the azimuth, elevation and speed of the rotation axis, which could result in a lower total residual value, but slightly shifts the corresponding correct Euler angle as well, therefore careful consideration of these bounds must be given. The first part of the EQ-method only involves a simple Euler rotation around the spin axis, assuming that the spin axis coincides with the z-axis(or another chosen principal axis). The full quaternion evaluation however requires quite a lot more iterations due to this more sophisticated rotation and three more parameters (7 in stead of 4). The results are given in figures 5.24 and 5.25.

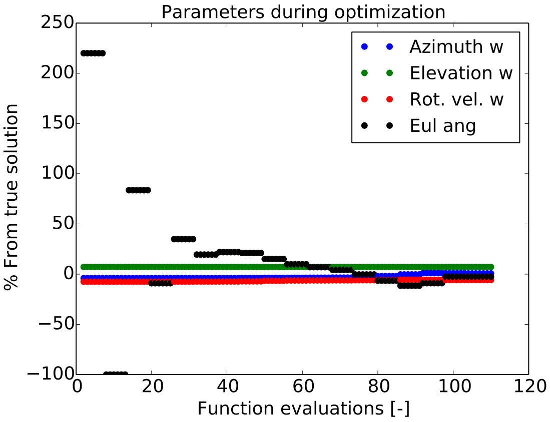

Figure 5.24: Results after the first estimation scheme with the simplified model

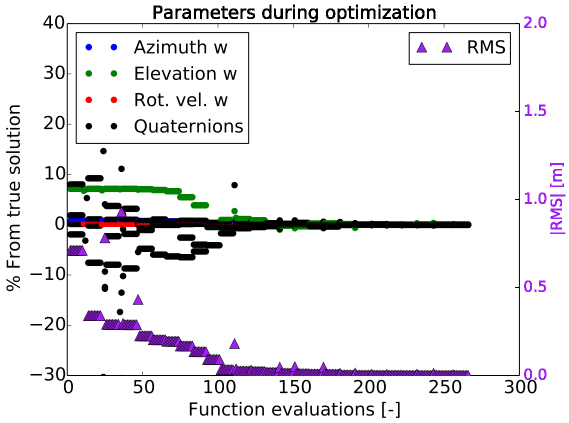

Figure 5.25: Results after the second estimation scheme with the full quaternions as input

This new method shows good performance even with a slight precession in the spin axes. In the remaining thesis, this method will therefore be addressed as the EQ method.

5.2.4. Length of pass

A common assumption is one where the the total pass length needs to be at least one revolution in order to process enough rotational behaviour. This section will investigate this assumption. A simple test has been created for a single local station pass of Hartebeesthoek on the first of august 2013. In a theoretical case based on the station-viewing assumptions, Envisat should be visible for about seven minutes. However in practice, the practical viewing time could be quite shorter than what is theoretical possible. In order to asses the use of shorter residual arcs, the number of normal points being used in the estimation scheme is reduced to only 7 NP's instead of the original 30 NP's. In all cases, the same initial guess of the SLSQP local optimization algorithm is used which is given in table 5.9. The results are given in figures 5.26-5.29.

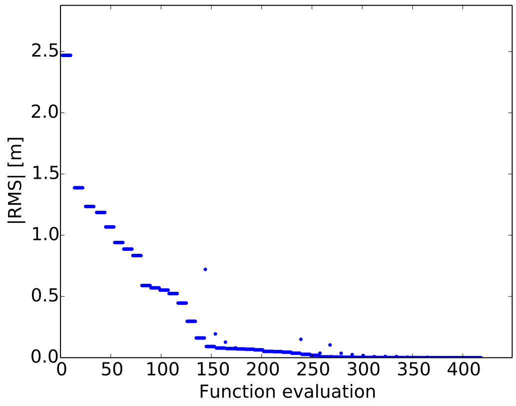

Figure 5.26: SLSQP performance all 30 NP's

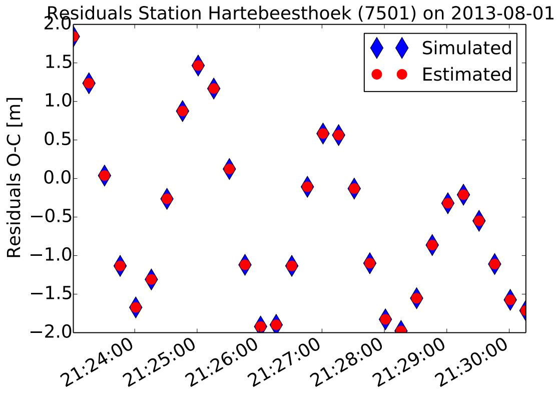

Figure 5.27: Corresponding residuals all 30 NP's

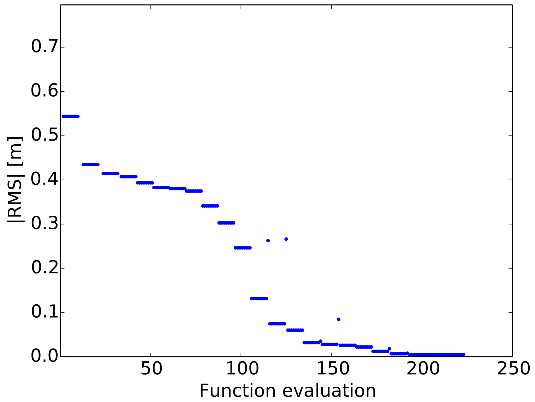

Figure 5.28: SLSQP performance 7 NP's

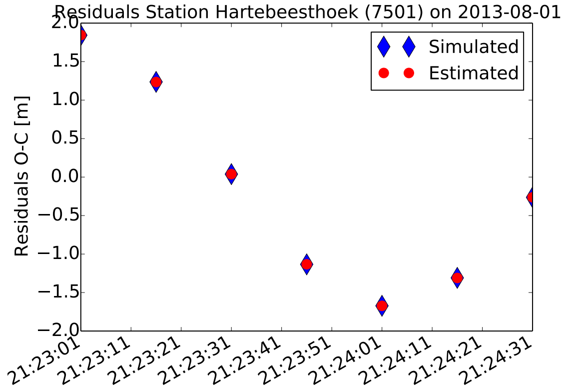

Figure 5.29: Corresponding residuals 7 NP

This test shows that indeed a solution is found in both cases. But when comparing the converged solutions it becomes clear that the reduced number of NP's does not converge to the true solution as is seen in the parameters which are plotted for each function evaluation in figures 5.30 and 5.31. This is one of the reasons why using simulated data to validate the outcome in this thesis is of importance.

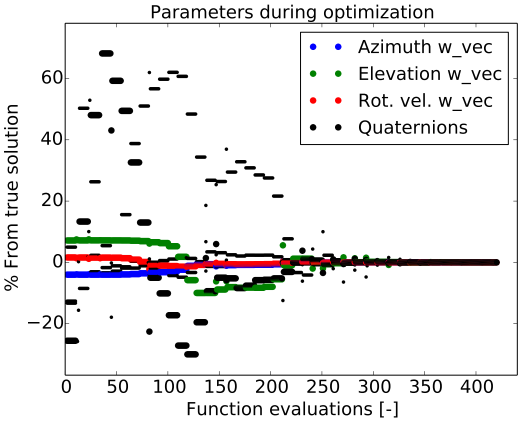

Figure 5.30: Parameters during optimization for all 30 NP's

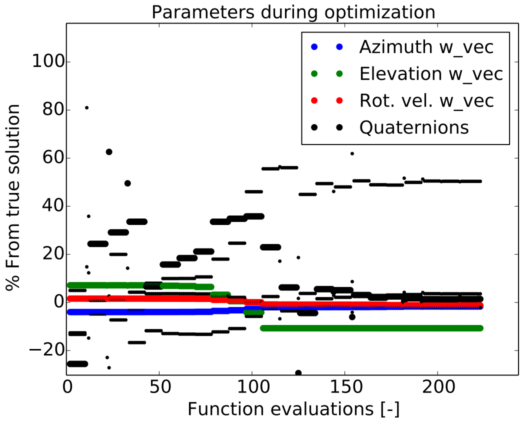

Figure 5.31: Parameters during optimization for 7 NP's

The question arises what a minimum number of normal points would be in order to have a true successful convergence. One would think that at least one revolution is enough to determine the exact solution. So in the upcoming case, ten normal points are selected covering about 150 seconds of data which is 25 seconds longer than one revolution of 125 seconds. The convergence results of all parameters are shown in figure 5.32 next to its corresponding matched residuals in figure 5.33.

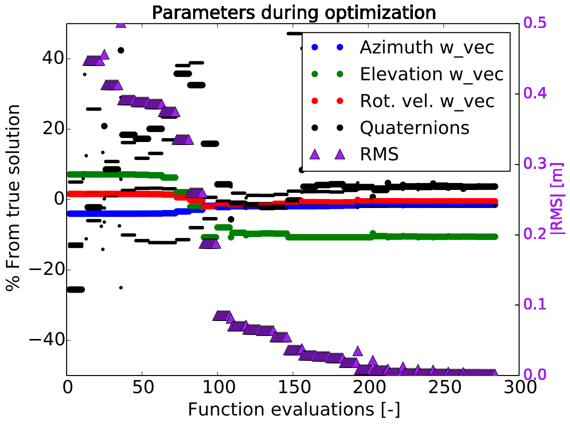

Figure 5.32: Parameters during optimization for one revolution

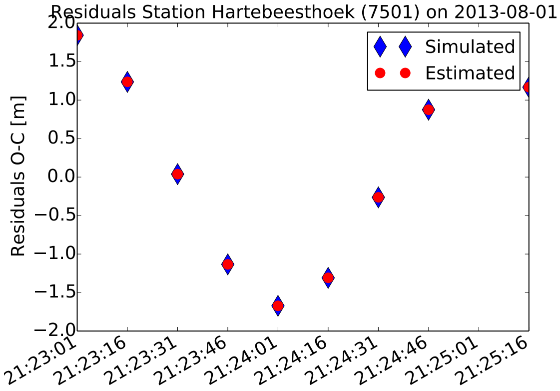

Figure 5.33: Corresponding residuals for one rotation

Even one rotation does not give enough guarantee for a correct convergence of the full rotational set as can be seen in figure 5.32. This is interesting as Envisat mainly posses small data sets. By varying the maximum amount of normal points in a pass, until the solution converges to about 1% of the true solution, a minimum number of normal points of 17 is found which corresponds to about two rotations which can be seen in figures 5.34 and 5.35.

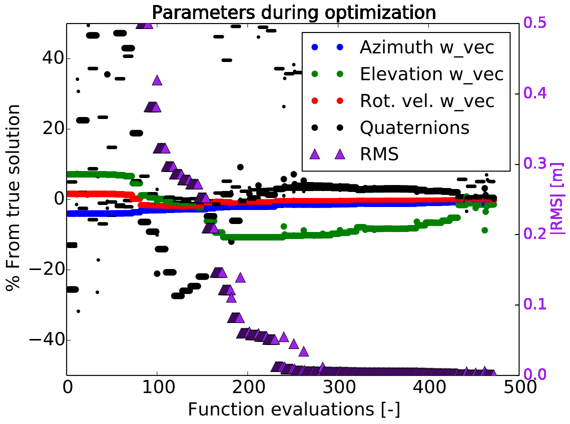

Figure 5.34: Parameters during optimization for 2 revolutions

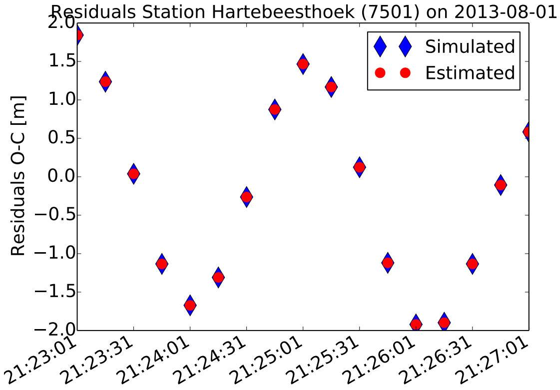

Figure 5.35: Corresponding residuals for 2 rotations

A similar analysis has been performed for a pass from Zimmerwald, again here the SLSQP optimization only succeeds (convergence within 1%) after a minimum of two revolutions. This might be a problem with real Envisat data, as most passes are not that long, as was shown in section 4.6.

The Nyquist-Shannon sampling theorem This theorem sets a specific condition on a sample rate that allows a discrete sequence of samples to capture all information from a continuous-time signal. The sampling frequency should be at least twice the highest frequency contained in a signal in order to avoid aliasing (see figure 5.36), which although matches the specific sampled points, does not produce the same signal. Thus if Envisat is spinning at a period of 130 seconds (0.0076 Hz) and this is regarded the highest frequency in the residual signal, the normal point distribution of 15 seconds (0.06 Hz) lies well above the minimum of 0.015 Hz (66 seconds) required. For a perfect sine wave this might be true, however, larger frequencies do exist in the residual signal as well(around 0.06 Hz), as was shown in section 4.7.1. This implies that using higher rate data could result in better estimates. One could use the higher rate full-rate data, but the amount of data is quite limited.

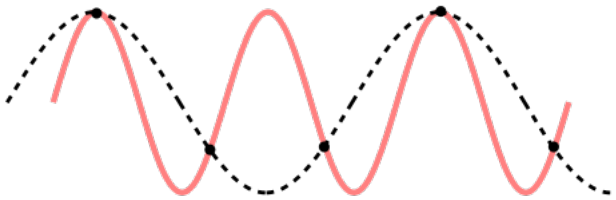

Figure 5.36: Aliasing problem, sample frequency is lower than twice the main frequency, which results in a wrong estimated signal

Initial conditions Whether or not a better initial condition could influence the converged result is still unknown. From figures 5.32 and 5.34, it is clear that the elevation angle of the rotational vector poses the largest offset from the true solution in the last iteration. Bringing the initial condition of the elevation angle pretty close to the true solution has unfortunately no significant effect on the convergence. Even when lowering all initial conditions to a value pretty close to the true solution(see table 5.9), the local estimation procedure does not produce good enough results which is shown in figure 5.37.

Table 5.9: Bounds to input variables 2

	Az [deg]		El [deg]		ω_0 [deg/s]		q_w [-]		q_x [-]		q_y [-]		q_z [-]	
Initial conditions(sim):	250		-28		2.88		0.1488		0.08945		0.507		0.844	
Initial conditions(estem):	249		-28.5		2.87		0.14		0.089		0.50		0.84	
Bounds:	200	300	-31	-25	2.83	2.92	-1	1	-1	1	-1	1	-1	1

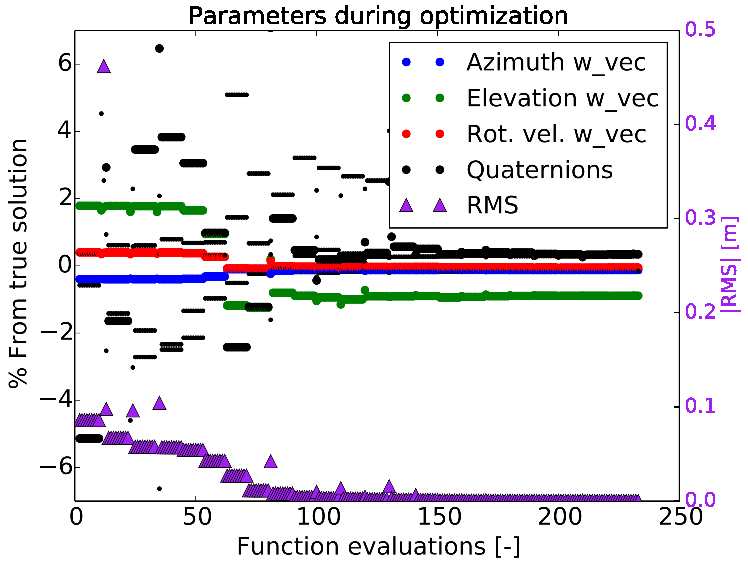

Figure 5.37: 1 revolution better initial conditions Hartebeestehoek

Even if the initial guess is very close to the true solution the solution does not converge locally to the correct answer if time arcs below 2 periods are chosen.

EQ method As was mentioned before, a different local optimization method may be used as well under the assumption that Envisat is rotating around one of its principal axes. Now this method is evaluated in terms of minimum length needed. As a sample, the following rotational inputs(table 5.10) are used from a pass from Graz on the 5th of August 2013 covering a total of 39 normal points.

Table 5.10: EQ pass length evaluation initial parameters

	Az[deg]	El [deg]	period [s]	q_w[-]	q_x [-]	q_y [-]	q_z [-]
Input	270	-28	129	-0.338	0.2527	0.542	0.726
Initial estimate	250	-45	130	-	-	-	-

By varying the amount of normal points in this pass the convergence performance is analysed. The results are given in table 5.11.

Table 5.11: Unbounded length of pass evaluation results

Number of NP's	Convergence?	Function evaluations	f_{final} [m]
39	Yes	1000	0.0007
30	Yes	1100	0.0008
25	Yes	800	0.0006
22	Yes	1200	0.004
20	No	440	0.6

During the Euler angle approximation phase, the elevation angle seems to shift up to a positive value when the number of normal points is decreased, causing the solution in the second phase not to converge to the true solution. The first phase does show smaller residuals for higher elevations angles, but can be discarded due to the assumed semi-fixed orientation in the l-frame (based on the station pass analysis in figure 4.39). By imposing bounds(-90° to -20 °) to the elevation angle in the first phase this problem is solved and the solution even converges with 20 normal points as is presented in table 5.12.

Table 5.12: With bound on elevation

Number of NP's	Convergence?	Function evaluations	f_{final} [m]
20	Yes	700	0.0004
15	Yes	650	0.004

From 15 normal points(slightly bigger than one revolution) the solution shows increasing errors from the true solution which are still within certain limits of the true solution. The convergence results are shown in figures 5.38 and 5.39.

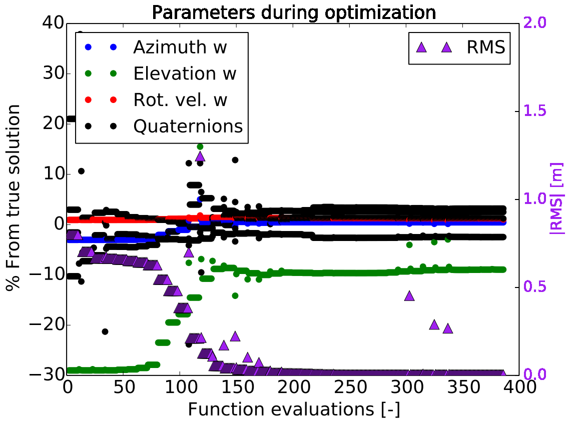

Figure 5.38: Parameters during optimization for 15 NP's

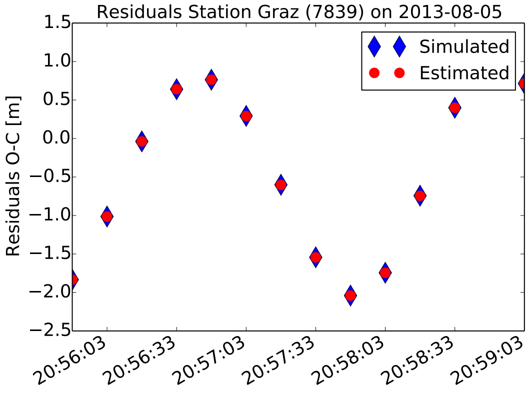

Figure 5.39: Corresponding residuals for 15 NP's

5.2.5. Global optimization algorithms

This section will discuss the used algorithms in order to find the best solution and asses its performance. Two global optimization algorithms are included in the scipy package of python. These are differential evolution and basinhopping. This section will test and evaluate both methods.

Differential evolution This algorithm is implemented using the scipy package. This stochastic method is based on the work of Storn (Storn and Price, 1997). Instead of relying on gradient search (steepest descent methods), the differential evolution method mutates each candidate solution with other solutions in order to create trial candidates from which it selects the best and continues with these candidates. This is an improved genetic algorithm. The differential evolution algorithm uses a L-BFGS-B method to polish the best population member at the end which gives an even higher accuracy. As a method the "best1bin" option was selected, which selects two members of the population randomly and their difference is then used to mutate the best member using a binomial crossover and only taking into account one pair.

The best1bin resulted in a found optimum at a lowest function value of 0.32 m and corresponding initial euler angles of 89.63°, -21.7° and 166° in yaw, pitch and roll respectively, which is not the desired true solution ($Eul_{true} = [180, 0, 62]°$ in yaw, pitch and roll). Therefore a larger population size and lower tolerance criteria should be evaluated, next to allowing multiple iterations.

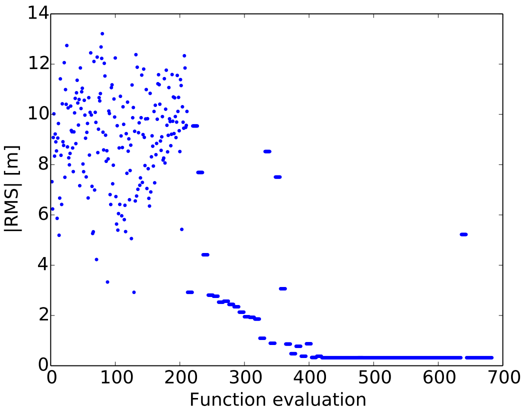

Figure 5.40: RMS of each function evaluation

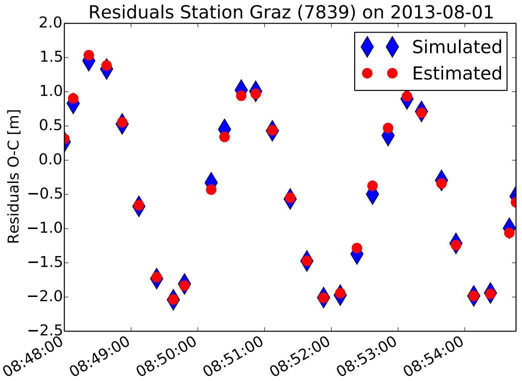

Figure 5.41: Corresponding residuals

Another pitfall of the algorithm is that it tends to go to the initial attitude Euler state corresponding to [-180,0,62]° in yaw pitch and roll respectively in stead of [180,0,62]° which is the true global optimum. Figure 5.42 shows the results of the "best2bin" method in terms of convergence for a population size of 15, maximum iterations of 10 and a tolerance criteria of 0.01.

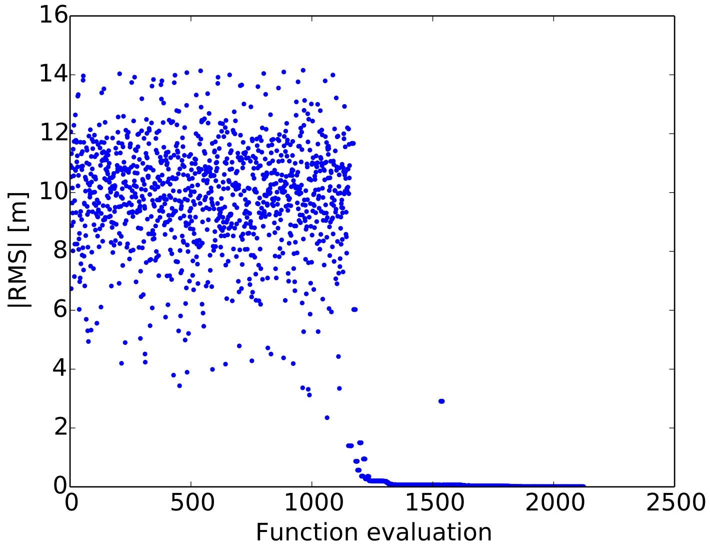

Figure 5.42: "best2bin" method

The differential evolution method shows a large sparse area after which, all local minima found are evaluated for their true global minima. This initial sparse area is defined by the user's input parameters population size and maximum iterations. The population has a total size of the input parameter multiplied with the number of arguments (8). Mallipeddi and Suganthan (2008) mention that the success of a differential algorithm depends on the correct use of the population size. Choosing a too small population could result in fast convergence but with the risk of stagnation. That is, if the population remains diverse, but it looses it diversity and won't progress any more resulting in a case like in figure 5.41. When comparing all methods with the options, the "rand2bin" strategy (where not the best, but a random member is mutated) seems to convergence to its optimum in the smallest amount of function evaluations. All options converge to nearly the true optimum.

Concluding it can be seen that the method has some drawbacks in terms of speed and accuracy.

Basinhopping algorithm Unlike the differential evolution algorithm, the basinhopping algorithm implemented in scipy is a non-population based method (Wales, 2003). Just like in the differential evolution case, a L-BFGS-B method is used. This algorithm shows that it must evaluate all local minima before drawing conclusions regarding a global result. Due to the random selection of a set of parameters this method is quite slow. This results in a large number of iterations before the optimum is found, as can be seen in figure 5.43. There are about 9-10 different local optima that have RMS values under 1 m, which lie pretty close too each other.

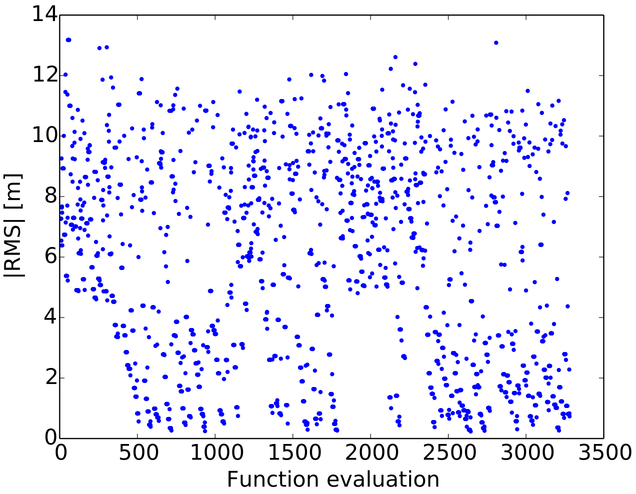

Figure 5.43: Basinhopping algorithm

The corresponding attitude parameters of these minima needs investigation. A possible scenario could be that the baisnhopping algorithm always finds the same/similar local minima. Another could be that a certain symmetry with respect to the true solution creates more or less similar convergence function values. Two cases are examined. One with a 0.2 standard deviation bound on the quaternions, and one with no bounds. Both cases are evaluated for the same number of iterations and starting from an initial guess of quaternions which is chosen arbitrary (q=[0.1,0.1,0.1,0.1]). The results can be seen in figure 5.44 and 5.45. A tolerance criterion of 0.01 is used in the algorithm which only accepts minima which lie under a total RMS of 0.01.

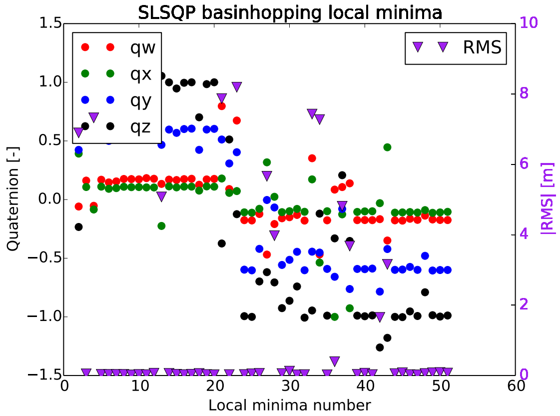

Figure 5.44: All local minima found with no constraints on quaternions with a wrong initial guess of the quaternions

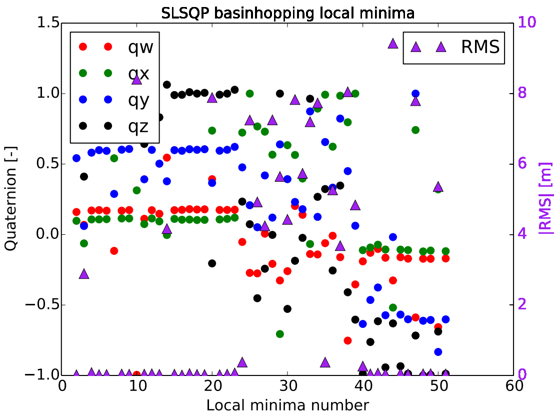

Figure 5.45: All local minima found with no constraints on quaternions with a correct initial guess of the quaternions

It is clearly visible that the quaternion parameters lie pretty close to each other and that the algorithm tries to obtain a better result each iteration. There exists however another optimum where the algorithm takes quite some iterations as well. This is located at exactly the inverse of a quaternion set (q and -q). This is due to the fact that no constraint is put on the quaternions such that it allows to divert to exactly the opposite. A unique rotation is defined by a pair of opposite (antipodal) unit quaternions. This figure shows it is save to conclude, that only one exact global optimum exists, which can be seen in the RMS values. Only for one particular set of parameters, a total RMS value below a certain threshold exists. It is not necessary due to the initial guess that these figures are produced like they are shown above. Some runs, the algorithm would only show the opposite solution (-q) and some times only the positive solution (q). Sometimes it shows both as is illustrated in figure 5.44. Fact is that having an initial guess as close as possible to the correct solutions does not affect the performance.

A function tolerance criteria of 0.01 shows a clear convergence to the suitable answer. Increasing this number allows a lot more local minima to be accepted by the algorithm which is shown in figures 5.46 and 5.47.

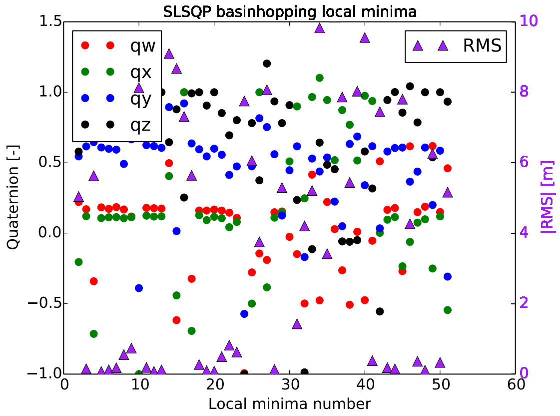

Figure 5.46: ftol=0.05

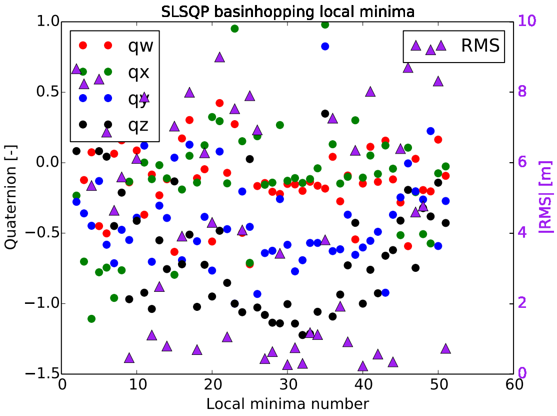

Figure 5.47: ftol=0.1

Although these minima do not approach the true solution, their resemblance is quite significant. On this point there is no direct relation between a local minima and the true solution. It would be useful for later analysis if one knows how far these local minima lie from each other.

5.2.6. Evaluating bound ranges

The EQ method is selected as the estimation method for a local minima search. This section will show the allowable bounds wherein the initial conditions must be set in order for the local optimization method to succeed. The results of this test are presented in table 5.13. The rotational velocity expressed as the period (P) is always constraint at a standard deviation (σ) of 20 s. For each run, either the azimuth or the elevation angle (or none) of the spin axis is constraint.

Table 5.13: Values from which the solution diverges to another local minimum

Situation	Test run	Constraints	Δ Azim [°]	Δ Elev [°]
A	1	Az σ = 20° + P σ=20 s	-	± 140
A	2	El σ 20° + P σ=20 s	± 160	-
A	3	P σ=20 s	None	None
B	4	Az σ = 20° + P $\sigma 20s$	-	±110
B	5	El σ 0.20° + P σ=20 s	±120	-
B	6	P σ=20 s	See down	See down

In this table the ΔAzim and Δ Elev show the deviations of the azimuth and elevation angle of the spin axis from the true solution from which the local EQ method starts to divert to another local minimum. Table 5.14 briefly summarizes both situations A and B.

Table 5.14: Situations from 5.13 explained

Situation	Explanation
A	Rotation around principal Z_b axis with Az=270°, El=28°
B	Rotation around principal Z_b axis with induced precession (Roll+0.5 [rad])

If one element of the spin axis is constraint (test runs 1,2,4,5) and the others are not, this might result in local minima that are not the true solution. These margins are however quite large. When precession is added (situation B), these margins tend to decrease.

When no constraints are set on spin axis location in case when the spin axis is aligned with the principal Z_b axis, the solution always converges to the true result as is seen in test run 3. This appears due to the fact that a pair of different azimuth and elevation combinations exist which result in the same solution. That is, at Az-180° and 180°-El, the same solution is found as when the original azimuth and elevation angles of the spin axis were to be used. Situation B, where precession in the spin axis is added shows slightly more sensitive results for constraints on azimuth and elevation of the spin axis. Furthermore the Euler angle step converges first in the most extreme situation, after which the full quaternion step takes over and fits the exact attitude information. This results in a higher number of steps required in order to converge. Test run 6 with situation B showed that constraints are necessary as the solution resulted in several local minima which are not the true solution but the inverse of the spin axis. Although the residuals seem to fit quite well for this inverse(in the counter direction of the original axis), the total RMS of the residuals show slightly higher values (about 2 m). Furthermore the rotational speed converges to its minimum constraint. This situation is new and is only found when precession is added to the spin axis.

5.3. Multiple stations

This section will show the attitude determination for multiple stations passes. Just like in the estimation scheme of orbit determination, the problem becomes better constraint when multiple unique passes or more data is available. Instead of estimating the attitude of only one pass at a time, another method will be investigated. That is by looking at the residuals of an entire batch of passes. First a case with a relatively short arc will be presented for demonstration purposes, then a longer arc will be evaluated.

5.3.1. Short arc-demonstration

As mentioned in section 5.1.2, the number of stations which are in view can manually be adapted. As a first demonstration test, a single arc on the 1st of August 2013 was selected over Western-Europe around 21:40. In this pass, Three stations (Wetzell, Zimmerwald and Graz) are theoretically in view of Envisat. These stations should thus be capable of tracking Envisat based on the assumptions mentioned in section 5.1.2. The station-satellite pass geometry is illustrated in figure 5.48 using STK. Table 5.15 gives the assumed start and stop contact times of each station's pass. The residuals of this short-arc demonstration set-up are shown in figure 5.49.

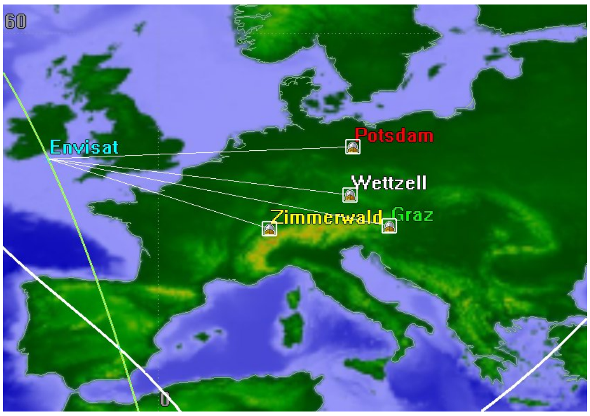

Figure 5.48: Short arc demonstration (STK)

Table 5.15: Short arc stations and their appropriate start stop times

Station name	Station ID	Start time	Stop time
Zimmerwald	7810	21:43:14	21:52:14
Graz	7839	21:44:24	21:50:54
Wetttzell	8834	21:44:31	21:52:01
Potsdam	7841	21:45:28	21:52:58

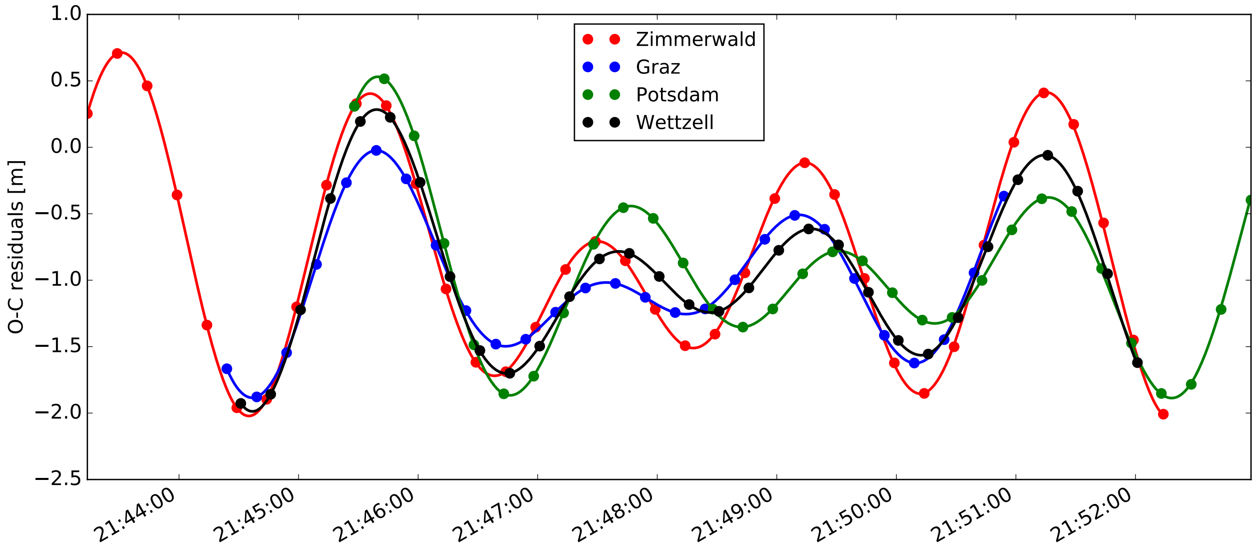

Figure 5.49: Short arc residuals corresponding to table 5.15

The start and stop times are filled with a pass arc at a 15 second interval, just like the normal points would be separated. First, each specific station-satellite geometry vector is calculated after which it can be converted to the laser ranging residuals using the quaternions from the total arc.

The optimization output is the sum of all differences between the simulated and true residuals of all passes. When the same initial conditions are used, just like in section 5.2.3, and the assumption that the initial quaternions are known with a standard deviation of 0.2, figure 5.51 is found. It is compared to a single pass convergence figure 5.50 where only Zimmerwald is considered. The RMS shows the total difference of all individual passes added up. This means a higher initial RMS (about 4 times as big) is found when comparing figures 5.50 with figure 5.51. It can be seen that the multi-station case converges to the about the same minimum RMS value of about 0.004 in the same amount of function evaluations.

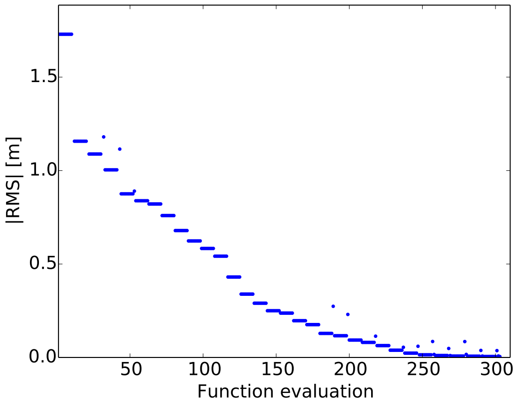

Figure 5.50: Only one station (Zimmerwald)

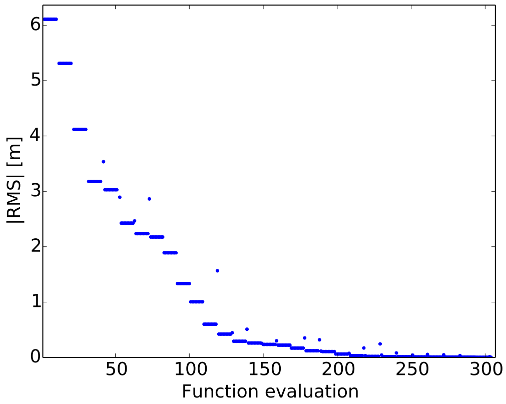

Figure 5.51: 4 station case

No propagation between several passes is needed for this set-up. All passes overlap with each other. Furthermore, the station-satellite geometry in terms of latitude longitude is similar making this set-up actually just an extended single pass. In terms of performance, there is no significant increase in convergence.

5.3.2. Short-arc multi geometry demonstration

Off course the short arc demonstration shows almost the same orbit-station geometry. Therefore still local minima exist. Not only is the arc short, but the stations lie relatively close to each other. When considering a pass where the stations have slightly different unique geometries with respect to the satellite, this could result in a unique problem solving situation. A sketch off this pass is given in figure 5.52 and the corresponding start stop times are given in table 5.16. The resulting simulated residuals are illustrated in figure 5.53.

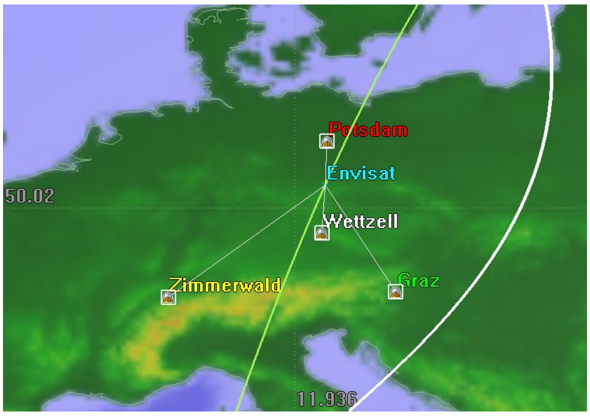

Figure 5.52: Multi geometry case (STK)

Table 5.16: Setup at 2013/08/02 multi-geom case

Station name	Station ID	Start time	Stop time
Potsdam	7841	9:48:09	9:55:09
Zimmerwald	7810	9:48:35	9:57:35
Wettzell	8834	9:49:25	9:55:40
Graz	7839	9:51:04	9:54:49

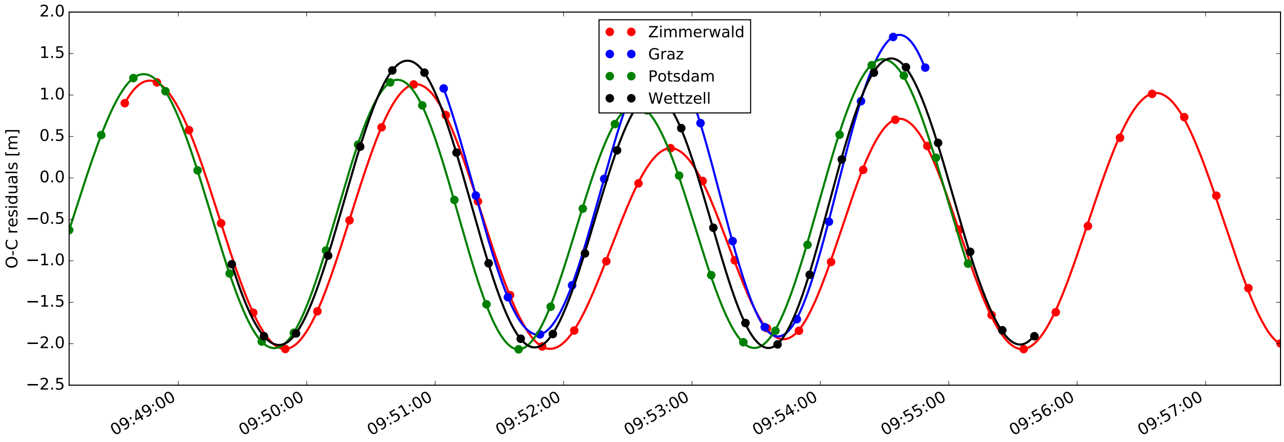

Figure 5.53: Multi geometry simulated residuals

When comparing figure 5.53 with the similar station-satellite geometries in figure 5.49 it seems the residuals are still in phase. The convergence off all parameters is illustrated in figure 5.54. The same initial conditions have been used as in the similar station-satellite geometry case.

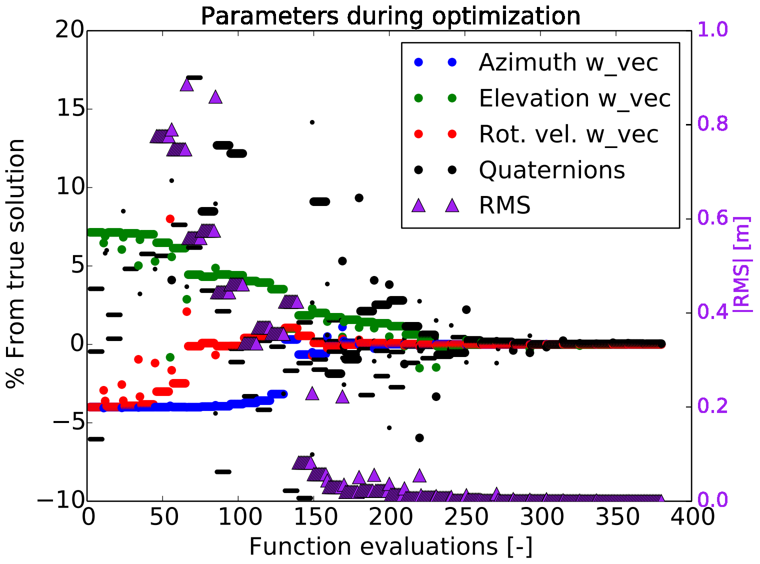

Figure 5.54: Multi geometry convergence parameters

There is clearly no decrease in the number of function evaluations when compared to figure 5.51 where the same geometry is used rather than multiple different ones as in this analysis. The stations still lie pretty close to each other as the viewing condition of Envisat does not allow further separation between the normal and anti-normal side of its l-frame orbit.

Using multiple station-satellite geometries does not necessary change the different residual signals severely compared to station passes from one particular side of the l-frame. The signals remain to be in phase. This results again in a similar longer residual arc, which does not show to improve the local estimation if the initial conditions have been set farther from their true value.

5.3.3. Medium long arc

The following station set-up is used on the first of August 2013. Its goal is to evaluate the performance of a medium long-term propagation of about 22 minutes between both passes. The selected stations are presented in table 5.17 and illustrated in figure 5.55.

Table 5.17: Station selection medium arc

Station name	Station ID	Start time	Stop time
Potsdam	7841	21:45:28	21:52:58
Hartebeesthoek	7501	21:23:01	21:30:16

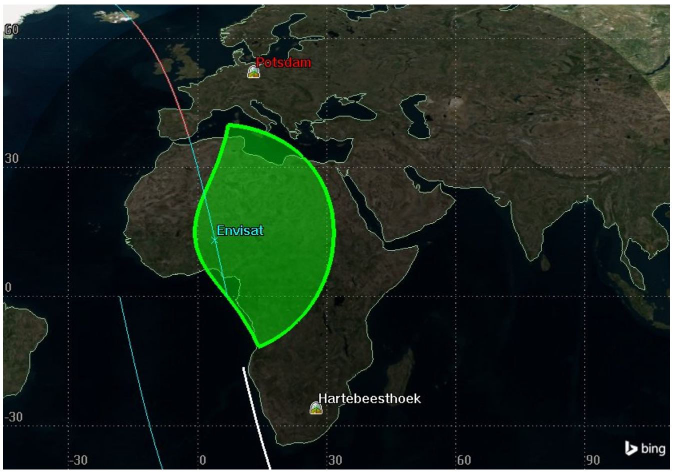

Figure 5.55: Medium arc Potsdam–Hartebeesthoek (STK)

This setup investigates the estimation performance when one needs to propagate a certain pass till the next one. In order to asses a feasible long term propagation and its performance, a suitable step size must be chosen. As was already mentioned in section 3.2.3 the longer the propagation time, the higher the error with a bigger step size. When considering a 22 minute propagation time, a 15 second step size would result in a quaternion error of about 0.02 whereas 10 seconds results in a relative error of 0.003 while increasing the CPU time with 25 % (based on the assumed initial attitude and rotational state mentioned in section 3.2.3). For this small example a step size of 10 seconds is used. The result is given in figure 5.56.

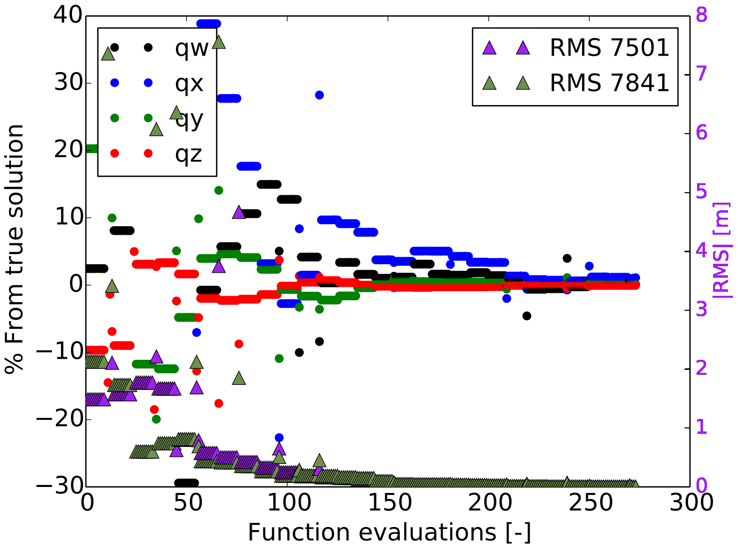

Figure 5.56: RMS and quaternions for medium arc

Figure 5.56 shows the RMS values of both stations. During the first few iterations, the SLSQP algorithm makes a few steps where the RMS of both stations clearly make contradictory moves. Where the RMS solution of station Hartebeestehoek (7501) becomes smaller, this is not necessary a solution for station Potsdam (7841). The algorithm takes the norm of both solutions in order to solve for a local minimum. This method shows converges well within less evaluations than a single arc. Therefore making it a stronger convergence problem. The computational time on the other hand is increased.

5.3.4. Long-arc

This setup will show the performance of the attitude estimation for a longer data set. 24 hours of attitude data is simulated from 2013/08/01 till 2013/08/02 for 17 stations. The main disadvantage of using a long-arc attitude estimation is the computational time it takes. As shown in section 3.2.3, a 24 h attitude propagation of a single set of initial conditions with a step size of one second takes about a minute. When about 200 iterations are necessary (if the initial state is close to the true attitude), this would require about 200 minutes op CPU time. Due to the large rotational velocity of Envisat, a step size of one second is not sufficient for long-term propagation. A step size of 0.01 second would eventually require about 13 days for 200 iterations. For the scope of this thesis, this options has not been considered. Therefore another method has been chosen.

First it must be assumed that the initial attitude and rotational state of the first pass is known and correct. This will be the starting point. From there, all passes need to be evaluated chronologically in order of appearance. An algorithm has been developed which searches for a local minimum, provided that the initial conditions are close enough too its optimum. When a suitable local minimum has been found at pass n, the next initial condition of pass n+1 can be derived by propagating the state vector from pass n till the first normal point of pass n+1. This process is repeated over time. A sketch of this process is illustrated in figure 5.57.

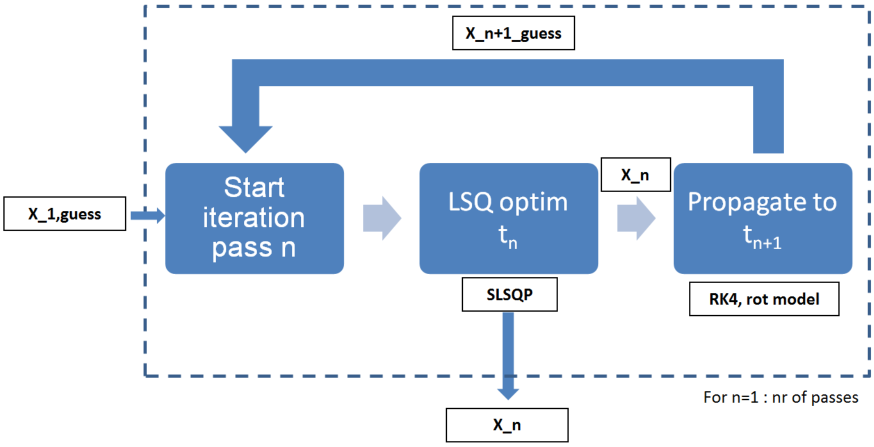

Figure 5.57: Blokdiagram of long term attitude determination

Figure 5.58 shows the convergence function results for the first six passes considered on the first of August 2013. The last station in figure 5.58 (Baikonur(1887)), clearly shows a problem. After the 5th station pass the errors increase significantly. This increase is already visible when looking at the lowest possible convergence numbers. This threshold is increasing over time as well (which is shown in figure 5.59). The reason for this lies in the long term propagation. The simulator propagated 24 hours of simulated data starting from one initial attitude state. As was mentioned in section 3.2.3 the RK4 propagator becomes unstable depending on its step size after about 4 hours (for a step size of 1 second). The produced residuals do not resemble a true simulated state but induce large errors. From a certain point these error become significantly large and the estimation algorithm fails as can be seen. The produced simulated residuals are not correct, due to a 24 hour propagation time.

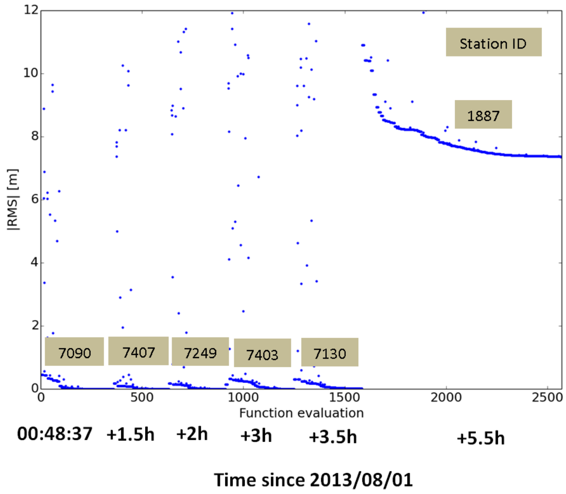

Figure 5.58: Long arc propagation example

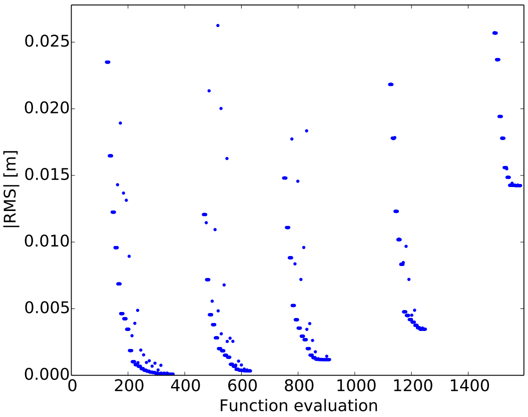

Figure 5.59: Long arc propagation example zoomed

In order to overcome this problem, more accurate propagation is needed. By having a look at the inertia tensor, a significant decrease in error was noticed. The previous analysis was performed using the full inertia tensor rotating the spacecraft around it's Z_b-axis, which is clearly not the principal axis. The RK4 integrator can also be provided with the principal axis only as is discussed in section 3.2.3. The same stations are evaluated as in figure 5.58, but only with the principal axes. The result is illustrated in figure 5.60.

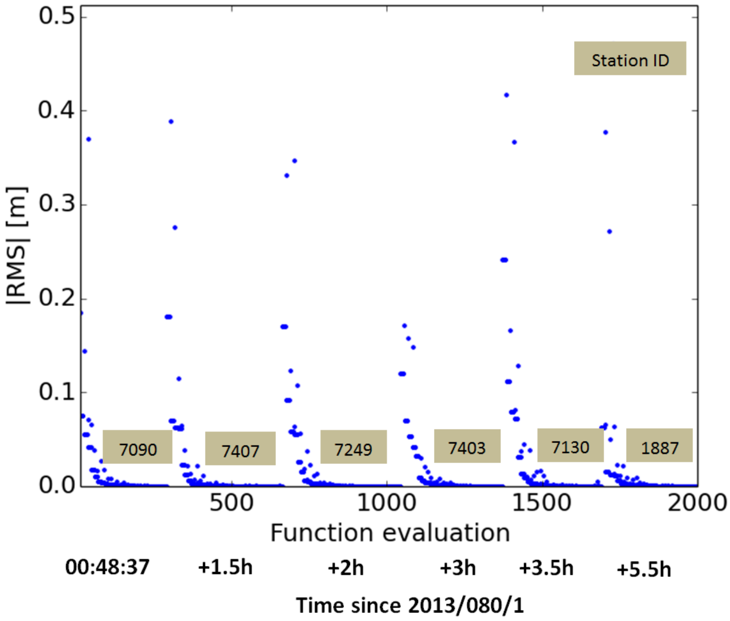

Figure 5.60: Long arc prop example with principal axes only

It is clearly seen that the estimation process does not fail any more after 5 hours which was the previous case when considering the full inertia tensor. Furthermore the accuracy is below a convergence RMS of 0.00005 m for all passes. This is a nice step, but then again when compared to reality, Envisat is tracked only a couple of times a day, so the estimation algorithm should also work for longer periods of gaps between two passes. This has been tested for the principal-axes propagation system. A propagation is evaluated from Yarragadee to Arequipa which lies about 13 hours from each other as can be seen in table 5.18.

The result is shown in figure 5.61. It is clearly visible despite the small stepsize of one second that a longer propagation induces some errors in the initial state. This increased initial state error is however well within the allowable bounds for the SLSQP local optimization algorithm in order to succeed.

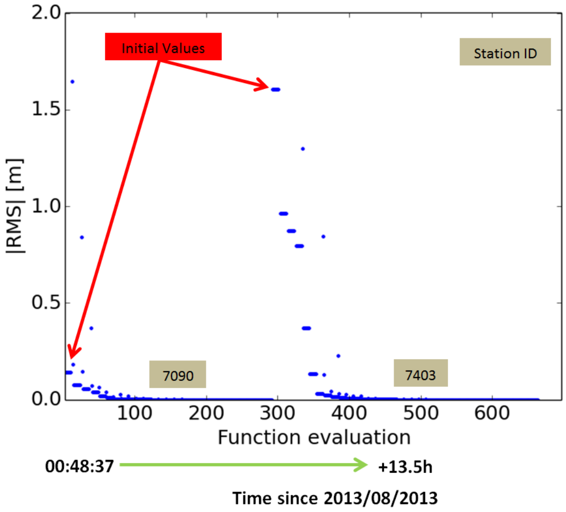

Figure 5.61: Very long propagation performance

Table 5.18: Long arc example propagation

Station name	Station ID	Start time	Stop time
Yarragadee	7090	00:48:37	00:54:37
Arequipa	7403	14:04:21	14:13:36

5.4. Conclusions simulations

Based on the assessed simulations and test cases the following conclusion can be drawn. First a minimum of two revolutions is necessary in the residual signal in order to estimate the corresponding attitude state. This holds when local optimization is considered. Next, a method has been developed called the Euler Quaternion (EQ) method which first rotates around an assumed spin axis which coincides with a principal axis, in order to find a suitable initial quaternion set, after which in the second phase the full quaternion state is derived. This method can only be used when the spin axis is assumed to be in the direction of a principal axis. When the spin axis wobbles(precesses) around the principal axis with a few degrees, the EQ method is still able to find the full quaternion set.

Multiple station passes can also be combined in the attitude determination process. Three different cases were assumed. First a simultaneous tracking case was analysed. Here a distinction between the same station-satellite geometry and different station-satellite geometries was made. For both cases, the fitting of the residuals happens simultaneously. The same geometry does not converge any faster than a single pass. The total residual set just becomes longer. A multi-geometry case has been assessed as well. It shows no clear evidence of converging better or faster than a single arc. The produced residuals show to be in-phase with each other for both cases.

The second tracking case shows the simultaneous estimation using passes which are separated from each other with a couple of hours. This method clearly shows not only faster convergence but also seems to be a lot more stable. Although it requires less function evaluations, it takes more time as larger integration arcs are necessary each iteration.

The third setup concerns assessing the performance of a pass-by-pass attitude estimation in a long arc. In this way the attitude state is propagated each pass to the next one after which its state is corrected again. Here it was clearly visible that the attitude state propagator performance lacks accuracy if the spin axis is not oriented in exactly the same direction of the principal axis. This is due to the step size accuracy in the RK4 propagator. If the principal axis is aligned with the spin axis this problem is solved as the attitude integration becomes a lot more simple and a one second step size suffices to accurately integrate the attitude state up to 14 hours.

6

Real attitude determination

> *"When something is important enough, you do it even if the odds are not in your favor."*
>
> — *Elon Musk* Founder of SpaceX

Off course in reality there does not exist as much data as was simulated. From section 4.6.3, it became clear that there exists quit some separation between data. Furthermore from the simulation study in chapter 5, it became clear that a large pass (minimum 2 cycles) is necessary in order to find the correct corresponding attitude information. As is found as well, that several local minima exist and the a-priori estimate of the initial condition must lie as close as possible to the true solution.

Section 6.1 will start with examining the quality of the orbits and the residuals. This is rather important, as it was assumed that the orbit would resemble the COM. Next, in section 6.2, real SLR data will be used in order to derive its attitude using single passes with the Euler Quaternion (EQ) method. Finally, this chapter will give a brief implementation of the found attitude states within the orbit determination process in section 6.3 after which this chapter will end in section 6.4 with some conclusions.

6.1. Averaging data

The real residuals are a result from a seven day orbit determination arc as explained in chapter 4. Each block of seven days contains thus slightly different station passes. Due to this non consistency in the number of NP in a data set, the orbit quality shifts a little bit. This section will show the residual and orbit quality and their relationship with each other.

Residuals Not only the orbit will shift, but the corresponding residuals as well. Therefore for each normal point, seven different values exist. These slightly different residuals can be averaged which allows them to be compared with each other. In figures 6.1 and 6.2 two examples are shown.

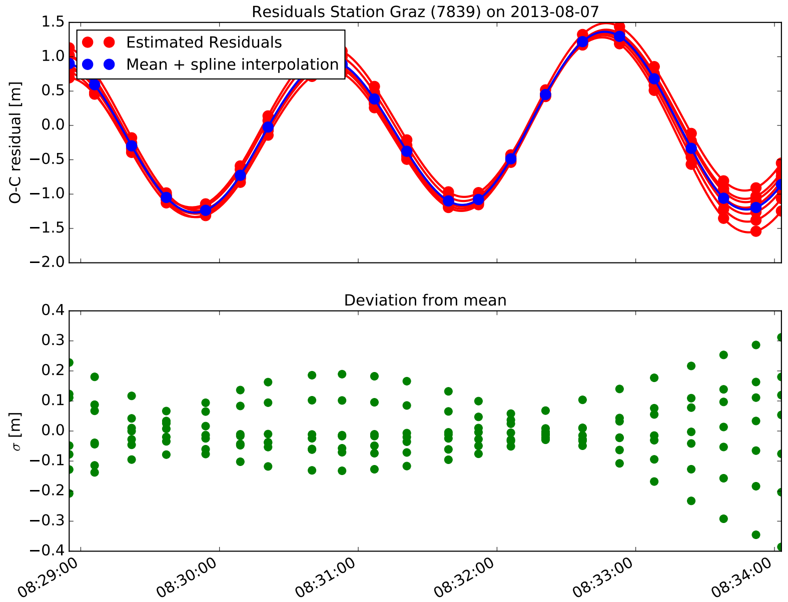

Figure 6.1: Average residuals for each different OD run

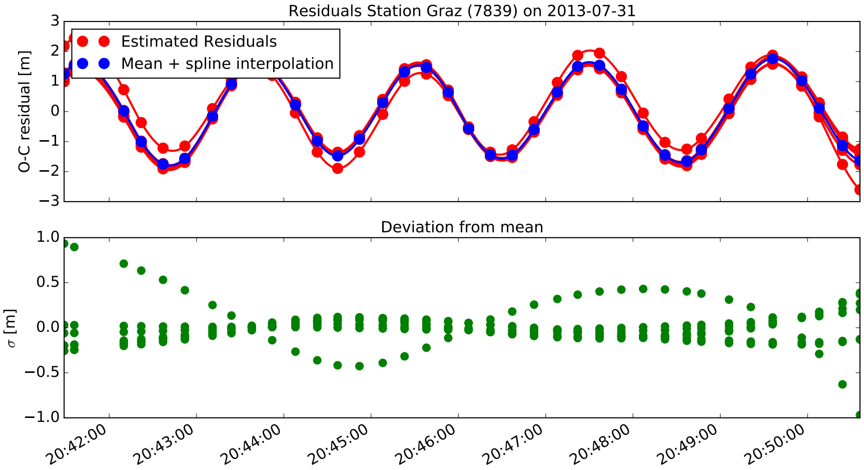

Figure 6.2: Average residuals for each different OD run 2

All residual sets follow the same shape in all cases as this indicates the rotational behaviour. Small offset are however visible between different residuals. As mentioned before in section 4.4, the empirical accelerations tend to correct the force models for all unknown discrepancies. The largest offsets between the residuals at the same NP for shifted arcs, can reach values up to 0.60 m. It is clear that not the entire residual set is shifted up or down with a constant but a trend can be visualised as is shown by green points in the bottom of figures 6.1 & 6.2, showing the deviation from the specific residual set to the mean. The reason for this trend is still unclear but is most likely caused by the slightly different orbit solutions found. Interesting to see is that each residual line from each orbit determination run does not follow the same trend but crosses each other at specific moments in time. It seems like a periodic single cycle is shown. This could be due to the empirical accelerations which tend to bend the residual signal around the orbit.

Orbit The same holds for the orbit data, which is directly related to the estimated residuals due to the vectors used. Some arcs contain a lot of normal points, others less. It is interesting to see what the orbit error is between the two extremes. For each day, seven versions of orbit data where compared for an entire orbit (with a step size of 60 seconds). The results of six hours of data are shown in figures 6.3 and 6.4.

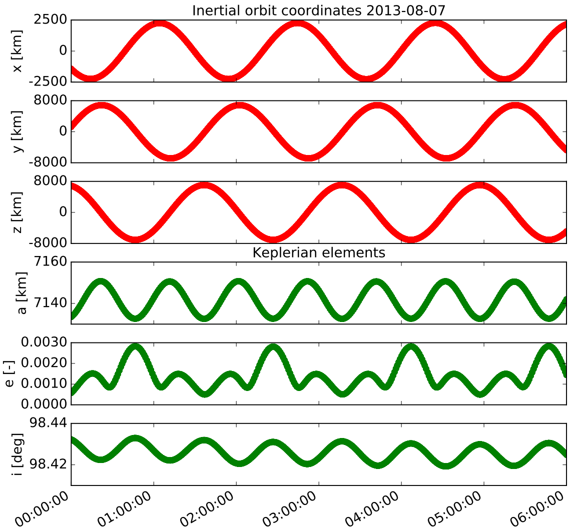

Figure 6.3: Inertial orbits on 2013-08-07

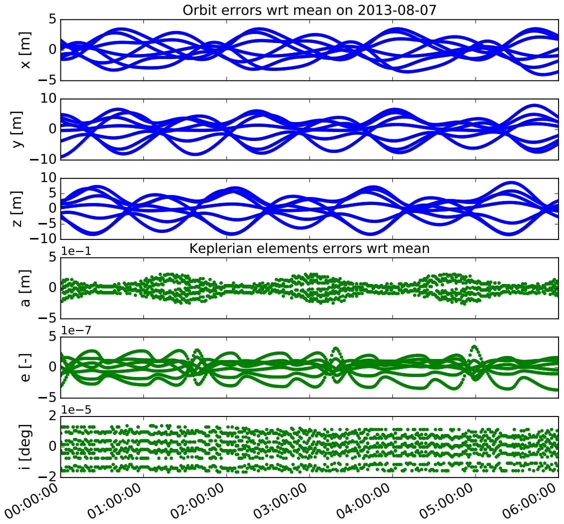

Figure 6.4: Relative to mean on 2013-08-07

A clear periodic behaviour is visible in figure 6.4, as about four orbits have been selected. The standard deviations are given with respect to the mean of all seven passes. The way these standard deviations behave can be linked to the orbit. Minimum errors appear to occur at the extremes of the corresponding orbit axis, whereas the maximum standard deviation with respect to the mean is visible when the orbit crosses the perpendicular plane of the two remaining axes. The reason for this periodic cycle lies in the small shifts between the Kepler elements. As can be seen in figure 6.4, small constant deviations exist between the inclinations of the particular seven day orbit arc. Each orbit run thus has a slightly different inclination which results in a slightly different orientation of the orbit. The semi-major axes and eccentricity show to have slight variations, but are considered really small.

Combined orbit error and residual error Whether or not there exists a link between the orbit error due to the lack of sufficient SLR data and the effect on the residuals still needs investigation. From figure 6.1 it was already shown that the residuals might lie up to 0.6 m from a mean depending on the orbit. This bias is important for the attitude estimation as it is assumed that the orbit resembles the COM position of the spacecraft. Figure 6.5 shows the different residuals for each arc indicated with a particular color. The corresponding orbit errors with the same color code corresponding to a particular orbit run is given in figure 6.6.

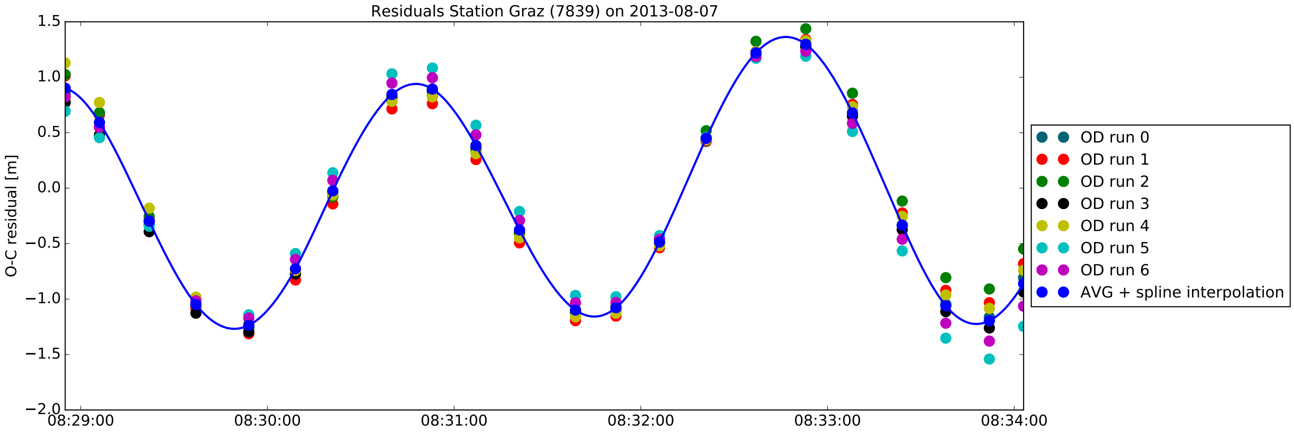

Figure 6.5: Residuals for different OD runs

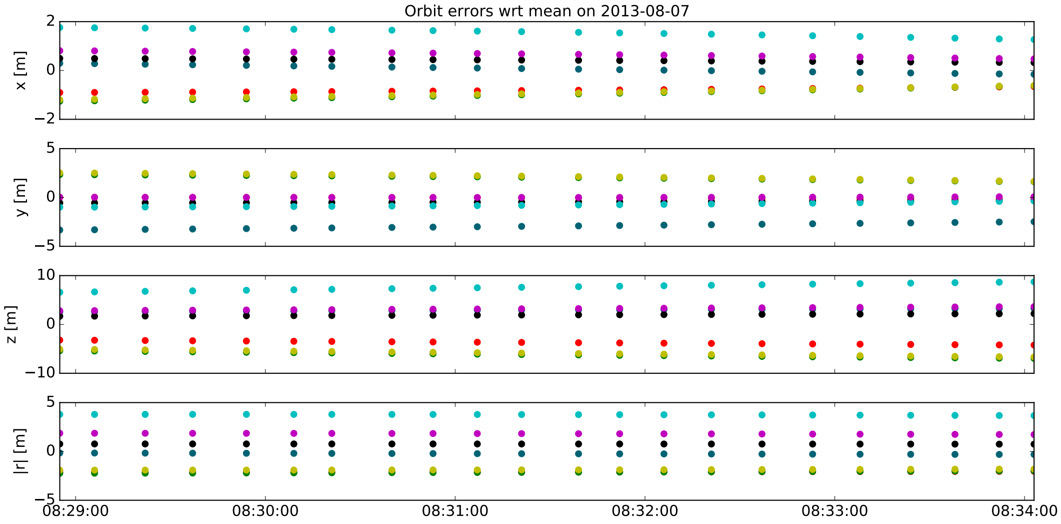

Figure 6.6: Orbit error for different OD runs

Comparing figures 6.5 with 6.6 it can be seen that larger orbit errors correspond to larger deviations in the residuals. The amount of normal points in each OD arc is given in the table 6.1. This shows that the highest amount of normal points does not necessary correspond to the residuals which are closest to the mean.

Table 6.1: Number of NP in each OD run 1

OD run	0	1	2	3	4	5	6
Nr. of NP's	384	354	353	377	416	379	305

Another example of orbit residual error with respect to the orbit error scan be found in figures 6.7 and 6.8

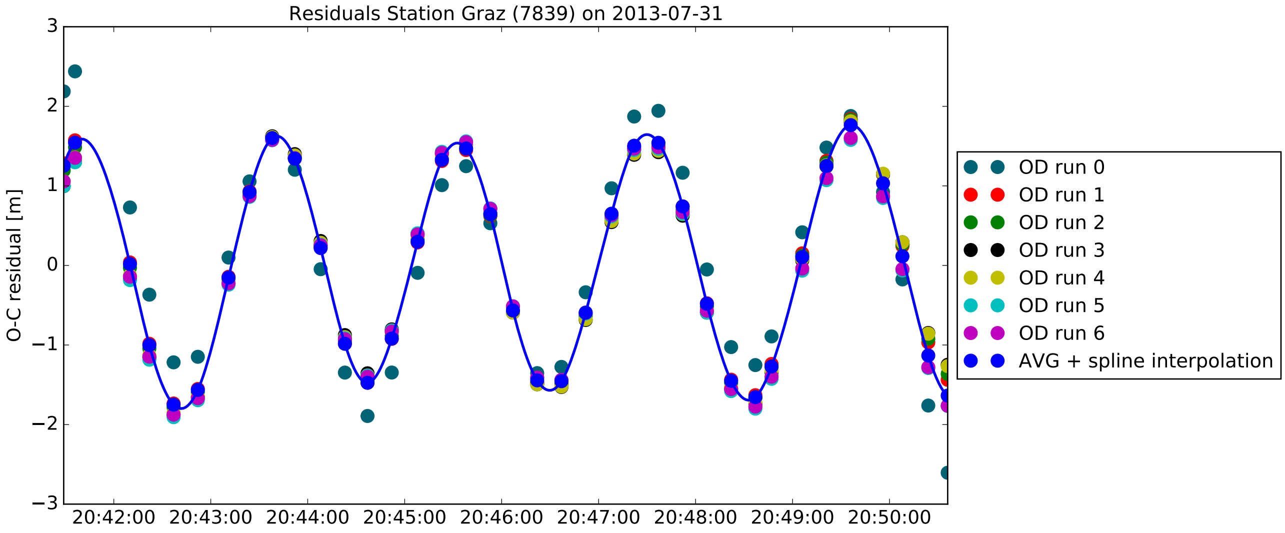

Figure 6.7: Residuals for different OD runs 2

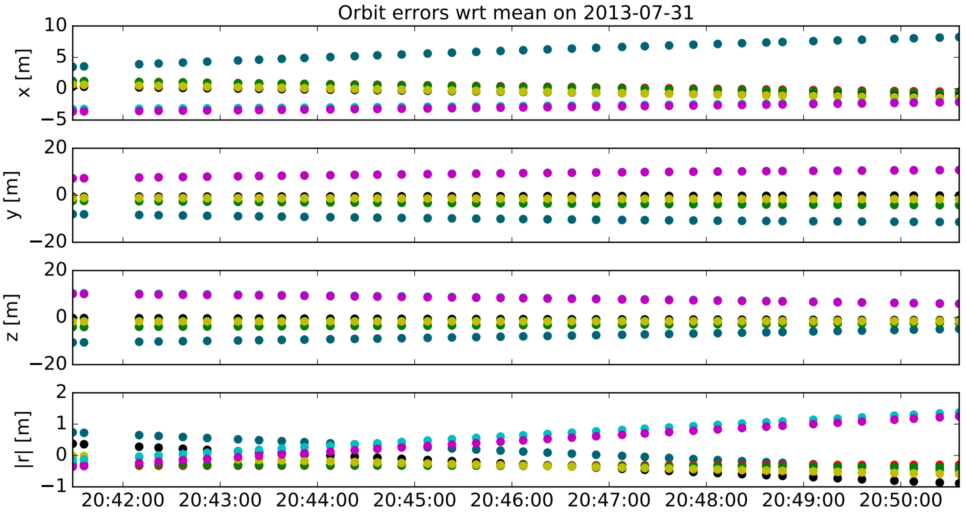

Figure 6.8: Orbit differences for different OD runs 2

Table 6.2: Number of NP in each OD run 2

OD run	0	1	2	3	4	5	6
Nr. of NP's	286	276	250	212	190	309	333

This shows that the number of normal points is not decisive in the quality of the orbit determination. The first run shows to have the highest deviation in residuals from the mean, but does not correspond to the arc with the lowest number of normal points. Therefore the cause in the orbit quality could lie in the specific normal points from each station. This might be due to having several shorter arcs in the normal points which only cover less than an entire rotational period. Interesting to see would be what the orbit determination accuracy does when only passes are considered which cover an entire revolution of Envisat. In this way the residuals would level out around the COM.

Evaluating orbit determination with only long passes Due to the relatively slow rotational period of Envisat, the orbit determination run could get confused by a station pass which only consists of a few normal points. The quality of the orbit is checked for several thresholds. These include first a full rotation, such that the minimum pass length should be larger than 140 seconds in 2013. In this way the range residuals should oscillate three times pass the COM range point. Secondly, a half rotation (t > 70 s) is considered where the laser signal should pass the COM line twice and thirdly a 40 second threshold where only very short passes (smaller than two normal points) are excluded from the orbit determination run. The orbit deviations with respect to their mean are given in figures 6.9, 6.10, 6.11 and 6.12.

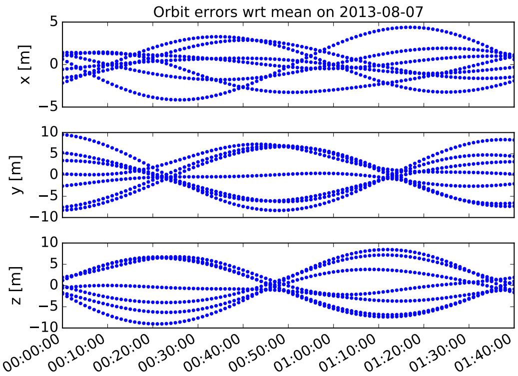

Figure 6.9: Orbit deviations with all NP's (314 NP's)

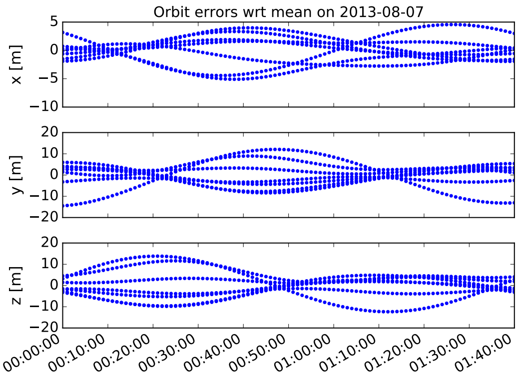

Figure 6.10: Orbit deviation with a threshold of 40 s (295 NP's)

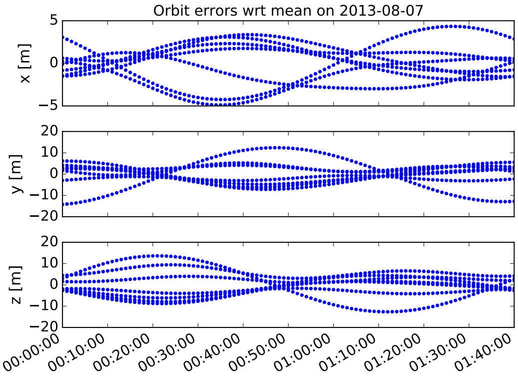

Figure 6.11: Orbit deviation with a threshold of 70 s (290 NP's)

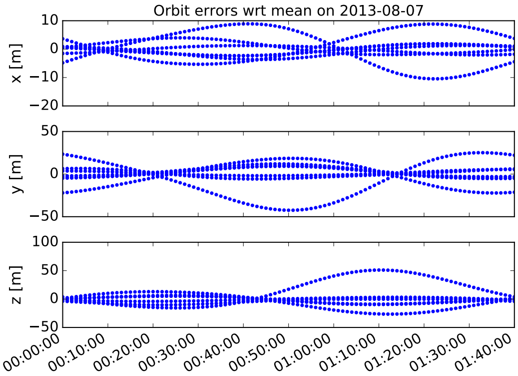

Figure 6.12: Orbit deviation with a threshold of 140 s (260 NP's)

From the figures above, it can be seen that the maximum deviations in all cases show to be not higher than 5 meters in X_i direction for this particular orbit. Slight deviation differences can however be observed in the Y_i and Z_i direction in the i-frame. Imposing thresholds on the minimum NP length does not show to cause significant changes in the maximum deviations of the orbit error. This small study does not show the full effect of this option. Analysing a larger data set could give a better overview of this effect.

It can be concluded that there is a slight correlation between the orbit error and the residuals, but these do not deviate far from each other. Large empirical accelerations ensure that the residual signals are almost similar. Without these, orbit errors would be even larger as was seen by the shifted residuals in section 4.4.

Removing all additional trends As is addressed by Silha et al. (2016) the along-track error remains dominant in the SLR residuals. The ACCEL9 cards of GEODYN mainly ensure a nice fit of the residuals, but an additional linear trend can be taken from the left-over residuals as well. In a residual set a non-linear residual behaviour shows the dynamical behaviour of the LRR versus the COM. A linear trend could indicate a local orbit error which changes slightly in a pass, therefore in the upcoming analysis, linear trends are removed in the real residuals.

6.2. Evaluating local passes

There are a few key differences between the simulated residuals and the real residuals. First, the simulated orbit is assumed to follow the exact COM position, whereas as was just indicated that the real orbit data shows fluctuations and thus does not represent the exact COM position. Secondly, the attitude state is known in the simulated case, making it easy to validate the found attitude state. Last, in the simulated case, the COM and LRR positions are assumed to be correct which might not be true for the real case.

When switching to real residuals, an initial attitude solution must first be found. For this, a certain zone is selected in the entire SLR data set with enough long passes. The week from 30 July to 4 August 2013 onwards contains a long (NP>20) pass each day (which is relatively high). On average it takes about 4.7 days for a long pass to take place.

This section will only cover local pass in order to find a global true solution. As a starting point, a very long pass is selected to determine a possible global solution. This pass consists of 37 NP's and is taken on the 31st of July 2013 from Graz. From this solution one can propagate further until the next pass as was demonstrated before using simulated residuals.

Kucharski et al. (2014) already came up with an expression of the inertial spin period. This followed a linear trend given as:

$$T_{inertial} = 0.0367320 \cdot D + 124.883 \tag{6.1}$$

With an RMS of 0.91 seconds and where D represents the day of the year in 2013. This means that during this pass Envisat should be spinning with an inertial period of 133 seconds. Given its small uncertainty, a safety factor of 5% is added to set the bounds for the period from 125 to 140 seconds. The rest of state parameters are unknown. As was shown for the simulated results, the use of the EQ method shows promising results for global local attitude determination. The spacecraft is first rotated over an Euler angle with an assumed spin axis location which coincides with one of the principal axis(in this case th Z_b axis), after which the full quaternion set is derived which allows a more detailed set of its attitude. The initial conditions(see table 6.3) are set at a spin axis orientation as given by Kucharski et al. (2014) and an Euler angle which is chosen arbitrary at 0 °.

Table 6.3: Initial conditions local double method

Az [deg]	El [deg]	Period [s]	Euler angle [deg]
270	-28	133	0

The simulated residuals are created with the same orbit which are used to create the residual set. The convergence results are plotted below.

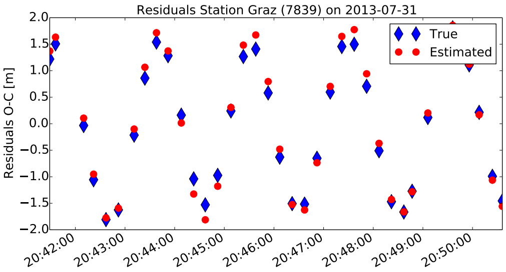

Figure 6.13: Convergence with real data $\vec{x} = [277°, 23°, 128.7s, 0.21, -0.40, 0.74, 0.49]$

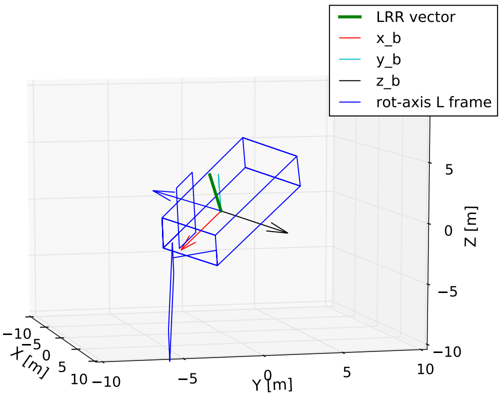

Figure 6.14: Corresponding initial attitude in 3D

The converged condition clearly deviates from the initial proposed condition. Furthermore, the state rotational state where Envisat is rotating in is physically not possible due to the viewing cone restrictions of the LRR. This has been validated using STK as can be seen in figure 6.15.

Figure 6.15: LRR viewing cone not in reach with Graz station during a pass on 31 July 2013, 20:45

If specific bounds are put on the estimation scheme which correspond to the assumed spin axis direction from Kucharski et al. (2014), the residuals do not approach the created signal as close as was shown in figure 6.13. In figure 6.16 the body-fixed z-axis is aligned with the spin axis.

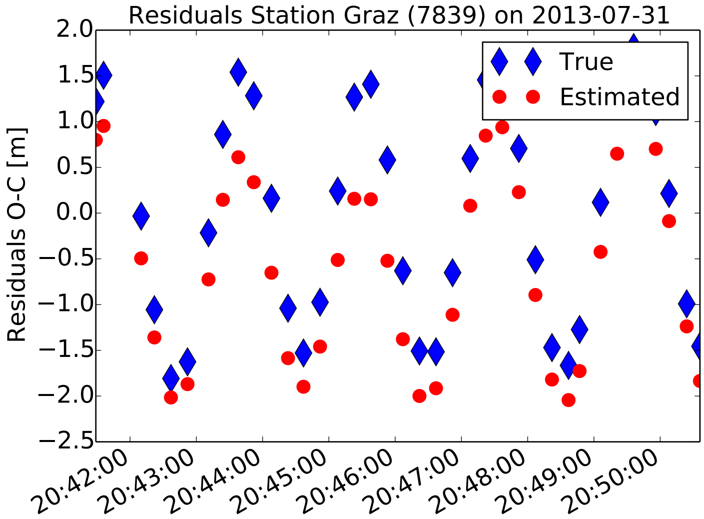

Figure 6.16: Residuals after fixed spin axis location and bounds as found by Kucharski et al. (2014)

The constrained fit shows a clear deviation from the true residuals. The best fit does not match the true residual signal. It is still unclear what the reason for this deviation could be. A possible transformation error is not excluded. Fact is that pointing up or down from the normal plane in the l-frame shows entirely different residual signals.

Effect of empirical accelerations on residuals Due to the empirical accelerations the residuals will be slightly affected as well. This makes it hard on the estimation scheme which converges to entirely different elevation angles corresponding to the best fit of that residual set. For instance, if for the same arc the empirical accelerations are left out, slightly different residuals as is seen in figure 6.17.

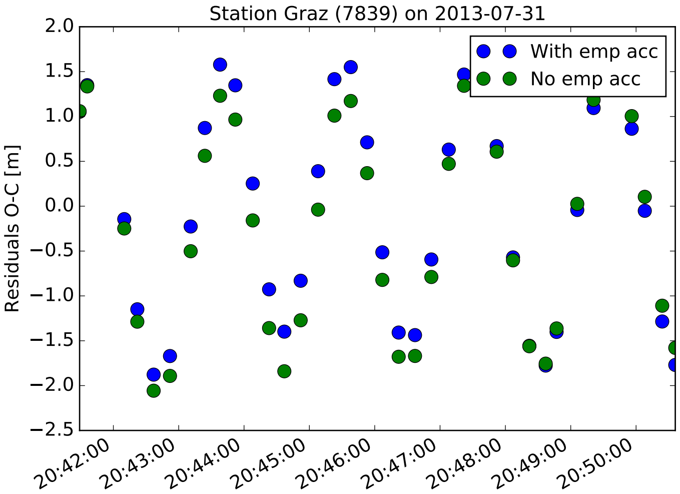

Figure 6.17: Difference between residuals when empirical accelerations are left out

When the estimation scheme is run the best convergence results are given in table 6.4.

Table 6.4: Convergence results with respect to empirical acceleration option

Run	Min f [m]	Az [deg]	El [deg]	Period [s]	qw [-]	qx [-]	qy [-]	qz [-]
No emp acc	0.62	279.3	2.84	128.9	0.26	-0.36	0.64	0.62
With emp acc	1.19	275.2	21.11	128.1	0.21	-0.37	0.75	0.49

Clearly a large difference in elevation angle can be seen. This shows that even a slight difference in residual can have a large impact on the best fitted model. As was discussed before in section 6.1, each residual set shows slight differences. This small test shows that a slight difference in residual could translates in a large difference in best fitted spin axis location.

CCW/CW Kucharski et al. (2014) already mentioned that Envisat should be rotating Counter-Clockwise (CCW) around its spin axis as was found by comparing the RMS of the spin phase residuals. The CCW case should produce 40% lower residuals than the CW part. Counter-clockwise rotation is defined by Kucharski such that the solar array first passes the along-track direction and consequently the radial direction. The CCW representation can also be described as rotating with a motion opposite to that of the motion of the orbit. Silha et al. (2016) found this rotation axis direction as well by observing the shift in peaks between the true and estimated residuals. For a particular pass as given in table 6.5 a decrease of almost 87% is visible.

Table 6.5: Rotation direction analysis for a pas from Graz on the 31st of July 2013(20:42)

Option	RMS [m]	Euler angle [deg]
CCW	1.24	-61
CW	8.99	35

2013-2015 local pass results Figure 6.18 shows the spin axis location and its corresponding rotational velocity for all passes longer than 20 NP's from June 2013 till August 2015 based on the local EQ method.

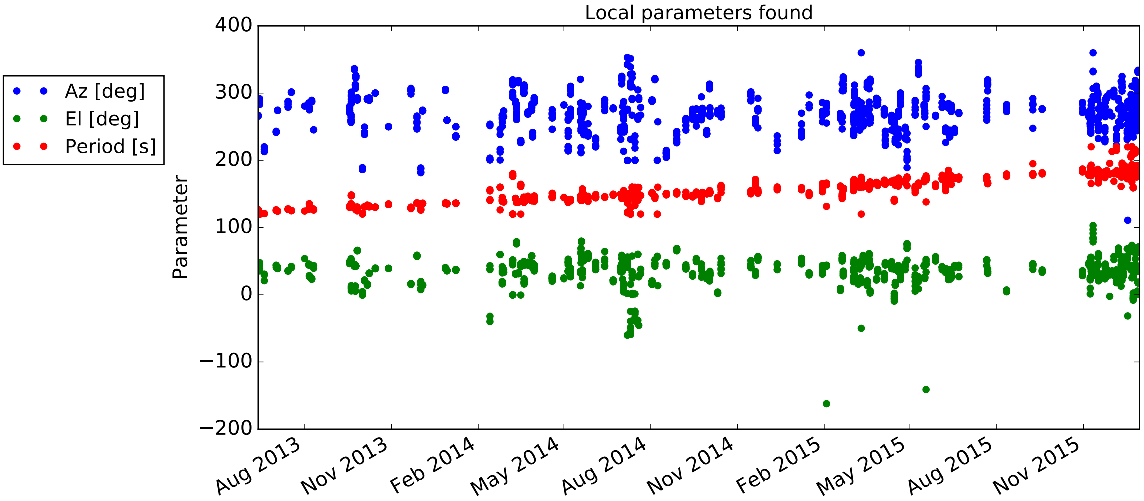

Figure 6.18: Results multiple local estimations

The rotational velocity shows an increase over the years, which corresponds to the increase found by Kucharski et al. (2014). The azimuth and elevation of the spin axis orientation within the l-frame show however larger deviations. The lowest RMS of the solution varies as well between 0.3-4 m with a mean of 1.7 m. All elevation angles are shown oriented positive with respect to the normal. As mentioned before this is not possible due to viewing constraints of the LRR. This might indicate a systematic error in one of the transformations.
Next in figure 6.19 the spin axis direction has been plotted from figure 6.18 covering the entire time span from August 2013 up to December 2015. It clearly shows a large range wherein the spin axis evolves. The mean of the azimuth and elevation parameter is found at 270° and 35.2° respectively. This mean spin axis shows no large deviations over the studied time interval, after several small tests where executed evaluating each year. The distribution of the individual local minima with respect to the mean are plotted in figure 6.20. As was already seen in figure 6.19, the elevation parameter shows to have a quite smaller distribution. Varying azimuth angles thus has a smaller effect on the residuals than varying the elevation angle.

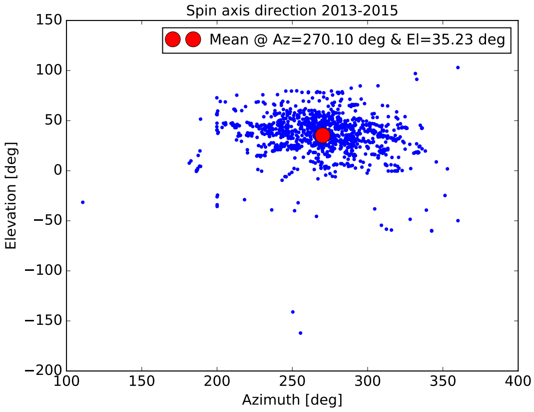

Figure 6.19: Spin axis orientation 08/2013-12/2015

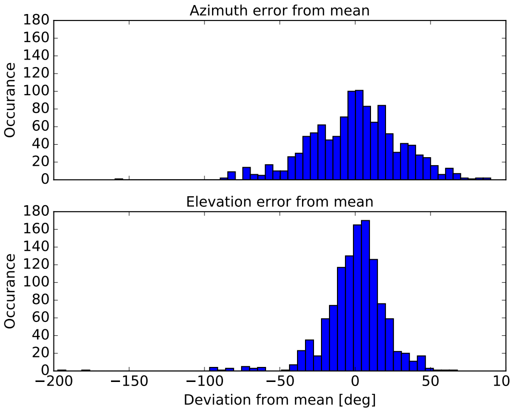

Figure 6.20: Spin axis mean distribution

At first, the large fluctuations might be thought to be caused by the inaccuracy of the local optimization procedure. However, Shakun et al. (2013) analysed Envisat's behaviour using photometric data (using the specular reflections). Shakun did not find a stable, but a precessing spin axis, together with quite large stan-

dard deviations in the spin axis location. This corresponded to middle latitudes (30–60°) and right ascension spin axis angles between 80–100° in May 2013, and between 90–140° in August 2013. No explanation is provided by Shakun concerning the reference frame conventions, however it is believed that the right ascension corresponds to the angular distance measured in the east direction of the l-frame (along the normal plane), which corresponds to the 270° azimuth angle. The 30–60° range of the latitude does correspond with the found elevation range as illustrated in figure 6.19. It is however still unclear if Shakun assumes its latitude convention positive from the nadir vector or from the normal plane.
Kucharski et al. (2014) concluded that Envisat would have a stable spin axis location within the l-frame. Based on this analysis, it can not be confirmed that the spin axis is stable within the l-frame between 2013–2015.

Comparison of results with iOTA The In-Orbit Tumbling Analysis (iota) software is currently under development by Hyperschall Technolgie Göttingen within the framework of ESA's Debris Attitude motion Measurements and Modelling project. It will allow short and long term propagation of the orbit and attitude motion (six-degrees-of-freedom) of a space debris object. Validation of the software will be done by cross-calibration with multiple observations like optical, SLR, radar measurements and signal level determination. The tool will be used for making accurate predictions of the attitude evolution. It includes all relevant internal and external effects, gravitational influences by Earth, Moon and Sun, aerodynamic torques, solar radiation pressure, eddy current damping and internal effects like tank sloshing, moving parts or even the likelihood of an micrometeorite impact torque.
In March 2015, the iOTA team (Kanzler et al., 2016) presented their first results of their simulation using a model of Envisat showing simulated light curves. During the thesis work, another paper was published. The work of Silha et al. (2016) showed the implementation of iOTA using SLR data from Zimmerwald on Envisat by generating synthetic measurements and matching them with their residuals. Interesting though, is that Silha et al. (2016) noticed the contradictory results between Kucharski et al. (2014) and Shakun et al. (2013) orientation of the spin axis, being that Kucharski et al. (2014) found that the spin axis is oriented below the normal plane and Shakun et al. (2013) found an orientation tilted with the normal plane. In its simulated SLR data, Silha et al. (2016) assumes that Envisat is rotating around its principal axis of inertia, which is aligned with the LRR. This setup can be compared to the EQ method in this thesis.
Figure 6.21 shows the matched synthetic with real SLR data of a recent pass in August 2016 (Silha et al., 2016).

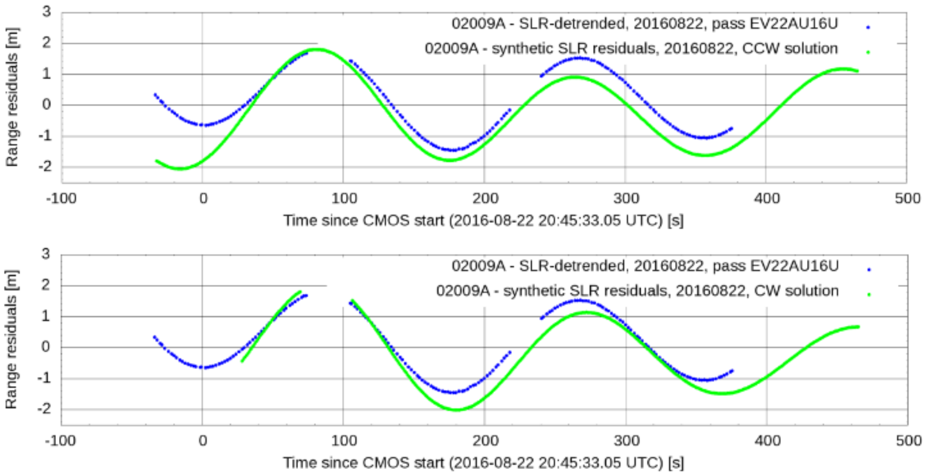

Figure 6.21: Silha et al. (2016) found matching synthetic at real SLR data

It is clearly shown that the synthetic residuals do not match the real SLR residuals entirely, as was found as well during the local passes of this thesis. Furthermore, Silha et al. (2016) concludes that the matched SLR residuals correspond to a spin axis which is slightly tilted compared to the normal as well.

6.3. Investigating the impact on the orbit determination

The found attitude state can be used to have a look at the effect of correcting the offset between the LRR and the COM in GEODYN. This is done as is described in section 4.3.2. By doing so, the found attitude can be validated. one of the common methods to asses the orbit quality of a satellite is to look at its residuals.

The smaller, the better the orbit determination is believed to be. The ultimate goal for passive space debris tracking would be to have residuals which are as small as the active period where the LRR-COM offset was corrected automatically based on a known attitude state. A small test has been performed using the found quaternion set on the 31st of July and implementing it into GEODYN's external attitude file format as was discussed in section 4.3.2. Not the entire seven day has been integrated into the full quaternion set, but only one particular pass in order quickly asses the result and due to the low quaternion accuracy for long-term propagation.

If the elevation error would be just a simple sign error this might be visible in the produced residuals. Using the newly found quaternions does not show any indication of a decrease in size and appear not to show any link.

When the assumed spin axis which was found by Kucharski et al. (2014) is inserted together with the assumption that the body's Z-axis coincides with the spin axis together with a suitable spin phase angle of 48°, the residuals are decreased to about half their original size as is shown in figure 6.22.

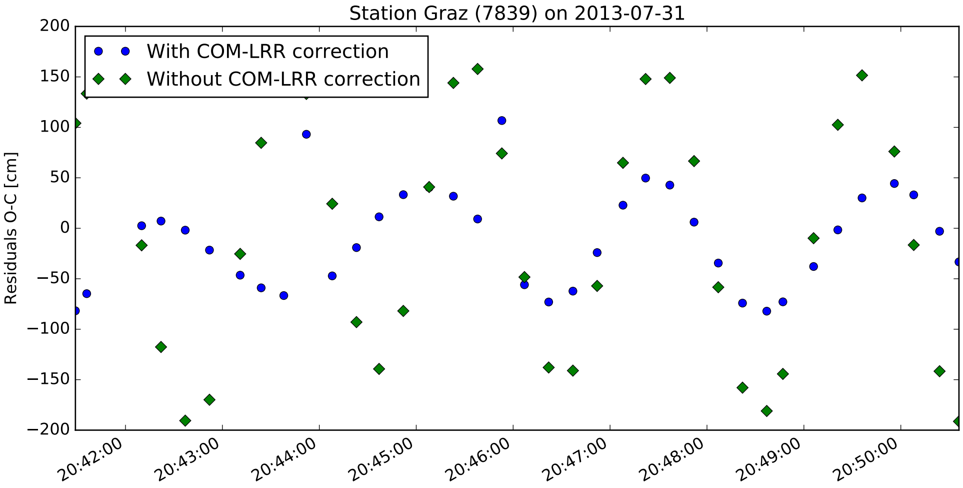

Figure 6.22: COM-LRR correction with spin axis // Z_b axis, Az=270°, El=-28°, P=129s, θ=48°

The corrected residuals clearly show a nearly constant amplitude behaviour, this shows that the attitude file must be in phase with the true attitude mode of Envisat. The remaining amplitude could be the result of the spin axis, which is not perpendicular to the body's z-axis, resulting in a conical motion with the same period.

6.4. Conclusions real data

From the analysis of local passes large ambiguities exist in the determination of the corresponding attitudes. Each local pass seems to converge to a best fit at that particular time. Just like was shown in the simulated cases, a local pass might not always converge to the correct attitude state. Especially when small errors are still included, the local optimization method might not always converge to a true result. Several different residual arc exist due to slightly different orbits. The effect on the residuals can reach values up to 0.6 m. Orbit errors were found in the order of 0-20 m in an inertial orbit frame. Orbit data shows no decrease in error when considering only long passes with multiple revolutions. The smallest rms function value between the estimated and the true attitude did not converge better than 0.5 m, and showed to converge on average to about 1.7 m over the time period 2013–2015. Furthermore the spin axis is shown to be tilted with respect to the normal plane of the orbit (in the l-frame). Several different researchers have found contradictory results concerning the elevation of the spin axis with respect to the normal plane in the l-frame. This work has shown that the spin axis points in the negative normal direction of the l-frame with corresponding azimuth angles ranging from 220–320° and tilted at about 10–60° from the normal plane. Fact is that no stable spin axis orientation has been found, which could indicate precession of the spin axis as was already addressed as a possibility by various researchers. Often, too high spin axis elevation angles make it impossible for the

LRR to be in contact with the ground station if the LRR symmetry axis coincides with the spin axis. When the found attitude from a local pass is used to correct the COM with the LRR, the residuals show to follow the phase of the old cannonball residual. The remaining amplitude of about a meter could be the result of the still unknown precession.

7

Conclusions and recommendations

The main objective of this thesis was to assess the feasibility and performance of attitude determination of tumbling space debris objects equipped with a retro-reflector. As a test case the passive Envisat was used. This chapter will present all the conclusions found during this thesis in section 7.1 and give corresponding recommendations in section 7.2 for further work.

7.1. Conclusions

The main solution brought forward in this thesis involves simulating residuals and matching them to their real counterparts by estimating a full rotational parameter set. The conclusions as a result of this work can be split up intro three parts. First a station analysis and the orbit determination performance of Envisat will be discussed, next the simulated residuals and various test cases are evaluated. Finally, these chosen processes are used on real SLR data and final conclusions are drawn.

7.1.1. Orbit determination

Orbit determination of passive space debris objects is quite different from the orbit determination process of active objects. First of all, there is the lack of sufficient data. The passive Envisat is tracked on average each three orbits. Large deviations in the availability of data however exists over the years. Due to the large concentration of SLR stations in Western Europe, a higher concentration of tracking data is available during the summer months in the Northern hemisphere as a result of better weather conditions. Furthermore only a few stations have tracked Envisat for longer periods of time (larger than 20 normal points). The laser skyplot of Envisat's passes confirms that it is only tracked during passes along the non-normal side of the local orbit frame as was already discovered by Kucharski et al. (2014). The trend of the created osculating residuals show to have a strong dependency on the empirical accelerations as used in GEODYN. These accelerations ensure that the residuals lie centred around orbit while reducing any trends.

7.1.2. Simulated attitude determination

This chapter began with the creation of simulated range residuals. It uses a simplified torque-free rigid body rotational model from chapter 3 in combination with orbital data from chapter 4 and the offset between the laser reflector and the COM in order to create simulated residuals. An a-priori known initial rotational state is used as an input, which together with a particular station pass, creates a theoretical set of residuals. This method is perfectly suited to validate the attitude estimation scheme as it should deliver the known state.
First local optimization is considered after which multiple stations at the same time are analysed. The SLSQP method is selected as an appropriate local optimization method. From these runs, several conclusions where drawn. First of all, a minimum of two revolutions is necessary in order for the local optimization method to converge to the true solution. This however only works if the attitude state is chosen pretty close to the exact solution. In order to solve this problem, clear bounds on the states are necessary. An estimate of the spin axis location can be made by analysing the orientation of the SLR passes within the l-frame, together with viewing cone restrictions of the LRR. The spin period follows from a frequency analysis of the residuals. If the spin axis shows a steady orientation, bounds on the spin axis state could be used for the spin axis location and spin period. The initial attitude state remains hard to constrain as no information is available. In order to cope

with this problem, another estimation procedure is used. If one assumes that one of the bodies principal axes coincides within a certain degree with the spin axis, a new method can be used which first rotates the object around its assumed spin axis over a certain Euler angle keeping the principal axis aligned with this axis. This process uses four state variables in stead of the original seven variables. When this process converges, the full quaternion set may be derived from this newly produced initial condition. During the second phase, the spin axis is free to move away from the spin axis, thus allowing precession. This method has been named the "Euler-Quaternion" (EQ) method.

When using multiple stations in the attitude determination process the problem becomes stronger constraint as it limits the amount of possibilities. If similar station-satellite vector geometries are selected which overlap with each other (single pass), the performance of convergence does not show a direct sign of increase. This effect is slightly similar to having a longer data arc without gaps. When different station-satellite vector geometries are selected, such that the satellite is being tracked on both the positive normal body fixed axis as on the negative side, the convergence time does not show any increase. The produced residuals do not show any difference if compared with the similar station-satellite geometries. This situation could be however nearly impossible for Envisat, due to the assumed orientation of Envisat, making it only possible to be tracked from more or less the same geometries at the same time. Next, two passes were assessed separated 22 minutes from each other. It clearly shows that the amount of iterations has gone down and the solution shows to converge quite well. Using longer arcs may be more difficult for complex attitudes as the RK4 propagator shows increasing errors after three hours with a stepsize of one second. A simplified case where the principal axis is aligned with the spin axis shows no problems under the assumption of a torque free environment.

7.1.3. Real data attitude determination

Only local optimization was considered in this thesis. The Euler Quaternion (EQ) method was used for multiple local long arcs covering at least 20 normal points, which corresponds to about two rotations. Orbit and residual errors were evaluated using the overlapping segments in a seven day orbit arc. Errors were typically in the range of 0-0.6 m for the residuals and 0 - 20 m for the orbit coordinates in an inertial frame. Using only long passes (multiple spacecraft revolutions) shows no decrease in orbit error.

Each found attitude solution shows to be quite different. The inertial rotational period is found with a RMS of a couple of seconds and shows a clear non-linear decaying trend over the years. This corresponds to the work found by Kucharski et al. (2014) and indicates the exponential decaying rotational velocity due to the eddy currents as was found by Gomez and Walker (2013). Furthermore, it has been shown that the spin axis points in the negative normal direction of the l-frame with corresponding azimuth angles ranging from 220–320° and tilted at about 10–60° from the normal plane over the time period 2013-2015 in the local orbit frame. The mean of this orientation is found at 270° and 35° azimuth and elevation angles respectively in the l-frame. These ranges could indicate a changing spin axis orientation over time. All found attitude states correspond to an attitude state where the spin axis is pointed upwards relative to the normal plane in the local l-frame. When the spin axis coincides with the Laser Retro Reflector (LRR) symmetry axis, the orientation is not (always) possible due to viewing constraints of the LRR. Implementing rotating Envisat quaternions in the orbit determination process GEODYN, in order to correct the residuals, show that the proposed spin axis location by Kucharski et al. (2014) does correspond to lower residuals, however a systematic residual (although smaller) is still present which could indicate a certain precession in the spin axis.

This thesis showed that it is possible to derive attitude information from tumbling space objects equipped with a laser reflector, like Envisat. However, there are a few limitations. One of the biggest is the lack of sufficient data. Next, there is the limited visibility of a tumbling satellite equipped with only one reflector. Lastly, the number of revolutions in one particular pass affects the attitude determination process significantly.

7.2. Recommendations

This thesis has shown the performance of a few methods for SLR attitude determination, however there is still enough work to be performed. This section will give further recommendations for future work.

Assessing multiple stations at the same time Due to time constraints and computer performance limitations, a multiple pass attitude determination sequence for real data was not done. It is strongly recommended to assess the performance of this method as it showed promising results for the simulate case where only short arcs where considered.

Assessing its attitude now Envisat's rotational velocity is exponentially decreasing over time. This might form a problem for attitude determination using SLR as the number of rotations per pass decreases in this way. As was found during simulations, a minimum amount of two revolutions is needed in order to find a correct attitude state. Therefore it is highly encouraged to perform attitude simulations using SLR right now in order to understand Envisat's rotation and in this way being able to make better estimates regarding its evolution in the future.

Using a better attitude propagation technique The RK4 propagator lacks accuracy when long term propagation is considered (>3h) for step sizes of one second. In the case of Envisat's large separation between long passes, this is essential in order to assess the attitude of Envisat for an entire arc. Smaller step sizes are thus required when considering this integrator. Other integrators might perform better for similar step sizes.

Evaluate external torques A torque free rigid body was assumed, a more detailed (long-term) evolution of space debris attitude evolution could be given by including external torques like gravity gradient, aerodynamic solar and magnetic.

Producing better orbit data Corrections of the Laser Retro Reflector (LRR) offset in GEODYN shows still some ambiguities. It should be theoretical possible to correct the LRR offset in the orbit determination process and in this way produce better orbits and thus better predictions. It is still unknown how much better these predictions can get if an attitude model is used. Long-term propagation of Envisat's orbit with a modelled attitude(and external torques) could give better decaying/re-entry predictions.

Combining visibility model with residual estimation In order to constrain several options, the LRR viewing cone could be used in combination with the particular station-satellite geometry during an estimation procedure. This might reduces the amount of possible solutions.

Introduce orbit and other errors Real data estimation showed an average difference of about 1.7 m between the best fit residual set and the true residuals. By adding particular errors (like orbit, COM position and inertia tensor) to the simulated estimation of residuals, their effect can better be understood. Right now it is still unclear if the local minima found during this thesis are the true local minima (where the minimum function value dues not drop below the error bias) or false local minima (where the error is due to a wrong attitude state), or a combination of both.

A

Transformations

This chapter will give an overview of the conversions between several attitude representations.

A.1. Euler to DCM

Euler angles are used most often as its representation is easy to understand and visualise. However one major drawback exists which is called Euler-angle singularity of gimbal lock. Where for aircraft this does generaly not pose that of a concern, this does become a problem for rotating objects in space. Next, careful consideration must be given as a set of three angles correspond to twelve different rotation options. A distinguishing between symmetric and asymmetric euler angles can be made. Symmetric euler angles consist of three consecutive rotations around two axis where the first and last axes are the same e.g. XYX. On the other hand the asymmetric sets are the rotations which include three different axes in its set like XYZ.

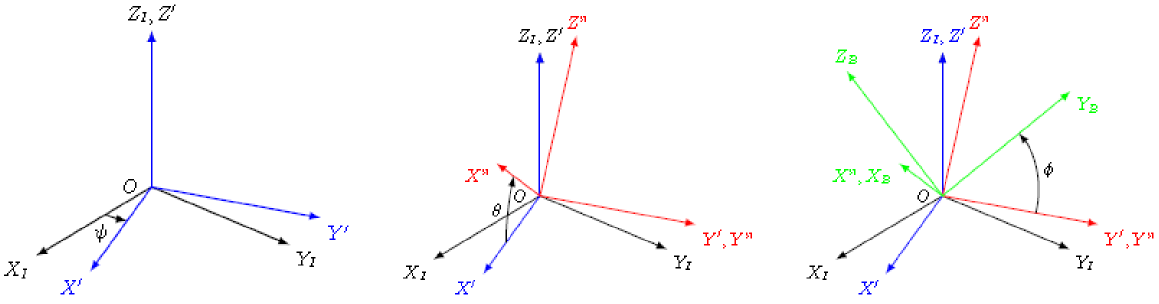

(a) Rotation ψ around Z_I (b) Rotation θ around Y' (c) Rotation ϕ around X"

Figure A.1: Rotation sequence zyx (Habets, 2015)

Figure A.1 shows a rotation from an inertial frame denote by the subscript I to a particular body frame B. The most common used sequence in the Aerospace sector is the so-called 3-2-1 sequence corresponding to first a rotation around the initial Z_I angle over a yaw angle ψ. Next a rotation of this new intermediate frame I' is executed over its Y' axis over a pitch angle θ to end up at the second intermediate frame I"'. Finally a rotation around the new X" axes needs to be performed over a roll angle ϕ. The sequence of rotation is mathematicly expressed through a rotation matrix which combined add up to the full rotation matrix from frame I to B as is given in the proceeding equations.

$$\begin{bmatrix} X' \\ Y' \\ Z' \end{bmatrix} = T_z(\psi) \begin{bmatrix} X_I \\ Y_I \\ Z_I \end{bmatrix} = \begin{bmatrix} \cos\psi & \sin\psi & 0 \\ -\sin\psi & \cos\psi & 0 \\ 0 & 0 & 1 \end{bmatrix} \begin{bmatrix} X_I \\ Y_I \\ Z_I \end{bmatrix} \tag{A.1}$$

$$\begin{bmatrix} X'' \\ Y'' \\ Z'' \end{bmatrix} = T_y(\theta) \begin{bmatrix} X' \\ Y' \\ Z' \end{bmatrix} = \begin{bmatrix} \cos\theta & 0 & -\sin\theta \\ 0 & 1 & 0 \\ \sin\theta & 0 & \cos\theta \end{bmatrix} \begin{bmatrix} X' \\ Y' \\ Z' \end{bmatrix} \tag{A.2}$$

$$\begin{bmatrix} X_B \\ Y_B \\ Z_B \end{bmatrix} = T_x(\phi) \begin{bmatrix} X'' \\ Y'' \\ Z'' \end{bmatrix} = \begin{bmatrix} 1 & 0 & 0 \\ 0 & \cos\phi & \sin\phi \\ 0 & -\sin\phi & \cos\phi \end{bmatrix} \begin{bmatrix} X'' \\ Y'' \\ Z'' \end{bmatrix} \tag{A.3}$$

Which combined result in the Direction Cosine Matrix (DCM) of frame B relative to frame I which is given as

$$\begin{bmatrix} X_b \\ Y_b \\ Z_b \end{bmatrix} = T_x(\phi)T_y(\theta)T_z(\psi) \begin{bmatrix} X_I \\ Y_I \\ Z_I \end{bmatrix} = \begin{bmatrix} c\theta c\psi & c\theta s\psi & -s\theta \\ s\phi s\theta c\psi - c\phi s\psi & s\phi s\theta s\psi + c\phi c\psi & s\phi c\theta \\ c\phi s\theta c\psi + s\phi s\psi & c\phi s\theta s\psi - s\phi c\psi & c\phi c\theta \end{bmatrix} \begin{bmatrix} X_I \\ Y_I \\ Z_I \end{bmatrix} \tag{A.4}$$

Here the cosine is represented by a c and the sine by an s.

A.2. Euler to quaternions

By considering each axis as an euler eigenaxis, a full euler angle representation can be transformed to the quaternions by combining a set of three quaternions (Wie, 2008). First lets consider the multiplication of two quaternion sets(a,b) resulting in a third(c) which can be represented in matrix form as:

$$\begin{bmatrix} c1 \\ c2 \\ c3 \\ c4 \end{bmatrix} = \begin{bmatrix} a_4 & a_3 & -a_2 & a_1 \\ -a_3 & a_4 & a_1 & a_2 \\ a_2 & -a_1 & a_4 & a_3 \\ -a_1 & -a_2 & -a_3 & a_4 \end{bmatrix} \begin{bmatrix} b_1 \\ b_2 \\ b_3 \\ b_4 \end{bmatrix} \tag{A.5}$$

This principle can be used to transform a 3-2-1(Z-Y-X) rotation as follows:

$$\begin{bmatrix} q_1 \\ q_2 \\ q_3 \\ q_4 \end{bmatrix} = \begin{bmatrix} q_4''' & q_3''' & -q_2''' & q_1''' \\ -q_3''' & q_4''' & q_1''' & q_2''' \\ q_2''' & q_1''' & q_4''' & q_3''' \\ -q_1''' & -q_2''' & -q_3''' & q_4''' \end{bmatrix} \begin{bmatrix} q_4'' & q_3'' & -q_2'' & q_1'' \\ -q_3'' & q_4'' & q_1'' & q_2'' \\ q_2'' & q_1'' & q_4'' & q_3'' \\ -q_1'' & -q_2'' & -q_3'' & q_4'' \end{bmatrix} \begin{bmatrix} q_1' \\ q_2' \\ q_3' \\ q_4' \end{bmatrix} \tag{A.6}$$

Where each individual quaternion set is represented by

$$q' = \begin{bmatrix} 0 \\ 0 \\ \sin\frac{\psi}{2} \\ \cos\frac{\psi}{2} \end{bmatrix}, q'' = \begin{bmatrix} 0 \\ \sin\frac{\theta}{2} \\ 0 \\ \cos\frac{\theta}{2} \end{bmatrix}, q''' = \begin{bmatrix} \sin\frac{\phi}{2} \\ 0 \\ 0 \\ \cos\frac{\phi}{2} \end{bmatrix} \tag{A.7}$$

When filling in equation A.7 in equation A.6 and carrying out the entire multiplication the following result is obtained:

$$\begin{bmatrix} q_1 \\ q_2 \\ q_3 \\ q_4 \end{bmatrix} = \begin{bmatrix} \sin\frac{\phi}{2}\cos\frac{\theta}{2}\cos\frac{\psi}{2} - \cos\frac{\phi}{2}\sin\frac{\theta}{2}\sin\frac{\psi}{2} \\ \cos\frac{\phi}{2}\sin\frac{\theta}{2}\cos\frac{\psi}{2} + \sin\frac{\phi}{2}\cos\frac{\theta}{2}\sin\frac{\psi}{2} \\ \cos\frac{\phi}{2}\cos\frac{\theta}{2}\sin\frac{\psi}{2} - \sin\frac{\phi}{2}\sin\frac{\theta}{2}\cos\frac{\psi}{2} \\ \cos\frac{\phi}{2}\cos\frac{\theta}{2}\cos\frac{\psi}{2} + \sin\frac{\phi}{2}\sin\frac{\theta}{2}\sin\frac{\psi}{2} \end{bmatrix} \tag{A.8}$$

A.3. Quaternions to DCM

As discussed in section 2.2 there exists multiple reference frame. Cartesian rectangular frame transformations can easily be achieved using the DCM or the so-called attitude matrix using the following multiplication. The transformation between vector A ($\vec{v}_\mathrm{A}$) and vector B ($\vec{v}_\mathrm{B}$) follows after multiplying the DCM from A to B with the actual vector A.

$$\vec{v}_B = DCM_{B\leftarrow A}\cdot\vec{v}_B \tag{A.9}$$

The DCM can be composed of several representations. One of these is the quaternion parametrized form as given in equation A.10 by Wie (2008).

$$\mathrm{DCM_q} = \begin{bmatrix} 1-2(q_2^2+q_3^2) & 2(q_1q_2+q_3q_4) & 2(q_1q_3-q_2q_4) \\ 2(q_1q_2-q_3q_4) & 1-2(q_1^2+q_3^2) & 2(q_2q_3+q_1q_4) \\ 2(q_1q_3+q_2q_4) & 2(q_2q_3-q_1q_4) & 1-2(q_1^2+q_2^2) \end{bmatrix} \tag{A.10}$$

A.4. DCM to quaternions

If the $\mathrm{DCM_q}$ is known, the corresponding quaternions can be computed using equation A.11 as given by Farrell (2008).

$$q = \begin{bmatrix} \frac{1}{2}\sqrt{1+\mathrm{DCM}[1,1]+\mathrm{DCM}[2,2]+\mathrm{DCM}[3,3]} \\ \frac{\mathrm{DCM}[3,2]-\mathrm{DCM}[2,3]}{4q_1} \\ \frac{\mathrm{DCM}[1,3]-\mathrm{DCM}[3,1]}{4q_1} \\ \frac{\mathrm{DCM}[2,1]-\mathrm{DCM}[1,2]}{4q_1} \end{bmatrix} \tag{A.11}$$

Bibliography

J.B. Abshire and C.S. Gardner. Atmospheric refractivity corrections in satellite laser ranging. In *IEEE Transactions on Geoscience and remote sensing, vol. GE-23 NO4, July 1985*, 1985.

K. Akins, L. Healy, S Coffey, and M. Picone. Comparison of msis and jacchia atmospheric density models for orbit determination and propagation. In *13th AAS/AIAA Space Flight Mechanics Meeting Paper AAS 03-165*, 2003.

L.J. Alvarez. Envisat-1 mission CFI software, mission conventions document. Technical report, GMV and ESA, 1997.

H. Krag B. Bastida Virgili, S. Lemmens. Investigation on envisat attitude motion. *e.Deorbit Workshop 06/05/2014*, 2014.

P. Bargellini, M. A. Garcia Matatoros, L. Ventimiglia, and D. Suen. Envisat attitude and orbit control in-orbit performance: An operational view. *6th International ESA Conference on Guidance, Navigation and Control Systems, held 17-20 October 2005 in Loutraki, Greece. Edited by D. Danesy. ESA SP-606. European Space Agency, 2006. Published on CDROM., id.52.1*, 2006.

F Barlier, C Berger, JL Falin, G Kockarts, and G Thuillier. A thermospheric model based on satellite drag data. In *Annales de Geophysique, volume 34, pages 9–24*, 1978.

J. Bennett, J. Sang, C. Smith, and K. Zhang. Improving low-earth orbit predictions using two-line element data with bias correction. In *Proceedings of the Advanced Maui Optical and Space Surveillance Technologies Conference, held in Wailea, Maui, Hawaii, September 11-14, 2012, Ed.: S. Ryan, The Maui Economic Development Board, id.46*, 2012.

P.T. Boggs and J.W. Tolle. Sequential quadratic programming. *Acta Numerica*, 1995.

C. Bonnal, J. M. Ruault, and M. C. Desjean. Active debris removal: Recent progress and current trends. *Acta Astronautica, 85, 51-60.*, 2013.

L. Cerri, A. Couhert, and P. Ferrage. Doris satellites models implemented in poe processings. Technical report, CNES, IDS, 2016.

B. G. Cour-Palais D. J. Kessler. Collision frequency of artificial satellites: The creation of a debris belt. *Journal of Geophysical Research, Volume 83, Number A6, pp. 2637-2646*, 1978.

Y.H Dai. A perfect example for the bfgs method. *Mathematical programming*, 2013.

J. I. A. de la Fuente. *Enhanced Modelling of LAGEOS Non-Gravitational Perturbations.* PhD thesis, Delft, University of Technology, 2007.

J. Degnan. Satellite laser ranging: current status and future prospects. *IEEE Transactions on Geoscience and Remote Sensing*, 1985.

J. Degnan. Slr2000: An autonomous and eyesafe satellite laser ranging station. In *Proceedings of the 9th International Conference on Laser Ranging Instrumentation, Canberra, November*, pages 7–11, 1994.

J.A.F. Deloo. Analysis of the rendezvous phase of e.deorbit, guidance, communication and illumination. Master's thesis, Technical University Delft, 2014.

DLR-IMF. Nominal and mission extension orbit of envisat, 2016. URL `https://earth.esa.int/web/guest/missions/esa-operational-eo-missions/envisat/instruments/sciamachy-handbook/wiki/-/wiki/SCIAMACHY%20Handbook/Orbit+and+Attitude`. [Online; visited on 14-12-2015].

E. Doornbos, P. Visser, G. Koppenwallner, and B. Fritsche. Algorithm theoretical basis document, version 1.1. Technical report, TU Delft, HTG, 2013.

Eelco Doornbos. Modeling of non-gravitational forces for ers-2 and envisat. Master's thesis, TU Delft, 2001.

eoPortal Directory. Lageos-i (laser geodynamics satellite-i) / lageos-ii. URL `https://directory.eoportal.org/web/eoportal/satellite-missions/l/lageos`. [online; visited on 10-11-2016].

ESA. Goce esa gravity explorer. URL `https://www.esa.int/esaKIDSen/SEM7AHVG3HF_Earth_3.html`. [online; visited on 09-11-2016].

ESA. *Envisat-1 Mission and System Summary*, 1998. URL `http://envisat.esa.int/support-docs/pdf/mis_sys.pdf`. Brochure, [online; visited on 26-04-2016].

ESA. Envisat instruments: Lrr, 2002. URL `https://earth.esa.int/web/guest/missions/esa-operational-eo-missions/envisat/instruments/lrr`. [online; visited on 12-4-2016].

ESA. Investigation of envisat continues, 2012a. URL `http://www.esa.int/Our_Activities/Observing_the_Earth/Envisat/Investigation_on_Envisat_continues`. [image online; accessed 14-12-2015].

ESA. Cdf study report e.deorbit e.deorbit assessment. Technical report, Concurrent Design Facility, ESTEC, 2012b.

ESA. Envisat(environmental satellite), 2016a. URL `https://directory.eoportal.org/web/eoportal/satellite-missions/e/envisat`. [online;visited on 26-4-2016].

ESA. *Reference Systems and Frames*. European Space Agency, 2016b. URL `http://www.navipedia.net/index.php/Reference_Systems_and_Frames`. [online; visted on 18-5-2016].

ESA. *Space Segment ENVISAT*, 2016c. URL `https://earth.esa.int/web/guest/missions/esa-operational-eo-missions/envisat/satellite/space-segment`. [online; visited on 16-5-2016].

European Space Agency. e.deorbit implementation plan, 2015. URL `http://blogs.esa.int/cleanspace/files/2016/02/e.deorbit-Implementation-Plan-Issue_1_2015.pdf`. [online; visted on 20-11-2016].

J. Farrell. *Aided navigation: GPS with high rate sensors*. McGraw-Hill, Inc., 2008.

J. Fiege, H. Bendel, and J. Ender. Science report, August 2013. URL `http://www.fhr.fraunhofer.de/content/dam/fhr/en/documents/Fraunhofer_FHR_Science_Report_web.pdf`. [online; visited on 26-04-2016].

H.P. Gavin. The levenberg-marquardt method for nonlinear least squares curve-fitting problems. Technical report, Department of Civil and Environmental Engineering, 2016.

N.O. Gomez and S.J.I. Walker. Earth's gravity gradient and eddy currents effects on the rorotation dynamics of space debris objects: Envisat case study. Technical report, Southampton University, 2013.

M. Gottwald, F.-J. Diekmann, and T. Fehr. Envisat- sciamachy's host. Technical report, Remote Sensing Technology Institute German Aerospace Center, ESOC and ESRIN, 2010.

J.M.G. Habets. Evolving systems approach to the attitude control of a large-space-debris removal spacecraft. Master's thesis, TU Delft, 2015.

S.F. Harvey, A. Lebru, and R. Kerner. Thermal design of the Envisat-1 ASAR active antena. *Sixth European Symposium on Space Environmental Control Systems, held in Noordwijk, The Netherlands, 20-22 May*, 1997.

A.E. Hedin. Msis-86 thermospheric model. *Journal of Geophysical Research: Space Physics, volume 92, number A5, pages 4649–4662*, 1987.

Inter-Agency Space Debris Coordination Committee. Iads space debris mitigation guidelines, 2007. URL `http://www.unoosa.org/documents/pdf/spacelaw/`. [online; visited on 11-10-2016].

L.G. Jacchia. New static models of the thermosphere and exosphere with empirical temperature profiles. *SAO Special Report volume 313*, 1970.

F. Jensen. Scattering from a low-orbiting satellite with rotating solar array. Technical report, TICRA, 2005.

R. Kanzler, J. Silha, T. Schildknecht, B. Fritsche, T. Lips, and H. Krag. Space debris attitude simulation- iota (in-orbit tumbling analysis). In *Proceedings of the Advanced Maui Optical and Space Surveillance Technologies Conference, held in Wailea, Maui, Hawaii, September 15-18, 2014*, 2015.

R. Kanzler, J. Silha, T. Schildknecht, B. Fritsche, T. Lips, and H. Krag. First results of iota (in-orbit tumbling analysis). In *6th International Conference on Astrodynamics Tools and Techniques, 14-17 March 2016, Darmstadt*, 2016.

G Kirchner, F Koidl, D Kucharski, W Steinegger, and E Leitgeb. Using pulse position modulation in slr stations to transmit data to satellites. In *Proceedings of the 2011 11th International Conference on Telecommunications (ConTEL)*, pages 447–450, 2011.

G. Kirchner, F. Koidl, M. Pioner, P Lauber, J. Eckl, M. Wilkinson, R Sherwood, et al. Multistatic laser ranging to space debris. In *18th International Workshop on Laser Ranging, 13-0213, November 2013*, 2013.

H. Krásná, J. Böhm, and H. Schuh. Tidal love and shida numbers estimated by geodetic vlbi. *Journal of geodynamics, volume 70, pages 21–27*, 2013.

D. Kucharski, G. Kirchner, T. Otsubo, and F. Koidl. 22 years of ajisai spin period determination from standard slr and khz slr data. 2009.

D. Kucharski, S. Schillak, H.C. Lim, and T. Otsubo. Spectral analysis of borowiec slr data for spin determination of geodetic satellite egp. In *Artifical Satellites, Vol. 48. no -1*, 2013.

D. Kucharski, G. Kirchner, F. Koidl, C. Fan, Carman R., C. Moore, A. Dmytotsa, et al. Attitude and spin period of space debris envisat measured by satellite laser ranging. In *IEEE Transactions on Geoscience and Remote sensing, vol 52, NO. 12, December 2014*, 2014.

S. Lemmens, H. Krag, J. Rosebrock, and I. Carnelli. Radar mappings for attitude analysis of objects in orbit. In *6th European Conference on Space Debris, At Darmstadt, Volume: ESA SP-723*. European Space Agency, Fraunhofer Institute for High Frequency Physics and Radar Techniques,, 2013.

F.G. Lemoine, N.P. Zelensky, D.D. Rowlands, S.B. Luthcke, T.A. Pennington, D.S. Chinn, D.S. Beckley, et al. Calibration and validation of the precise oorbit for ostm- extending the topex, jason-1, and jason-2 climate data record for msl studies. In *Ocean Surface Topography Science Team Meeting*, 2009.

D.C. Liu and J. Nocedal. On the limited memory bfgs method for large scale aptimization. *Mathematical programming*, 1989.

N.R. Lomb. Least-sqaures frequency analysis of unequally spaced data. *Astrophysics and space science, volume 39, number 2, pages 447–462*, 1976.

R. Mallipeddi and P.N. Suganthan. Emperical study on the effect if population size on differntial evolution algorithm. In *Conference: Proceedings of the IEEE Congress on Evolutionary Computation, CEC 2008, June 1-6, 2008, Hong Kong, China*, 2008.

J. J. McCarthy, S. Rowton, D. Moore, D.E. Pavlis, S.B. Luthcke, and Tsaoussi L.S. *GEODYN II: Systems Description Volume 1*. NASA, Space Geodesy Branch, Greenbelt, 1972.

J. W. McMahon and D. J. Scheeres. Improving space object catalog maintenance through advances in solar radiation pressure modeling. *Journal of Guidance, Control, and Dynamics, volume 38, number 8, pages 1366–1381*, 2015.

O. Montenbruck and E. Gill. *Satellite Orbit, Modles, Methods, and Applications*. Springer, 2001.

S. I. Nishida and T Yoshikawa. Space debris capture by a joint compliance controlled robot. In *Advanced Intelligent Mechatronics, 2003. AIM 2003. Proceedings. 2003 IEEE/ASME International Conference on (Vol. 1, pp. 496-502)*, 2003.

R. Pail, S. Bruinsma, F. Migliaccio, C. Förste, H. Goiginger, WD. Schuh, E. Höck, M. Reguzzoni, J.M. Brockmann, O. Abrikosov, et al. First goce gravity field models derived by three different approaches. *Journal of Geodesy, vOLUME 85, NUMBER 11, PAGES 819–843olume 85, number 11, pages 819–843*, 2011.

M.R. Pearlman, J.J. Degnan, and J.M. Bosworth. The international laser ranging service. In *Advances in Space Research*, volume 30, pages 135–143, July 2002.

C. Peat. *Heavens Above Envisat Orbit*. DLR, GSOC, 2016. URL `http://www.heavens-above.com/orbit.aspx?satid=27386&lat=0&lng=0&loc=Unspecified&alt=0&tz=UCT`. [online; visited on 26-04-2016].

S. Peters, R. Forstner, M. Weigel, and H. Fiedler. Reference scenario and target identification for autonomous active space debris removal methods. Technical report, Universitat de Bundeswehr Munchen, Deutsches Zentrum fur Luft-und Raumfahrt, 2013.

R.L. Ricklefs and C.J. Moore. *Consolidated Laser Ranging Data Format (CRD)*. The University of Texas at Austin(Center for Space Research) and the EOS Space Systems Pty. Ltd., 1.0.1 edition, 2009.

B.C. Root. Validating and improving the orbit determination of cryosat-2. Master's thesis, Delft University of Technology, 2012.

A. Rudolph, P. Bargellini, M. Garcia Matatoros, L. Ventimiglia, and D. Kuijper. Envisat orbit control, philosophy, experience and challenges. In *Proceedings of the 2004 Envisat & ERS Symposium (ESA SP-572). 6-10 September 2004, Salzburg, Austria. Edited by H. Lacoste and L. Ouwehand. Published on CD-Rom., nr63.1*, 2005a.

A Rudolph, P Bargellini, M Garcia Matatoros, L Ventimiglia, and D Kuijper. Envisat orbit control, philosophy, experience and challenges. In *Envisat & ERS Symposium, Volume 572*, 2005b.

T. Schildknecht, J.N. Pittet, J. Silha, M. Prohaska, and M. Ploner. Zimmerwald laser observations to determine attitude states of space debris. In *2015 ILRS Technical Workshop 26-30 October 2015 Matera Italy*, 2015.

E. Schrama, M. Naeije, Y. Yi, P. Visser, and C. Shum. Cryosat-2 precise orbit determination and indirect calibration of siral. In *End of Commissioning Phase Report, ESA contract report*, 2010.

L. Shakun, N. Koshkin, S. Korobeinikova, E.and Melikyants, S. Strakhova, and Terpan S. Monitoring of the inoperative envisat satellite's behaviour. In *Odessa Astronomical Publications, vol 26/2(2013)*, 2013.

J. Silha, Schildknecht T., J.P. Pittet, Bodenmann D., Karrang P. Kanzler, R., and H. Krag. Comparison of envisats attitude simulation and real optical and slr observations in order to refine the satellite attitude model. In *AMOS conference 2016*, 2016.

R. Storn and K. Price. Differential evolution a simple and efficient heuristic for global optimization over continuous spaces. *Journal ofJournal of Global Op, December 1997, Volume 11, issue 4, pp 341 359*, 1997.

E. Sutton. Comparison of atmospheric density models in the thermospheric region: Msis-86 and dtm-78. 2003.

B.D. Tapley, B.E. Schutz, and G. H. Born. Statistical orbit determination. Elsevier, 2004.

Z. Terze, A. Muller, and D. Zlatar. Singularity-free time integration of rotational quaternions using non-redundant ordinary differential equations. *Springer-Science+Business media dordrecht*, 2016.

A. Tewari. *Atmospheric and Space Flight Dynamics: ModModel and Simulation with MATLAB and Simulink*. Birkhauser, 2007.

K.F. Wakker. *Fundamentals of Astrodynamics*. Instituational Repository Library Delft University of Technology, 2015. ISBN 978-94-6186-419-2.

D.J. Wales. *Energy Landscapes*. University of Cambridge, 2003.

M. Weigel, G. Kirchner, and H. Fiedler. Slr tracking of envisat pasts its end of life. In *18th International Workshop on Laser Ranging, 13-Po40, November 2013*, 2013.

J. R. Wertz. *Spacecraft attitude determination and control.* Springer Science & Business Media, 2012.

J.R. Wertz. *Orbit & Constellation Design & Management.* Mircocosm Press and Springer, 2009.

B. Wie. *Space Vehicle Dynamics and Control.* American Institue of Aeronautics and Astronautics, Inc., 2008.

World Commission on Environment and Development (WCED). Our common future: Report of the world commission on environment and development. Oxford University Press Oxford, 1987.